Department of Precision and Microsystems Engineering

High-Resolution Multi-Material 3D Printing for Microfluidic Applications

D. Hopman

Report no : 2024.108
Coach : -
Professor : Dr. Paola Fanzio
Specialisation : High-Tech Engineering
Type of report : MSc Thesis
Date : 19-12-2024

TU Delft Delft University of Technology

Challenge the future

High-Resolution Multi-Material 3D Printing for Microfluidic Applications

by

D. Hopman

To obtain the degree of Master of Science
at the Delft University of Technology,
to be defended publicly on Thursday December 19th, 2024 at 13:00.

Student number:	4451740	
Project duration:	October 23, 2023 – December 19, 2024	
Thesis committee:	Dr. P. Fanzio,	TU Delft, supervisor
	Dr. ir. M. Tichem,	TU Delft
	Dr. C. Ayas,	TU Delft

An electronic version of this thesis is available at http://repository.tudelft.nl/.

TU Delft

Acknowledgements

At the moment of writing, I have been a student at the TU Delft for over 9 years. When I started this journey, I felt lost and overwhelmed by the magnitude and difficulty of the courses. Even though I have managed a lot of hardships since the start of this journey, I always refused to give up and that's what brought me here today. I would never have accomplished this milestone without several people, to whom I would like to express my deepest gratitude.

First of all I would like to thank my supervisor, Dr. P. Fanzio. At the beginning of this graduation year, I again felt lost (yes really... again after all those years). Your guidance, expertise and encouragement throughout this journey have been invaluable in shaping this research and my personal growth. I truly could not have asked for a better supervisor during the past year.

I would also like to thank Dr. ir. M. Tichem, who provided me with a lot of feedback after the literature review. And in advance, I would like to thank him again and Dr. C. Ayas for attending my graduation and being in the thesis committee.

I really appreciate all help from the TA's and other staff from the TU Delft who helped me out several times during this research.

And lastly, I would like to express my gratitude towards my parents who have always provided for me and stimulated me to do better. I am especially grateful for their unwavering belief in my potential, their patience during challenging times and their constant motivation.

D. Hopman
Delft, December 2024

Abstract

The primary objective of this research is to develop an efficient protocol which can be used to 3D print multi-material microfluidic devices with a high resolution. During this research, the fabrication of multi-material microfluidic valves is discussed as a showcase to verify the multi-material protocol, using a single affordable printer and multiple resin vats. In contrast to single material microfluidic fabrication methods, complex geometries can be created by the use of combinations of stiff and flexible materials in a single 3D print. This protocol aims to streamline the fabrication process while ensuring precise feature reproduction and robust mechanical properties in multi-material 3D printed microfluidic parts.

In this study, the effects of UV light exposure on feature accuracy and mechanical performance is systematically investigated. It is observed that for the rigid material, Anycubic High Clear, sample sizes increase and void features shrink when the exposure to UV light increases. For the soft material, Liqcreate Elastomer-X, shrinkage rates after swelling due to IPA absorption are compared under different conditions, revealing that shrinkage occurs more rapidly with a heat source than at ambient temperature.

Mechanical properties are further evaluated through tensile testing of four sets of printed dogbones, showing that extended UV exposure enhances mechanical properties such as the Young's modulus, ultimate tensile strength and strength at break. Elastomeric materials assessed in this study demonstrate an optimal measurement accuracy within a strain range of 10% to 50%. The influence of print orientation is assessed for the hard material. This experiment is executed for layer thicknesses from 10 µm to 200 µm across horizontal, vertical, and diagonal orientations, with vertically printed samples being closest to the intended dimensions.

A comprehensive multi-material 3D printing protocol based on the existing "print-pause-print" technique and utilizing the software UVTools is presented. Finally, a microfluidic Quake valve is designed and optimized for 3D printing, its performance is analyzed through finite element (FEM) simulation and analytical calculations.

The results of this study offer valuable insights into the optimization of multi-material 3D printing for microfluidic applications, highlighting several critical parameters that affect feature resolution and mechanical performance. The proposed protocol and findings serve as a foundation for future advancements in the fabrication of complex microfluidic devices.

Contents

Acronyms

AM Additive Manufacturing

MMAM Multi-Material Additive Manufacturing

STL Standard Triangle Language or Standard Tessellation Language

SAW Surface Acoustic Waves

IDT Interdigital Transducer

RF Radio Frequency

UV Ultraviolet

PDMS Polydimethylsiloxane

CAD Computer Aided Design

FDM Fused Deposition Modeling

PLA Polylactic acid

PETG Polyethylene Terephthalate Glycol

SLS Selective Laser Sintering

MJF Multi Jet Fusion

DLP Digital Light Processing

DMD Digital Mirror Device

LCD Liquid Crystal Display

CLIP Continuous Liquid Interface Production

MJP Multijet printing

2PP Two-Photon Polymerization

LFS Low Force Stereolithography

NIR Near-infrared

DLW Direct Laser Writing

MEHQ Methylethylhydro-quinone

UDMA Urethane dimethacrylate

PEGDA Poly(ethylene glycol) diacrylate

TEGDMA Triethylene glycol dimethacrylate

bis-EDA Bisphenol A ethoxylate diacrylate

EPOX 3,4 epoxycyclohexane)methyl 3,4 epoxycyclohexylcar- boxylate

DGEBA Bisphenol A diglycidyl ether

CDVE 1,4-cyclohexane dimethanol divinyl ether

DSO Disubstituted oxetane

AUD Aliphatic urethane diacrylate

TPO Thermoplastic olefin

BAEDA Bisphenol A glycerolate dimethacrylate

PEG Polyethylene glycol

VLM Viscous Lithography Manufacturing

FEM Finite Element Method

IPA Isopropyl Alcohol, Isopropanol, or 2-propanol

UTS Ultimate Tensile Strength

1 Introduction

Microfluidic valves play a central role in the dynamic world of microfluidics, a field dedicated to the manipulation and control of small volumes of liquids at the microscale. These miniature valves serve as essential components, allowing precise control and regulation of fluid flow within microfluidic devices. Microfluidic devices usually operate in the micrometer to millimeter range and can integrate various functions such as sample injection, mixing, and separation into compact and efficient systems. Its importance extends to applications such as medical diagnostics, chemical analysis, and environmental monitoring, where the ability to precisely manipulate small amounts of liquid is paramount. Traditionally manufacturing components such as microfluidic valves in microfluidics has required complex processes such as micromolding, microforming, embossing, and soft lithography [1]. However, these traditional microfluidic fabrication methods have common drawbacks. Multi-step processing is required and must often be performed in a cleanroom. Besides, alignment errors are prone to occur due to the multi-step fabrication process. These challenges hinder seamless assembly of high-resolution microfluidic components.

To overcome these challenges posed by traditional microfluidic manufacturing methods, 3D printing provides a streamlined solution that eliminates the aforementioned multi-step processes and alignment issues. Additive manufacturing allows for microfluidic devices to be manufactured directly from digital models, increasing design flexibility and accuracy. The rapid prototyping capabilities of 3D printing further accelerate the development of complex microfluidic devices.

3D printing, also known as additive manufacturing (AM), is a technology that allows objects to be created layer by layer from a digital design. The process starts with an STL (Stereolitography, also called Surface Tessellation Language or Standard Triangle Language) file containing geometric information about the object [2]. Slicer software is used to slice the 3D object to create 2D cross-sectional images (layers) which will be printed one by one. The variety of materials available offers great advantages in terms of design flexibility and functionality. 3D printing has already been used for microfluidic valve manufacturing, but its widespread adoption is hampered by several limitations, including: the trade-off between resolution and cost, and the challenge of achieving a balance between multi-material capabilities and resolution.

As mentioned, 3D printing is a promising fabrication method to create multi-material microfluidics. Preliminary studies have shown multifunctional integrated microfluidic systems and integrated electrodes [3], which remedies the need for complex multi-step processes and complicated alignment procedures. However, existing multi-material additive manufacturing (MMAM) has its limitations, because traditional methods often show a higher resolution microchannel. Besides, most 3D printing techniques are not suitable for MMAM and when they are, the material adhesion has to be optimized between the two materials. To overcome these problems, a printing technique must be chosen which can utilize multiple materials while maintaining a high resolution. One example of such a 3D printing technique is MultiJet Printing (MJP), which uses multiple nozzles and is therefore capable of MMAM. Other methods such as liquid crystal display (LCD), stereolitography (SLA) and digital light processing (DLP) 3D printing require modifications to both software and hardware to be capable of MMAM.

The aim of this study is to overcome the limitations associated with traditional manufacturing approaches in microfluidics by creation of a novel high-resolution multi-material 3D printing protocol. These efforts not only focus on achieving technological advances, but also emphasize the scalability and affordability of new manufacturing technologies. The importance of multi-material 3D printing in microfluidics is its ability to seamlessly integrate different materials in a single step manufacturing process, which is critical to create complex structures and functions, and it expands the potential applications of microfluidic devices. An application to demonstrate this novel manufacturing technique will be shown and evaluated on an MMAM microfluidic valve.

2

State of the art

2.1. Microfluidic Devices

Microfluidic devices are systems that can manipulate fluids at the microscale level with precise control. These small amounts of fluid can be manipulated by using small channels or valves, often utilizing channel sizes ranging from 1 µm to 500 µm [4]. Besides precise control, the downscaling of traditional biomechanical protocols offers benefits in efficiency and cost-reduction [5]. Gharib, Bütün, Muganlı, *et al.* [5] distinguishes passive and active microfluidics. As the name suggests, active microfluidic devices require external energy to disturb these particles or fluids inside the device. This distinction is also applicable for microfluidic valves, active microfluidic valves require an energy consuming actuation mechanism. Various actuation methods for microfluidic valves will be discussed in the next subsection.

2.1.1. Microfluidic valves

Microfluidic valves can be used to manipulate fluid samples in channels with tens to hundreds microns in size [6], which makes microfluidic valves important components in microfluidic systems. As stated in Section 2.1, a clear distinction can be made between passive and active microvalves. Passive microvalves are driven by the back pressure, whereas active microvalves need a driving device. Microvalves can be driven by several different actuation mechanisms, some examples of which are electricity, magnetism, gas, and Surface Acoustic Waves (SAW). Qian, Hou, Li, *et al.* [6] describes these actuation mechanisms, which will be further elaborated in this section.

Electricity can be used to drive piezoelectric actuators. Microvalves using piezoelectric actuation can create large bending forces with resulting small displacements, making them particularly suitable for high pressures and precise control.

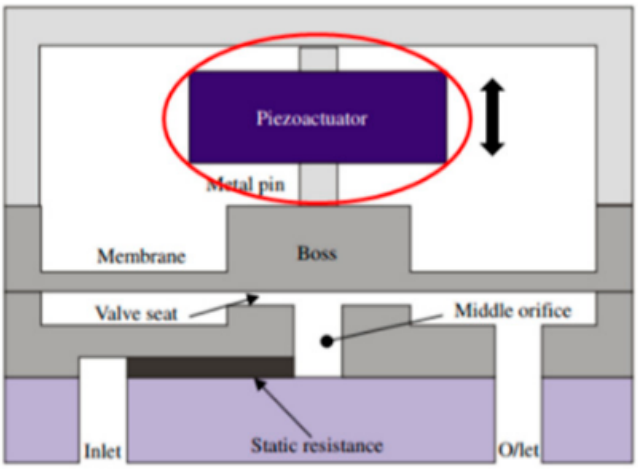

Figure 2.1: An example of a high pressure piezoelectric actuated microfluidic valve, picture adapted from [7].

Electricity can also be used to induce magnetism, magnetic actuation is characterized by a low energy consumption and easy scalability of the structure [6]. Electromagnetic actuation can in some cases be a requirement for pneumatic pressure control for the lab-on-a-chip [8]. Some advantages of electromagnetic actuation

are the reversibility of flow, a fast response and precise control [6]. For more simplistic applications, permanent magnets can be used to actuate the microvalve.

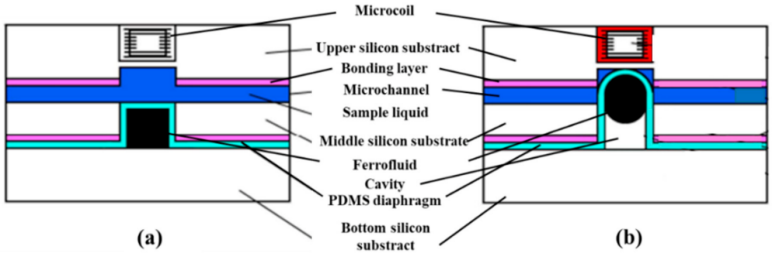

Figure 2.2: An example of an electromagnetic actuated microfluidic valve in which **(a)** is the open state and **(b)** is the closed state, picture adapted from [9].

Besides piezoelectric and magnetic actuation, photoresponsive actuation is possible using a light source, photoresponsive microvalves are based on light (photon) actuation [10]. Unlike other types of microvalves, photoresponsive microvalves are actuated externally, therefore the need for physical contact between the actuator and valve is eliminated, this reduces the complexity of the microfluidic device. The main disadvantage of photoresponsive actuation is its slow response time of over 1 second.

Gas actuated microfluidics in the form of pneumatic systems can be easily actuated using a compressor or another pressure source, the response time is fast and pneumatics have been used extensively in microvalves, micropumps, microsensors, microchannels, micromixers and other control systems [6] [11]. An example of gas actuated microfluidic valves is the Quake valve [12]. Pneumatic systems can be combined with thermal functions to obtain thermopneumatic systems, thermopneumatic systems utilize a microheater (thermoelectrically driven) to thermally expand minute volumes of air [6]. These valves are examples of bistable microvalves, bistable microvalves are valves which are either open or closed. The main drawback of bistable microvalves is the continuous addition of energy in the form of heat to keep the valve closed. The energy consumption of bistable microfluidic valves can be lowered by using thermal buckling of the membrane [6]. Pneumatic actuation requires a rounded microfluidic channel due to the pressure distribution on the membrane. This requirement is a drawback of gas actuated microvalves, since rounded microfluidic channels are a challenge to realise in current microproduction technology, to overcome this challenge, the design needs alteration or the fabrication method needs to be revisioned.

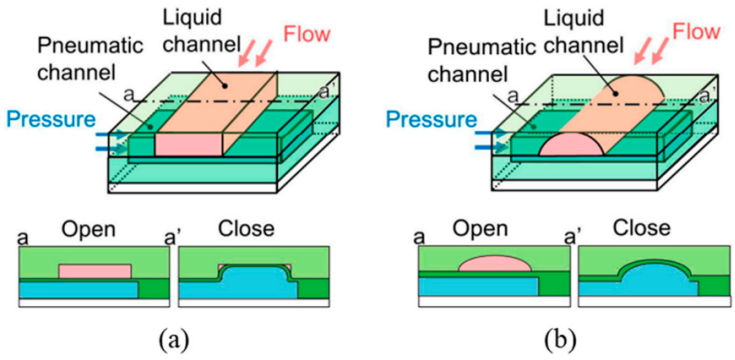

Figure 2.3: An example of a gas (pneumatic) actuated microfluidic valve in which **(a)** has a rectangular cross section and **(b)** has a semicircular cross section, picture adapted from [13].

Surface acoustic waves (SAW) are elastic waves that propagate along the surface of an object [6]. This technique relies on the generation and manipulation of sound waves to achieve fluid control. When interrogated by the corresponding signal, the double membrane expands due to electrostatic drive and sucks liquid into the chamber [14]. The coded interdigital transducer (IDT), which can be seen in figure 2.4, only responds to a coded signal. Transducers are devices which can convert energy from one form to another, an example of a transducer is a loudspeaker which converts electrical energy to acoustic waves. As can be seen, both input IDTs and output IDTs are used in this example of a SAW device. The IDTs are deposited on a piezoelectric substrate. The difference with the previously described piezoelectric actuation is the fact that this technology uses wireless actuation. The working principle is as follows, the input IDT transduces the coded input radiofrequency (RF) signal into an acoustic wave. These surface acoustic waves interact with liquids or gases within microchannels. This interaction can lead to the formation of pressure nodes and antinodes along the channel.

This type of actuation allows microvalves to open and close, regulating the flow of liquid by precisely controlling the frequency and amplitude of the surface acoustic waves.

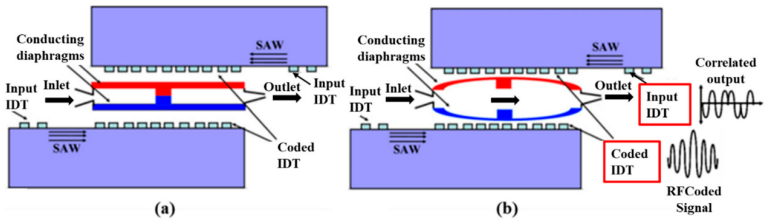

Figure 2.4: An example of a SAW actuated microfluidic valve in which **(a)** is the normally closed state and **(b)** is the open state, picture adapted from [14].

Qian, Hou, Li, *et al.* [6] describes current microfluidic valves as an imperfect technology and describes several problems with existing microfluidic valves. Some of these problems are a high leakage rate, low precision, poor reliability, high energy consumption and a high cost of manufacturing. These problems lead to some requirements for microfluidic valves, it is described that microvalves must have a low leakage rate, small dead volume, low power consumption, insensitivity to contamination, fast response and linear operation. The dead volume of a microvalve refers to the volume of liquid that remains trapped within the valve, or is not flushed out, when the valve is in the closed position. This is the part inside the valve that does not participate in fluid flow through the system. Dead volume can impact accuracy and precision, especially in microfluidic applications that manipulate extremely small volumes. Current microvalves often meet only one requirement instead of all requirements. To overcome some of the above mentioned disadvantages of current microfluidic valves, an appropriate and versatile fabrication method must be chosen. A list of recommendations to improve microfluidic valves is given by Qian, Hou, Li, *et al.* [6], some key points are the use of less components to reduce complexity and reduce the leakage rate. Besides, to control the fluid flow more precise, optimization of the actuation mechanism itself is advised. Lastly, the biocompatibility of certain materials needs to be evaluated before application in the human body. However, biocompatibility is out of scope for this literature review. In the next section, several traditional microfluidic fabrication methods will be described.

2.2. Traditional Microfluidic Fabrication Methods

2.2.1. Replica Molding

Replica molding (often called soft litography) is a commonly used fabrication method for biomedical microfluidic devices [3], [15], [16]. The fabrication method consists of the following steps: coating a photoresist on a silicon substrate, exposing the wafer to UV light, etching the photoresist, pouring polydimethylsiloxane (PDMS), and curing the PDMS in an oven [5], [17]. After curing, the PDMS can be separated from the mold and bonded (plasma bonding or PDMS) to a piece of microscope glass, this forms the microchannel(s) [5].

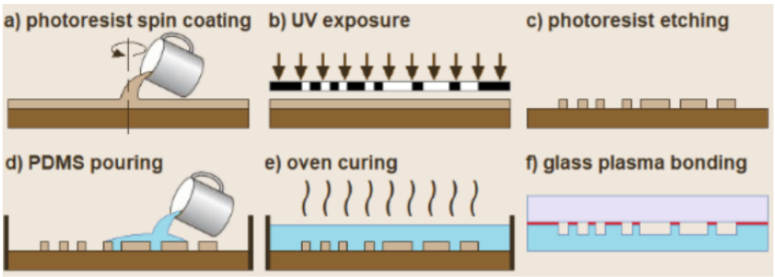

Figure 2.5: An example of replica molding using PDMS, picture adapted from [17].

Techniques such as replica molding are challenging due to the multi-step process. PDMS microfluidic devices are created out of 2D planes making up a 3D structure, the alignment of these planes is a known difficulty [4], [18]. For example, devices with an inflatable structure are hard to fabricate using this technique [11]. Besides alignment errors, replica molding is time consuming and the design complexity is limited. Also, the need for a cleanroom makes this method costly [5].

2.2.2. Injection Molding

Injection molding is a fabrication method which produces parts by injection of molten material (thermoplastics) into a mold. This fabrication method is characterized by a high throughput and high accuracy while being cost efficient [19]. The fabrication method consists of the following steps: a thermoplastic is melted in a compressible

chamber, both sides of the mold are compressed to form the inside of the mold, the cast object can be removed from the mold after cooling down [5]. Some drawbacks of this fabrication method are the restriction to use thermoplastics and the molds can be expensive to fabricate [15], [19]. Besides, the process requires multiple fabrication steps and is only able to create 2D single material structures.

2.2.3. Hot Embossing

Hot embossing is a fabrication method which uses heat and pressure to transfer a mold pattern onto a thermoplastic substrate. The thermoplastic substrate is often a thin film, after heating this thin film between the molds in a vacuum chamber, pressure can be applied to transfer the mold shape onto the substrate. After cooling down, the processed polymer can be removed [3]. Hot embossing creates less stress on the substrate in contrast to injection molding, this is due to a smaller distance traveled by the thermoplastic [5]. However, both fabrication methods are restricted to the use of thermoplastics. Also, hot embossing is not suitable for the fabrication of complex devices [19].

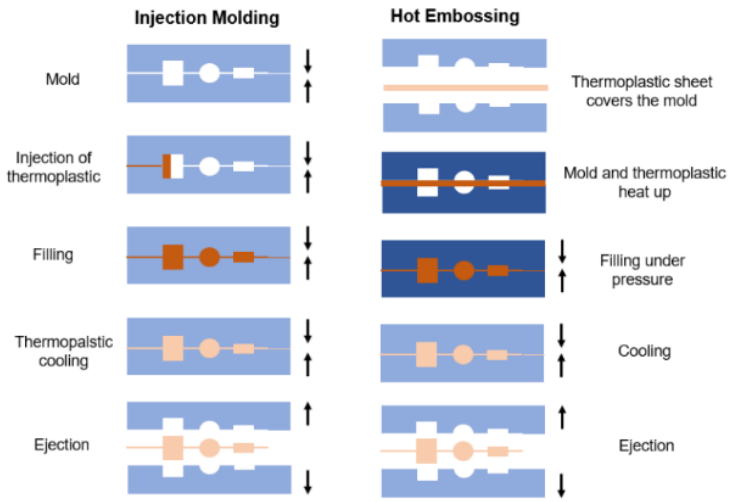

Figure 2.6: The difference between injection molding and hot embossing, picture adapted from [20].

2.2.4. 3D Printing for microfluidics

3D printing is a fabrication method which successively fuses or bonds layers of materials to create a 3D object. Microfluidic devices can be fabricated through direct or indirect 3D printing. Direct 3D printing encloses the microchannels during fabrication, whereas indirect 3D printing creates the microchannels using the 3D printed mold to cast PDMS or another material [21]. The difficulty of fabricating microfluidic devices lies in special requirements, both high resolution and correct handling of small sized structures are required. 3D printing is a promising method to fabricate microfluidics, however some challenges do exist. The Z-resolution can be a drawback depending on application, the surface finish is not smooth due to layering, there are not many transparent materials to choose from, and the precision of fabricated hollow and void sections is low [22]. Despite these disadvantages, 3D printing is very promising for the fabrication of microfluidic devices, it offers the ability to create microfluidic devices with fine features at a low cost in contrast to processes which are traditionally executed in a cleanroom [3]. Although the resolution is still limited, 3D printing enables for the design and construction of complex shapes through one-step manufacturing [23]. Besides, manufacturing digitally designed parts can be completed in hours, compared to days for soft lithography [18]. This makes 3D printing a very promising fabrication method to overcome the limitations from traditional microfluidic manufacturing methods. Additionally, the design freedom to create complex devices increases, whereas the cost to produce the microfluidic device decreases when using 3D printing [24]. This extended design freedom results in the development of complex designs such as three-dimensional microfluidic designs and modular microfluidic devices [25], modular microfluidic devices allow for quick changes to a device without refabricating the entire device [4]. A successful implementation of modularity in microfluidics has been proposed by Bhargava, Thompson, and Malmstadt [26].

It has been shown that additive manufacturing, also known as 3D printing or layered manufacturing is a great tool to improve or replace the above mentioned traditional microfluidic fabrication methods. Eliminating the need for replica molding (formative manufacturing) or machining (subtractive manufacturing), additive manufacturing serves as a great tool to produce custom parts from a broad range of materials. With 3D printers becoming more and more consumer available, a large variety of available materials, a high design flexibility, and decreasing

prices, 3D printing becomes an attractive microfluidic fabrication method. Moreover, the broad range of 3D printing techniques, of which various techniques will be described in the next section, further enhances its appeal as a versatile microfluidic fabrication method.

2.3. Additive Manufacturing Techniques

The procedure to 3D print objects, starts with the creation of a digital model (CAD design), after creation of this model it will be exported as a STL file. This STL file is then opened and sliced using slicer software (such as CURA or PrusaSlicer), which creates numerous 2D layers that represent a cross section of the object. After configuring the printer settings and the slicer settings, the 3D printer will start building the designed object layer by layer. Depending on the material and support generated by the slicer, post-processing may be necessary, for example: removing the support material, sanding the object, polishing the object or applying paint. Nowadays print-in-place is becoming more popular, which creates movable mechanisms from a single print sequence, eliminating the need for assembly.

Several 3D printing techniques exist nowadays, from the extremely popular Fused Deposition Modeling (FDM) to the more expensive 2-Photon-Polymerization (2PP). Some of the currently existing 3D printing techniques are suitable for the manufacturing of micro- and nanostructures. 3D printing techniques can offer several advantages such as the elimination of multi-step fabrication, and a reduction of the likelihood that manufacturing constraints complicate the fabrication. Each 3D printing method has its pros and cons that will be discussed in this chapter.

An assessment of resolution and multi-material capabilities in 3D printing will be made in the next section. Two types of resolution will be distinguished in this literature review; the Z-Resolution (i.e. the minimal thickness or vertical layer height) and the horizontal XY-resolution, also called spatial resolution. The multi-material additive manufacturing capabilities will be assessed using information from the available literature.

2.3.1. Fused Deposition Modelling (FDM)

FDM is a 3D printing technique which uses material properties of thermoplastics for the benefit of 3D printing, by melting and extruding the thermoplastic filament an object can be created layer by layer. FDM is very popular due to its affordability and wide range of applications.

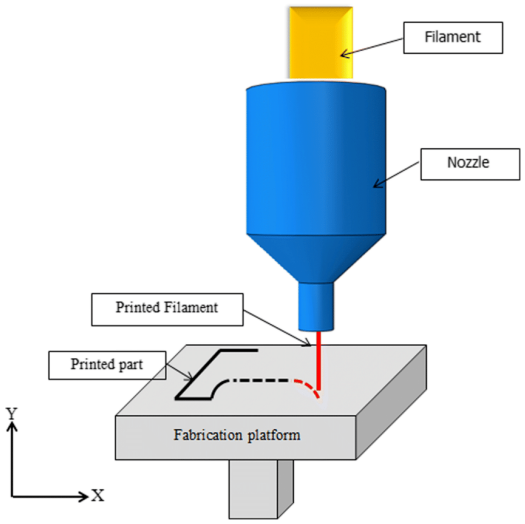

Figure 2.7: A schematic overview of FDM 3D Printing, picture adapted from [27]

The resolution of FDM printing is dependent on the nozzle diameter. The diameter of the extruded filament results in a minimum feature size. For most commercial printers the minimum nozzle size is 0.1 mm, therefore the theoretical XY-resolution is at best 0.1 mm with a vertical resolution of 0.05 mm [28]. The difference between the minimum feature size and resolution is described as follows: the minimum feature size focuses on the smallest details, while maximum resolution is a comprehensive measure of the level of detail. When printing holes (for example for microfluidic devices), the mean measured diameter error is mostly affected by the nominal diameter of the hole itself according to Alexopoulou, Christodoulou, and Markopoulos [29]. According to this research, the printing speed and layer thickness do not appear to affect the mean measured diameter error.

This technique allows for multi-material additive manufacturing within a single print, since the printer can be (manually or automatically) paused and the material can be swapped. Multi-material FDM 3D printing has been conducted for sensors in soft pneumatic actuators in previous work by Dezaki, Sales, Zolfagharian, *et al.* [30].

Besides the ability to create multi material 3D printed objects, Damanpack, Sousa, and Bodaghi [31] states that the density can be adjusted by altering the nozzle temperature and flow rate. This density was altered by creating bubbles during fabrication, essentially creating a lightweight PLA foam.

However, FDM 3D printing does not have a sufficiently high resolution, speed and/or material strength for certain applications [32]. In applications where functional parts with specific mechanical properties are essential, such as in the aerospace or automotive industry, metal 3D printing technologies like Selective Laser Sintering (SLS) or Multi Jet Fusion (MJF) may offer superior material strength and performance. The strength is based on fusion or bonding between layers, in FDM 3D printing this fusion is not sufficient and will often lead to stress fractures [15]. The accuracy of FDM 3D printing is low in contrast to other techniques. This is mostly due to shrinkage, with additional factors such as the motion system, the viscosity of the thermoplastic filament, and the nozzle size. Shrinkage makes it difficult to create geometric accurate results and is hard to compensate for, adjusting parameters such as the top/base layer thickness or infill density will lead to shrinkage in different directions (anisotropic) [33]. To fabricate microfluidic devices using FDM 3D printing, obtaining sufficiently transparent microchannels can be challenging [34] [35] [36].

Macdonald, Cabot, Smejkal, *et al.* [37] states that FDM printed samples have channels with high deformation in areas in which the channel direction changes. According to Collingwood, Silva, and Arif [4] it might be beneficial to bond the microfluidic device to glass on one side, with an FDM 3D printed object this is difficult due to leakage, a resin-based 3D printed object is easier to attach to glass using resin as glue and curing it afterwards. As stated, FDM has a high surface roughness, which is undesirable for most microfluidic devices, except for the fabrication of micromixers where turbulent flow is beneficial [4].

2.3.2. An introduction to 3D Photopolymerization

Photopolymerization is a process in which a liquid resin, usually containing a polymer and a photoinitiator, undergoes a chemical reaction when exposed to ultraviolet (UV) light. The UV light triggers a polymerization reaction that solidifies the liquid resin. This technique is commonly used in 3D printing techniques such as stereolithography (SLA) and digital light processing (DLP), which enable precise layer-by-layer construction of objects by controlling the exposure to UV light. 3D printers using vat polymerization techniques (3D photopolymerization), work by using a vat filled with liquid pohotopolymer resin to create objects layer by layer. Polymers consist of a repeating framework of monomers which are created by polyaddition (conservation of substance) or polycondensation (loss of substance, e.g. water or alcohol) reactions of the monomer units [38]. Similar to the approach discussed in section 2.1.1, a digital model is sliced into cross sections, these layers are illuminated by a photon source and subconsequently the build platform is incrementally lifted or lowered (depending on the design of the 3D printer), these steps are repeated until a full representation of the 3D model is completed. Afterwards, the object should be rinsed with isopropyl alcohol to remove uncured resin.

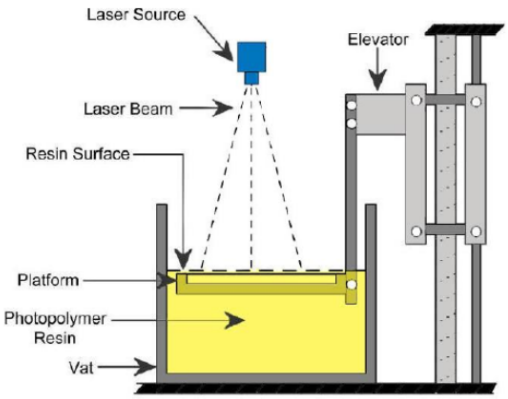

Figure 2.8: A schematic overview of stereolitography using a laser as photon source, picture adapted from [39].

The high resolution which can be achieved by 3D photopolymerization, aided by the use of materials with certain properties (such as shore hardness, transparency, opacity etc.) has resulted in a rapid rise of application in microfluidics, biomedical devices and soft robotics [40]. A thorough description of the viscous properties of the resin is important for the required resolution in the z-direction. The recoating process is dependent on both the viscosity of the resin and the accuracy of the stepper motor operating the build platform [41], it involves spreading a thin layer of liquid photopolymer resin evenly across the build platform after the previous layer is solidified with UV light. The viscosity of the resin affects how evenly the resin spreads across the platform, while the precision of the motion system that controls the movement of the platform determines the accuracy of the placement of each layer and ultimately the overall quality of the printed object.

2.3.3. Stereolitography (SLA)

SLA 3D printing is a method introduced and patented by Chuck Hull in 1986, it is a method that uses a movable photon source (a LED or a laser) to activate the photopolymerization process in a VAT of photocurable resin to successively print solid layers on top of the previous layer [42]. SLA is part of the vat (3D) polymerization techniques, in which a resin tank is filled with liquid polymer. An UV laser with a specific wavelength (usually in the UV-range) solidifies the liquid resin by means of polymerization and cross-linking, corresponding to the 2D sliced image from the CAD model. Since the resolution of FDM 3D printing is relatively low, stereolitography using photopolymerization is a better option for the fabrication of microfluidic devices, stereolitography has a resolution in the micron scale [43]. Therefore, in contrast to FDM printing, the surface finish is smooth. Like FDM, SLA is an affordable and therefore consumer friendly 3D printing technique. Due to the point by point exposure, printing speeds are relatively slow. In SLA 3D printing, the layer of resin which is polymerized is in direct contact with the air. During this polymerization, oxygen may inhibit the polymerization reaction by absorbing UV light and interfering with the free radical reaction which initiate the polymerization. As a result, the resin may fail to cure or cure completely in the presence of oxygen, resulting in failed layers or partially cured layers of the printed object.

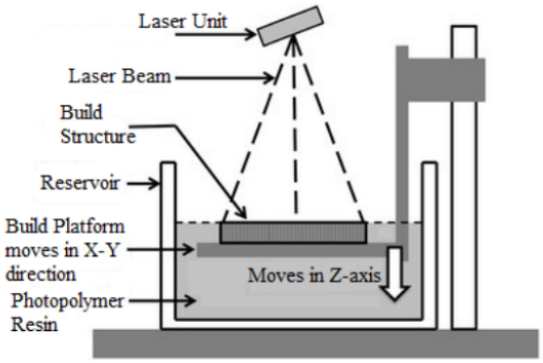

Figure 2.9: a schematic overview of SLA 3D printing using a laser as photon source, picture adapted from [44].

SLA printed parts need to be rinsed in IPA (isopropyl alcohol) before final curing with an UV lightsource. Another disadvantage of SLA 3D printing is the slow printing rate, it can only print at speeds which are supported by the movement of the laser beam [45].

The vertical (Z-axis) resolution is described by the minimum distance the stepper motor can generate, which is approximately 25 µm for consumer level printers. However, with a more expensive SLA 3D printer (dwslab xfab), minimum layer heights of 10 µm have been described by [46]. The high spatial resolution or the XY-resolution is one of the main advantages of SLA 3D printing [41]. The spatial resolution is dependent on the minimum laser spot size, the highest spatial resolution is around 25 µm with a Formlabs Form 3+ printer [47]. SLA 3D printing exposes every pixel to UV light sequentially, meaning that in theory the irradiation could be adjusted per pixel, allowing the printer to print grayscale patterns. The vertical resolution (z-direction) is dependent on the depth of penetration from the photon source and can be controlled using suitable absorbers. However, the curing depth is also dependent on the intensity and exposure time of the photon source [41]. Another technique which is similar to SLA is Low Force Stereolitography (LFS). LFS can be seen as the successor of SLA, it utilizes a special Light Processing Unit (LPU) [48] which eliminates stray light by using a spatial filter to eliminate stray light from entering the resin tank, and a series of mirrors to ensure that this filtered light beam is always perpendicular to the print plane.

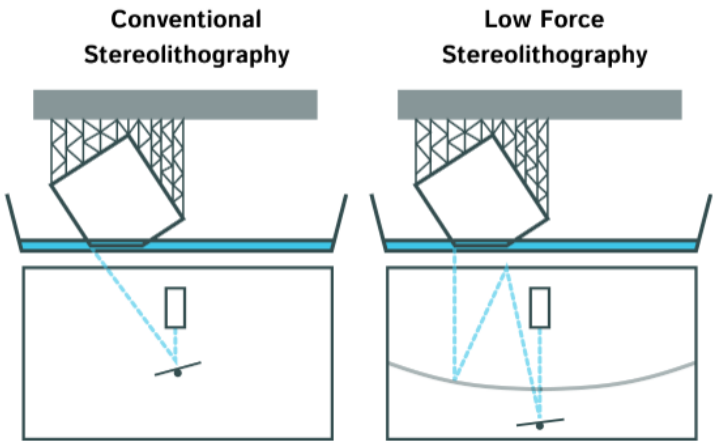

Figure 2.10: Conventional stereolitography vs LFS. LFS 3D printing uses the same principle as SLA, but uses filters and mirrors to eliminate stray light, picture adapted from [49].

Besides a more consistent layer spot, LFS utilizes a flexible film on the bottom of the vat, which reduces stress on the partially cured resin. Due to these improvements, the surface finish is smoother and there is less need for support material, which is claimed to be around 4 times less. SLA 3D printing can be used for MMAM, however to enable the 3D printer to do so, adaptation to both software and hardware is needed. For example, a multi-layered polypill containing six drugs has been reviewed by Robles-Martinez, Xu, Trenfield, *et al.* [50], using SLA 3D printing as the fabrication method. This study shows that after modifications, SLA is suitable for multi-material additive manufacturing, the main adaptation is a vat change or change of resin during printing [51]. Therefore, out of the box, SLA 3D printers are not suitable for MMAM.

2.3.4. Digital Light Processing (DLP)

In DLP, a projector is used to project an image of a complete cross section of a CAD model (the model is sliced into 2D layers) [45]. The generated layers consist of voxels, which essentially is a 3D pixel [52].

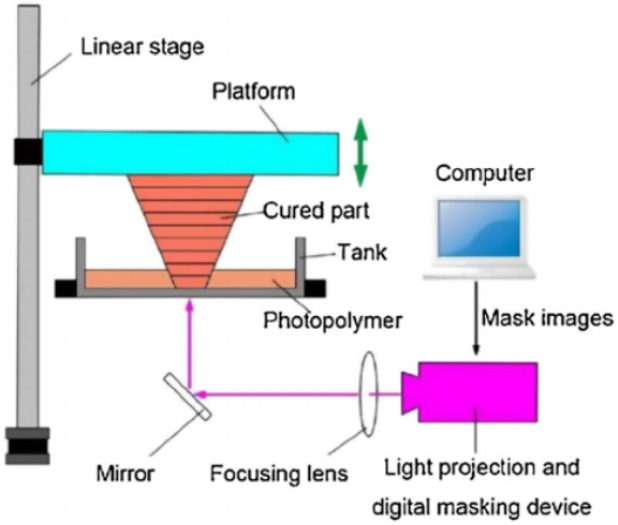

Figure 2.11: A schematic overview of DLP 3D printing, picture adapted from [53].

This technique is relatively fast, because of plane exposure (illumination of a complete layer). The amount of pixels on the imaging chip (DMD, Digital Mirror Device) is fixed, therefore the resolution is dependent on the optics. Imaging lenses of different magnification can be used. When a higher resolution is required, the print size will shrink, 0.6 µm to several 100 µm is possible using the DLP technique [54], whereas [45] gives the minimum print size (of an object) to be 50 µm and [41] states the spatial resolution to be 10-50 µm and the resolution in vertical (z-direction) to be dependent on the penetration depth of the photon source and the resulting curing depth, this vertical resolution can be altered using light absorbing additives which help to reduce

undesirable events such as light scattering. Since altering of the optics is out of scope for this research, known parameters from the ”B9Creations Core 5 Ascent XL” will be taken, which has a spatial resolution of 25 µm and a vertical resolution of 10 µm.

A great advantage of DLP 3D printing is that the layer of resin being illuminated and polymerized by the photon source is often on the bottom of the vat (bottom-up configuration), making DLP less susceptible to oxygen inhibition as compared to SLA 3D printing (top-down configuration) [41]. Another advantage of DLP 3D printing is that it can print very high resolution objects with a small size [55]. Besides, DLP 3D printing has the ability to process both regular nonfilled photopolymers and slurries containing ceramic or metal particles [56]. DLP, like SLA 3D printing, can also be used to print objects with multiple materials when both printer and software are modified. One example of MMAM enabled DLP 3D printing is a study by Kang, Chang, Costa, *et al.* [57], which shows a heterogeneous structure made out of two materials using a custom built DLP 3D printer. Therefore, out of the box, DLP is not suitable for MMAM.

2.3.5. Liquid Crystal Display (LCD)

LCD 3D printing utilizes a liquid crystal display as an imaging system, an electric field is applied to the liquid crystal in order to change its molecular arrangement, which prevents light from passing through. The working principle is almost the same as DLP 3D printing, both techniques use UV light to illuminate a complete layer. However, DLP 3D printing uses a projector, whereas LCD 3D printing uses the LCD screen as a mask with UV lights underneath. This technique is often labeled as Masked SLA or MSLA [52]. The resolution of this technique is high, however fully dependent on the pixel density of the LCD screen used, for example 4K, 6K, 8K and 12K screens are currently available. The highest spatial (XY) resolution of LCD 3D printing is described to be 22 µm with a vertical resolution of 10 µm [47]. However, when this technology improves, an even higher pixel density (and thus resolution) is possible.

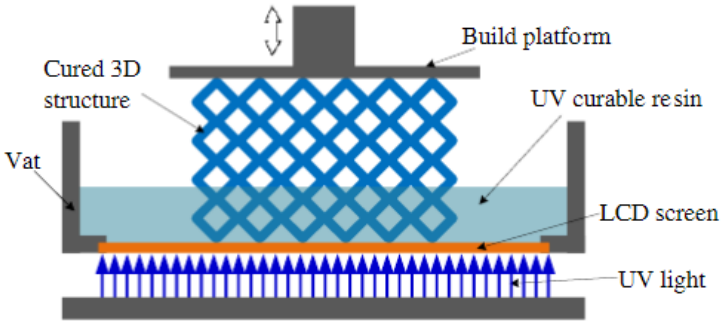

Figure 2.12: A schematic overview of LCD 3D printing, picture adapted from [58].

According to [59] the LCD panel has a certain lifetime, which means its performance decreases over time. The main disadvantage of LCD panels is the occurence of light leakage when such a screen degrades. Which in turn decreases the quality of the printed objects or even the quality of the resin. This phenomenon has also been described by [45], in which it is added that a small number of faulty rearranged liquid crystal molecular results in weak light leakage. Since the whole screen is illuminated at once, this light leakage can be described to be uniform, and thus can be accounted for in the slicer settings [52].

The difference between LCD 3D printing and other photopolymerization additive manufacturing methods is the lower light intensity. A lower light intensity makes it harder to initiate photopolymerization, which is induced by photolysis of the cationic photoinitiatiors. It can however print objects utilizing the same resins as the DLP 3D printing technique by varying the amount of initiator or an extended exposure time. LCD 3D printing, like SLA and DLP 3D printing, requires post processing in the form of rinsing and post curing [52].

2.3.6. Continuous Liquid Interface Production (CLIP)

CLIP is a more advanced version of DLP 3D printing, utilizing a permeable membrane to permeate oxygen, which inhibits the radical polymerization by (i) quenching of the excited state photoinitiator or (ii) forming a peroxide when interaction with a free radical of a propagating chain occurs [60].

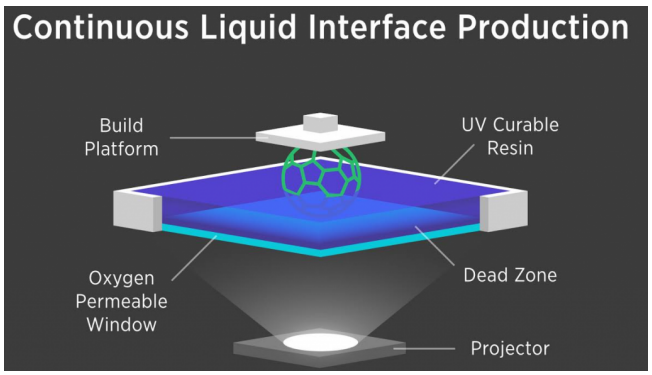

Figure 2.13: A schematic overview of CLIP 3D printing, picture adapted from [61].

The permeated oxygen creates a dead zone at the bottom of the vat, the thickness of the dead zone is given by formula 2.1, in which ϕ_0 is the photon flux, α_{PI} is the coefficient of absorption and D_{c0} is the curing dosage of the resin.

$$\text{dead zone thickness} = C\left(\frac{\phi_0 \alpha_{PI}}{D_{c0}}\right)^{-0.5} \tag{2.1}$$

A widely used example of such a permeable membrane is the amorphous fluorpolymer window, Teflon AF 2400, which shows a very high oxygen permeability [62].

The printing speed for CLIP is limited by the resin cure rates and resin viscosity instead of stepwise layer formation. However, CLIP is a continuous process and the refresh rate of the projected images can be increased without changing the print speed itself [63], therefore CLIP enables printing speeds 25 to 100 times faster than DLP.

The light source and imaging system (projector + lenses) are exactly the same for DLP and CLIP. However, due to the high speed, adhesion problems may arise which can be eliminated by using a lower viscosity resin. The same resin as used with DLP 3D printing can be used if the speeds are set lower [45]. The resolution is similar to the resolution of DLP 3D printing, which is 10 µm in Z-direction for DLP, however CLIP creates smooth layers and eliminates the voxelated effect that is typically seen in DLP prints [47], [64]. Lee, Hsiao, Lipkowitz, *et al.* [65] enhanced this technology, obtaining a spatial (XY) resolution of 30 µm, which is defined as the smallest feature size (1 pixel) in his work.

2.3.7. MultiJet Printing (MJP)

MJP uses arrays of piezo activated nozzles (printhead) to deposit photosensitive resin. This resin is cured by an UV lamp and after curing of the first layer, it is ready to deposit the next layer and repeat the process. This process is repeated until the object is finalized.

The main difference between MJP and techniques such as SLA, LCD, DLP and CLIP is that MJP is extrusion based. Besides, the imaging control and curing light source are independent, the image is created by the printhead instead of a UV laser or UV lights. Due to the extrusion based nature of MJP 3D printing, no masking is required. After extrusion, the entire 2D plane can be illuminated with UV light. As described in the section for LCD, resin exposed to a small amount of UV light can degrade, a phenomenon which does not occur in MJP. Therefore every wavelength can be used and a larger variety of resins can be implemented. Resins inhibiting radical, cationic and hybrid photopolymerization can be chosen for this technique, the working principle of these photopolymerization systems will be explained in section 2.4.

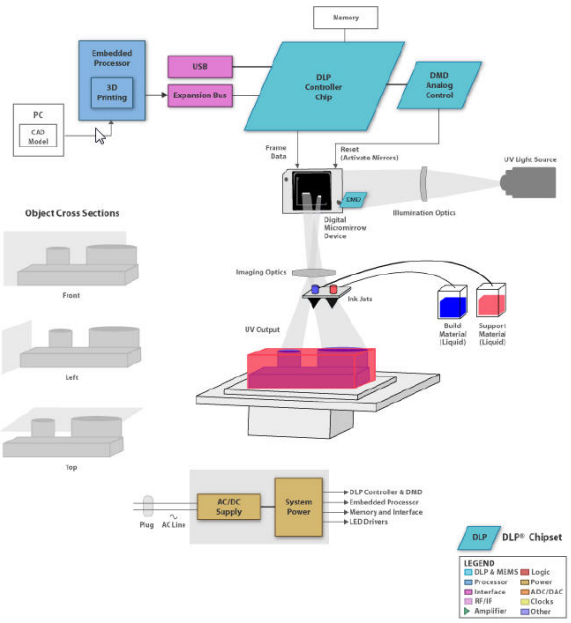

Figure 2.14: A schematic overview of MJP 3D printing, picture adapted from [66].

The main advantage of MJP is the ability to spray multiple materials and colors through various nozzles. The resolution in Z-direction is very high and can be as low as 16 µm [67]. This number is supported by manufacturers (proto3000), which states that MJP 3D printing can achieve a spatial resolution of 0.0017 mm, which equals 1.7 µm [68]. Besides, support material can be easily removed and eliminates the need for post processing. Keating, Gariboldi, Patrick, *et al.* [69] have used MJP 3D printing to fabricate a microfluidic valve using multiple materials. However, a low viscosity is advised to keep the resin printable through the nozzles. Another disadvantage is that both the machine and the low viscosity resins are expensive.

2.3.8. Two Photon Polymerization (2PP)

2PP is a technique commonly used in micro- and nanofabrication, just like SLA and LFS a laser is directed into a photosensitive resin, the resin cures (polymerizes) at the point where the 2-photon absorption occurs. The photosensitive resin used in 2PP is designed to polymerize when it simultaneously absorbs two photons of that particular wavelength. However, unlike stereolithography, 2PP does not cure the resin with UV light, but with femtosecond laser pulses in the visible to near-infrared spectrum [70].

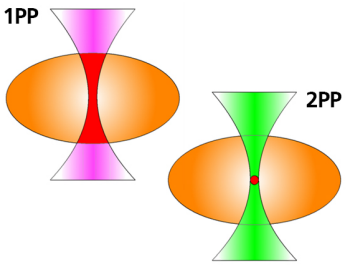

Figure 2.15: the difference between 1PP and 2PP, 1PP cures the entire path of illumination, whereas 2PP only cures a small focal volume [70].

2PP uses a resin which is transparent to NIR (near infrared light), to make sure cross-linking will only occur within the vocal volume of the laser [71]. Normally, these wavelengths are not absorbed by transparent resins. However, due to the narrow focus and the pulsed nature of the irradiation (energy released over a few hundred femtoseconds), two-photon absorption occurs within the focal volume, triggering the same chemical reaction as UV-light irradiation. Therefore, the polymerization is strongly restricted to a small focal volume. 2PP is often referred to as Direct Laser Writing (DLW), because the focal point of the laser can be positioned anywhere within the resin (3D) [72]. This technique allows for high resolution and intricate structures due to its self supporting nature, hence no supports are needed.

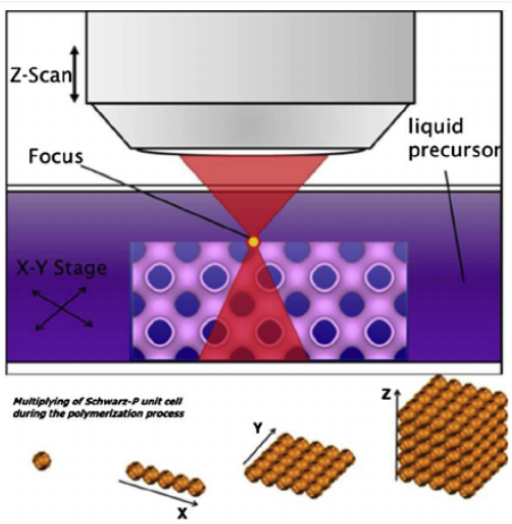

Figure 2.16: A schematic overview of a 2PP process, picture adapted from [73].

Rad, Prewett, and Davies [74] describes 2PP as the leading technology in ultra precision, 2PP has several advantages over SLA 3D printing, some of which are: a nonlinear response of the photoresists which creates superior resolution and the ability to create a high ratio between length and width. The XY-resolution of 2PP printing is described to be around 100 nm, whereas the best attainable resolution for μSLA printing is 0.5 μm [75]. For example, the Z-resolution for the commercially available ”Nanoscribe Professional GT2” 2PP 3D printer is 160 nm [76]. However, it is noteworthy that the resolution of 2PP 3D printing is adjustable, both the voxel dimensions and the objective lens can be changed [74].

2PP 3D printing can be further enhanced by adding a cross-linker to the used material, therefore generating more support and resistance to stresses during the building phase. By using this method, Emons, Obata, Binhammer, *et al.* [77] achieved a spatial resolution of 45 nm, which is a factor 10 better than even micro SLA. Out of the box, 2PP is not suitable for MMAM, however an example of multi-material objects is provided by Hu, Rance, Trindade, *et al.* [78], in which a multi-material basket is presented.

2.3.9. Comparison of 3D Printing Techniques

Table 2.1: A comparison of techniques

Categorized techniques	XY-Resolution	Z-Resolution	Materials	Multi-material
FDM	100 μm [28]	20 μm [47]	Thermoplastic filaments	Yes [30]
SLA	25 μm [47]	10 μm [46]	Liquid photopolymer resins	No
DLP	25 μm [47]	10 μm [47]	Liquid photopolymer resins	No
LCD	22 μm [47]	10 μm [47]	Liquid photopolymer resins	No
CLIP	30 μm [65]	10 μm [64] [47]	Liquid photopolymer resins	No
MJP	1.7 μm [68]	16 μm [67]	Liquid photopolymer resins	Yes [69]
2PP	45 nm [77]	160 nm [76]	Liquid photopolymer resins	No

As can be seen from table 2.1, two techniques are particularly suitable for MMAM, being FDM and MJP 3D printing. Both of these techniques are capable of MMAM out of the box. The main problem with FDM 3D printing is its relatively low resolution, which is difficult to improve due to the minimum nozzle size a viscous thermoplastic filament can be pushed through. FDM 3D printing can achieve a vertical resolution of up to 20 μm and a lateral resolution of 100 μm, however in reality these values will be at least double of which is mentioned. Besides, this resolution is not repeatable for every shape [79]. Figure 2.17, adapted from Collingwood, Silva, and Arif [4], elaborates on the minimum channel size and minimum resolution for positive features. From this table, it can be seen that FDM has the largest minimum channel size with a very high surface roughness, compared to other techniques.

3DP process	Reported Minimum Channel Size	Reported Minimum Resolution for Positive Features	Reported Surface Roughness
MJ	205 µm [34] 250 µm [38]	270 µm [34]	0.99 [34]
DLP	154 µm [34] 200 µm [39] 250 µm [18]	94 µm [34] 200 µm [18]	0.35 µm [34]
SLA	300 µm [38]	–	–
FDM	500 µm [34]	250 µm [18] 321 µm [34]	8 µm [18] 10.97 µm [34]

Figure 2.17: Minimum channel size and minimum resolution for positive features, table adapted from [4]

Another downside of FDM 3D printing is that due to the circular shape of the filament and a layer-by-layer approach poor layer adhesion can occur using single or even multiple materials [80]. MJP 3D printing, in contrast to FDM, shows a very high resolution, which is promising for creating microchannels in microfluidic devices. However, MJP 3D printing limits the available resins to proprietary and low viscosity ones, this makes the process costly. Besides, custom resins are not easy to formulate.

2PP 3D printing shows a very high resolution, this technique is however expensive in contrast to other stereolitography methods. Other stereolitography methods such as DLP, LCD and SLA show comparable resolution to each other, but none of these techniques is suitable for MMAM out of the box. Therefore, modification of the 3D printing process, hardware and software is necessary to enable MMAM on these printers.

Preliminary research has shown that both SLA and DLP have been used succesfully for MMAM after modifications to hardware and software [50] [57]. However, SLA and LCD 3D printers are more suitable for modifying since the DMD chip of a DLP 3D printer can get dirty easily. Besides this clear advantage, the availability of SLA and LCD 3D printers is high and the prices for both resin and the 3D printer itself are relatively low. LCD is currently the cheapest technology and has the highest availability, resolution, and speed (due to plane illumination). Therefore, LCD 3D printing is the method of choice to create a novel high-resolution and multi-material protocol. Another advantage lies in the fact that a broad range of photoresins is commercially available for these techniques [79]. Materials with different transparency, opacity, different shore hardnesses and combinations of such material properties are possible to print using stereolitography 3D printing. The use of photoresins is a hallmark of SLA 3D printing, these photoresins are sensitive to UV light, under which they cure. This technique was first used by Hull in 1984 and has been improved ever since.

2.4. Photoresins

As stated in Hull's patent from 1984, the first photoresins were not meant for additive manufacturing [42]. The resin came from Loctite and was used as an UV curable adhesive, it consisted of urethane dimethacrylate with a small fraction of acrylic acid, benzophenone (photoinitiator) and methylethylhydro-quinone (MEHQ)/triallyl phosphate (to inhibit premature polymerization) [81]. Like other resins in every manufacturing process, the composition is build up out of a homogenous liquid mixture of photo-initiators, monomers, crosslinkers and fillers [32].

Hull kept working on this principle of photopolymerization, SLA, and found a way to cure resins that absorb light with a wavelength of 325nm efficiently using a He-Cd laser [82]. The first photocurable materials used for SLA consisted of an urethane dimethacrylate (UDMA), with a small amount of acrylic acid, benzophenone (used as photoinitiatior) and methyl ethyl hydroquinone/triallyl phosphate (to prevent premature polymerization) [82]. However, with future research it became apparent that a smaller amount of energy to reach gelation (the transition from liquid resin to a gel-like state) of the resin equals to faster 3D printing speeds [83].

The following equations for gelation are adapted from Ligon, Liska, Stampfl, *et al.* [41]. To reach gelation in a SLA 3D printing system, the critical exposure E_c is measured in mJ cm^{-2}. The equation for E_c is given below, with E_0 being the dose at the surface, C_d the depth of curing, D_p the depth of penetration.

$$E_c = E_0^{(-\frac{C_d}{D_p})} \tag{2.2}$$

D_p is given and defined as

$$D_p = 1/(2.3\epsilon[I]) \tag{2.3}$$

In which ϵ is the molar extinction coefficient at the utilized wavelength and [I] is the photoinitiatior concentration [84]. Ligon, Liska, Stampfl, *et al.* [41] argues that E_c is important, but the strength and young's modulus at the point of gelation are too low to survive additive manufacturing processes. To compensate for this lack of strength, excess energy is defined to provide sufficient "Green" strength. "Green" strength is the ratio of

strength of the firstly photopolymerized object in contrast to the final object (the final object is often cured). The equation of this excess energy is given as:

$$E_x = E_c\left(\frac{D_p}{C_d}\right)^{\left(\left(\frac{C_d}{D_p}-1\right)-1\right)} \tag{2.4}$$

The strength can be increased and the layer size can be decreased by use of UV or visible absorbers which are not involved in initiation, at the cost of a longer build time a higher vertical resolution can be obtained [41].

2.4.1. Radical Systems

Radical systems are composed of three steps, which are; Generation of the radical, initiation and propagation of the radical. To induce photopolymerization, photolytic energy is converted into reactive species by the photoinitiator. Radical systems are classified to be Norrish Type I or type II [85]. Commercially available photoinitiators often undergo the Norrish type I α-cleavage reaction, this reaction generates radical fragments when irridiated with a certain wavelength.

Radical generation, initiation and propagation are fast processes which makes them suitable for rapid prototyping [41]. Resins such as (meth)acrylate monomers and oligomers are commonly used in 3D photopolymerization processes that occur through a radical system. The most common meth(acrylate) monomers and oligomers are poly(ethylene glycol) diacrylate (PEGDA), urethane dimethacrylate (UDMA), triethylene glycol dimethacrylate (TEGDMA), bisphenol A-glycidyl methacrylate (Bis-GMA), trimethylolpropane triacrylate (TTA) and bisphenol A ethoxylate diacrylate (bis-EDA) [86]. Hull, Clarita, Spence, *et al.* [87] states that shrinkage and stresses can ultimately result to deformations in the 3D printed object, which can be an issue for high resolution applications. To overcome this limitation, advises the use of high molecular weight oligomeric acrylates, another downside (making the process more intricate) is the need for heating up the resin to reduce the viscosity [88].

For 3D polymerization techniques such as DLP, which use a higher wavelength light source, acyl phosphine oxides are the preferred photoinitiatiors [89]. It is concluded from both Ligon, Liska, Stampfl, *et al.* [41] and Bagheri and Jin [86] that a photoinitiator with a lower energy level $\pi*$ corresponds to a higher wavelength to initiate the generation of the radical.

Bagheri and Jin [86] also discusses the use of Thiol-ene and Thiol-yne systems, where acrylates can have problems regarding oxygen inhibition (especially in open vat SLA 3D printers), thiol-ene chemistry can reduce the oxygen inhibition. The oxygen inhibition is thus the first advantage, the second advantage is a lower shrinkage stress and thirdly thiol-ene systems show higher biocompatibility than (meth)acrylates. Thiol-ene resins can for example be bought from Norland Optical Adhesives, which has been used extensively by research groups using SLA and 2PP 3D printing processes, using photon sources (lamps) with 320 to 380nm wavelengths [41].

2.4.2. Cationic Systems

Cationic systems often employ commercially available epoxy monomers such as 3,4 epoxycyclohexane)methyl 3,4 epoxycyclohexylcar- boxylate (EPOX) and bisphenol A diglycidyl ether (DGEBA) [86]. The compounds used are thermally stable and will decompose under influence of UV radiation into a mix of cations, radical cations and radical intermediates [41]. The molecular structure of these monomers is very important, because their reactivity differs, fast polymerization can be achieved using cycloaliphatic epoxides [90]. In SLA based systems, 1,4-cyclohexane dimethanol divinyl ether (CDVE) is a commonly used material [91]. The main advantage of using epoxide monomers in photopolymerization 3D printing is the low volumetric shrinkage [86]. Lapin, Snyder, Sitzmann, *et al.* [91] describes the shrinkage to be only 2-3% volumetric. Therefore, epoxides are very commonly used in photobased additive manufacturing, they show good mechanical properties and can be postcured using heat or light, whereas (meth)acrylate-based resins can only be postcured using light [41].

However, epoxides have a much slower polymerization rate than acrylates and have been used in SLA 3D printing in combination with much more reactive cationic polymerizable vinyl ether monomers [91]. The vinyl ethers will polymerize very quickly and harden acceptably, while the epoxide will minimize the shrinkage during post curing. For example, disubstituted oxetane (DSO) monomers show even higher reactance than epoxides and provide almost identical low shrinkage [92].

2.4.3. Hybrid Photopolymerization Systems

In addressing the challenges of rapid and inhomogeneous shrinkage eventually leading to curl, distortions and ultimately a product that will not meet it's desired specifications, a strategic approach involves the use of hybrid polymerization systems. This can be solved by incorporating multiple types of monomers, each providing different rates of reaction. A less reactive monomer has less curl and distortion and can be postcured afterwards. A mixture does not necessarily have to be only cationic or radical, a hybrid formulation can contain both systems. These mixtures of both radical and cationic monomers and initiators have been widely accepted in the industry [93].

2.4.4. Suitable Photoresins

Suitable photoresins for microfluidic manufacturing must comply with several material requirements. Material requirements such as transparency and biocompatibility are important considerations in microfluidics and form the basis for advanced applications in microfluidic systems. Besides, to create multi-material compliant microfluidics, requirements exist such as (transparent) materials with high elasticity and stretchability [94]. Commercially available UV curable resins possessing elastomeric properties, which can be used in either SLA or DLP 3D printing to create soft membranes, are for example Carbon EPU 40, Stratasys TangoPlus, Formlab Flexible and Spot-A Elastic [95]. To create a PDMS-like membrane, the young's modulus of this soft membrane material must be in the same order of magnitude as the young's modulus of PDMS, this way a soft membrane can be 3D printed. The young's modulus of PDMS is given to be 600 to 1400 kPa (0.6 to 1.4 MPa), depending on the thickness [96]. However, soft materials are often characterized by their shore hardness. For PDMS, 40 shore A is a suitable shore hardness [97]. A suitable SLA photoresin with a shore hardness in this range (43 shore A) is "Liqcreate Elastomer-X" [98]. The rigid part of the microfluidic valve can be created out of commercially available clear resin such as "Anycubic high clear" or "Anycubic clear". To obtain sufficient bonding between the rigid and soft part during the fabrication of multi-material microfluidic valves, Song, Chen, Hou, *et al.* [11] states that both resin formulations must consist of a high concentration of acrylate monomers. As a result, strong interlinking (due to covalent bonding) decreases the risk of delamination. Besides strong bonding at the interface, the first layer must adhere to the build platform, which can be ensured by using a longer exposure time for the first layer [79]. The downside of these commercially available UV curable resins are the fixed mechanical properties and the low value of elongation at break [95]. To gain more flexibility from the soft material, a monofunctional monomer of epoxy aliphatic acrylate (EAA), a difunctional cross-linker (aliphatic urethane diacrylate (AUD)) and a thermoplastic polyolefin (TPO) were used to create a custom elastomer resin, which resulted in a 5 times higher stretchability than the commercially available UV curable resins [95].

Others have found materials such as ethylene glycol dimethylacrylate (EGDMA) and bisphenol A glycerolate dimethacrylate (BAEDA) suitable for use as a curable base material in Multi Material Stereolitography [99] [100], accompanied by a photoinitiator which cured at 350 to 430 nm (Diphenyl(2,4,6-trimethylbenzoyl)phosphine oxide (TPO)). Khatri, Frey, Raouf-Fahmy, *et al.* [79] states that an optimal resin for SLA 3D printing has a viscosity (at ambient temperature, i.e. around 25°C) below 0.2 Pas, however an increase in temperature will also lead to a lower viscosity, making it possible to use thicker resins using a heated vat for SLA 3D printing.

Like the research from Patel, Sakhaei, Layani, *et al.* [95], Khatri, Frey, Raouf-Fahmy, *et al.* [79] have researched the effect of TPO contents and have found a significantly higher ultimate tensile strength when increasing the amount of TPO in the resin, a maximum failure strain of around 3.5% has been found at 1 wt.%. An increase of the photoinitiator results in a system consisting of a high cross link density, which results in an increased ultimate tensile strength and a decreased maximum strain.

2.5. Multi-Material LCD 3D Printing

Multi-material 3D printing refers to additive manufacturing which exploits several materials within a single step fabrication process. This single step fabrication process can be performed by use of LCD 3D printing, which makes the process not only cost effective, but also scalable. As stated before, 3D printing techniques such as SLA, DLP and LCD are out-of-the-box only suitable for single-material fabrication processes. To process two or more different materials in a single 3D printed object, one must be able to (manually or automatically) switch materials during the printing process. To enable multi-material additive manufacturing on these types of printers, techniques such as the print-pause-print method or the layer-on-demand method can be used. Utilizing these methods, several multi-material structures have been created already, such as magnetically activated microfluidic devices by Nakahara, Suzuki, Hosokawa, *et al.* [101] and Lazarus, Bedair, and Smith [102], and hydrogel valves with a porous film by Al-Aribe and Knopf [10]. Additional information on both techniques will be provided in the following subsections.

2.5.1. Print-pause-print

A research exploiting the print-pause-print principle to create pneumatic actuators using vat based stereolitography was conducted by Song, Chen, Hou, *et al.* [11]. 3D printed micro-actuators can for example be used for soft robotics [103], microfluidics [104] and biomedical engineering [105]. This print-pause-print technique is used for multi-material 3D printing (MMAM) and can be performed by using multiple resin vats, the object is transferred from one vat to the other during building, an early study on this subject consisting of multiple vats in a rotating carousel was already published in 2006 [106], [107]. Besides multi-material layers, multi-material structures within the same layer becomes possible using multiple vats [32].

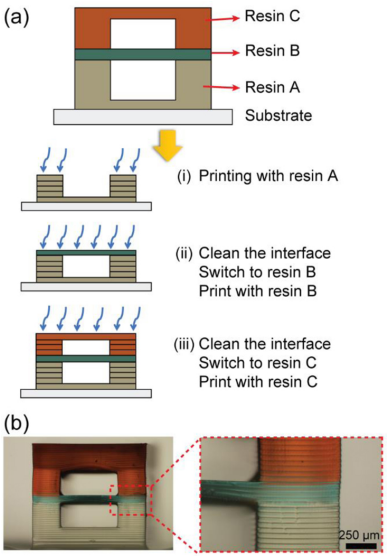

Figure 2.18: (a) Schematic of multi-material 3D-printing procedure with three different resins using print-pause-print (b) Two 3D printed channels, picture adapted from [108].

Multi-material vat polymerization exploits the print-pause-print method, which is nicely elaborated on by Robles-Martinez, Xu, Trenfield, *et al.* [50], where a multi layer polypill containing multiple drugs was created using this method. Robles-Martinez, Xu, Trenfield, *et al.* [50] states that the following steps were performed: (1) gain manual control over the 3D printer using the OpenFL version of PreForm software, which enables pausing and raising the build platform to allow switching of the vat, (2) resume printing after changing the vat, (3) between changes of the vat a deionised water rinse is necessary to avoid cross-contamination of resins.

Pausing the 3D printer and lowering or elevating the build platform may lead to an alignment error. Therefore, the precision of the Z-axis must be elaborated on. Inamdar, Magana, Medina, *et al.* [106] claims a precision in vertical direction (z-direction) of around 20 µm, with a repeatability (the precise reproduction of a process or measurement under the same conditions) of around 1 µm, this has however not been verified on the printed test samples. Another system consisting of syringes to exchange resins has been researched, however manual cleaning and rinsing of the vat was still necessary, using this technique a minimum thickness of 21 µm was aquired [109]. Using this technique, more curable materials such as polyethylene glycol (PEG) based hydrogels and conductive materials could be used [110]. In 2011 another MMAM SLA system using a DMD chip has been presented by Zhou, Chen, Yang, *et al.* [111], by using a vat change and 2 different polyethylene diacrylate based hydrogels, a sub-millimeter sized object could be achieved. Another study by Kim, Castro, Bhattacharjee, *et al.* [112] shows printed microchannels with dimensions of 200 µm using this technique.

To assess the layer formation between multiple materials, it can be helpful to add fluorescent dyes, when dissolved in the base resin these dyes help visualize the normally transparent parts. However, adding such dyes to the resin calls for the need of longer exposure times, this is due to the absorption characteristics of the material, a 30 second layer exposure time instead of the usual 3 seconds to 5 seconds has been reported by Khatri, Frey, Raouf-Fahmy, *et al.* [79]. In this study a minimum XY-resolution of 30x30 μm^2 has been found, with an aspect ratio of 1 to 5, using two different resins the smallest features have been found to be in the 200-300 µm range. Another aspect of SLA 3D printing is described, which is the occurence of micro cracks due to internal stresses induced by the polymerization process, decreasing the risk of micro cracks can be done by varying the light intensity and the exposure time. Khatri, Frey, Raouf-Fahmy, *et al.* [79] recommends to look into the assembly of high precision positioning elements such as better lead screws or more precise stepper motors, because most print defects are related to alignment issues.

To disregard these alignment issues, a small change in working principle should be made. As stated by Song, Chen, Hou, *et al.* [11], using a single vat in which the resin is changed and the object is cleaned inbetween resin changes eliminates the alignment error (due to the object not changing position) in the spatial plane. Other recommendations for improvement of the multi-material 3D printing process are for example: measuring the layer thickness vs exposure energy, this gives the required exposure time for a given layer height, rinsing the material between material changes with ethanol or 2-propanol, washing the 3D printed object (with water, isopropanol and ethanol) in an ultrasonic bath, drying in the oven and to check if the elastic properties degrade after exposure to UV light for different periods of time [11]. Possible drawbacks such as differences in reactivity (thermal or rheological) or incompatibilities of materials may arise and should be taken into account [113].

2.5.2. Layer-on-demand

The layer-on-demand approach is characterized by a thin layer of material which is provided as needed [32]. To generate such a layer, several methods are described such as: a fluidic cell or microfluidic cell [114], [115], liquid deposition by a syringe [116] and VLM (viscous litography manufacturing) [117]. The layer-on-demand approach is able to quickly switch from one material to another, it is stated by An and Leong [32] that uncured resin can be cleaned or recycled.

The layer on demand method as described by Kowsari, Akbari, Wang, *et al.* [116] can be seen in figure 2.19. The layer puddle is deposited by syringes, the build plate can selectively lower into both created puddles (material A and material B). When the puddle is exposed to UV light with a wavelength of 405 nm, the layer is formed and the object can be cleaned using compressed air after the build plate is raised by 5 mm, after which the process repeats itself until the object is finished. This technique requires custom coding in Labview to control the electronics of a purpose built DLP apparatus.

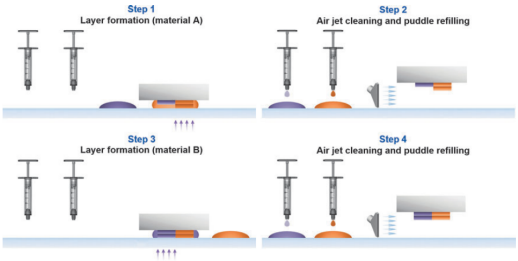

Figure 2.19: Steps required to create a multi-material structure using the layer-on-demand method on a custom DLP apparatus, picture adapted from [116].

VLM on the other hand, requires a roller to pick up the resin which is laminated to the bottom of a transparent film. This resin is transported to the printing area, where the build plate rises and presses up against the resin. UV light is used to cure the resin which is between the build plate and the laminated area, creating a specified layer thickness. After these steps, the build plate lowers and consequently peels the cured resin from the transparent film, as stated before the uncured resin can be recycled by transferring it back to the resin reservoir **VLM**, [118].

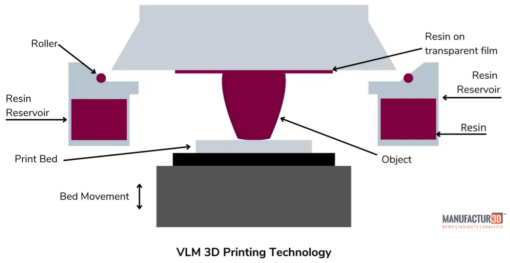

Figure 2.20: VLM 3D printing using the layer-on-demand approach, picture adapted from [118].

2.6. Research gap

Several fabrication methods have been discussed for the development of microfluidic devices and their manufacturing methods. However, there are still challenges, particularly in the fabrication of both high-resolution and multi-material microfluidic components. Traditional microfluidic fabrication methods, such as replica molding, injection molding, and hot embossing are well-established but suffer from inherent limitations. They all rely on multi-step processes, cleanroom environments, and alignment issues that hinder the integration of complex designs. These limitations constrain scalability, affordability, and the ability to fabricate and iterate rapidly.

Relevant studies have highlighted the potential of 3D printing as an alternative manufacturing technique, offering flexibility, rapid fabrication, and reduced process complexity. However, current 3D printing technologies face critical trade-offs. High-resolution techniques, such as SLA and DLP, are often limited to single-material printing or require extensive modifications to achieve multi-material capabilities. On the other hand, methods like MJP support multi-material additive manufacturing (MMAM) but are expensive and require special resins. Furthermore, adhesion between printed materials and the optimization of interfaces in MMAM remain untouched areas.

While prior work has demonstrated the feasibility of (M)SLA/DLP 3D printing to create multi-material microfluidic systems, **there is a lack of standardized protocols for achieving high-resolution MMAM with seamless material integration**. Additionally, **scalability and affordability remain under-explored areas**, especially in the context of biomedical and diagnostic applications where cost-effective and precise manufacturing methods are critical. This research addresses these gaps by developing a novel MMAM protocol tailored for the fabrication of multi-material microfluidic valves, focusing on material properties, enhancing resolution, material compatibility, and process scalability.

3

Research Questions and Project Outline

The scope of this research is to create a novel 3D printing protocol which enables to create high-resolution multi-material integrated microfluidic devices with a single step fabrication process. This protocol is expected to contribute to the further development of microfluidic devices and enable for applications in various fields such as biotechnology, medicine, and analytical chemistry. Some requirements are a high resolution, good scalability, affordability, elimination of the alignment error and good compatibility between various materials.

3.1. Research Questions

Hypothesis:

- In this thesis, it is hypothesized that a novel 3D printing protocol can be created which meets or exceeds the expectations in the fabrication of microfluidic valves using LCD 3D printing.

Main question:

- How to develop a novel 3D printing protocol which enables for the fabrication of a high resolution multi-material microfluidic device in a single step fabrication process?

Subquestions:

- Which 3D printing protocol can be used to develop a high-resolution multi-material microfluidic structure?
- How do the 3D printing process parameters influence the resolution of microfluidic channels in multi-material microfluidic structures?
- How do the 3D printing process parameters influence the mechanical properties of MSLA (LCD) 3D printed multi-material structures?

A microfluidic valve consists of a thin membrane which blocks a channel. For a multi-material microfluidic valve, the membrane is created out of a soft polymer, whereas the body is created out of a rigid polymer (see Figure 3.1).

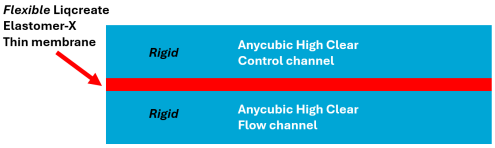

Figure 3.1: Diagram of a multi-material microfluidic valve and its materials.

Inspired by the recommendations of Qian, Hou, Li, *et al.* [6], certain important requirements for microfluidic valves have been highlighted. This primarily includes the preference for lightweight materials, with a particular emphasis on polymers. A list of requirements is provided below.

1. Multi-material, due to the soft membrane and the rigid body, a difference in Young's modulus between both materials is essential
2. Transparency for visualization

3. Sufficient material adhesion or bonding between different components/layers
4. 3D printable using an LCD 3D printer
5. High resolution/precision, minimum channel size of 50-100 µm
6. Cost effective
7. Elimination of the alignment error
8. Low leakage rate, preferably zero leakage

3.2. Methodical Approach

3.2.1. Materials and Equipment

In this Subsection, an overview of materials and equipment is provided.

- **Stereolitography MSLA 3D printer** - The printer of choice is an Elegoo Mars 4 9k, this printer is chosen due to its availability, high resolution (18 µm) and relatively low cost of both the 3D printer and the materials which it can process.
- **Printable resolution block** - The printable resolution block is used to gain insight in the printers' capabilities, the minimum feature size is assessed for both wells and extrusions as shown by [119]. The model consists of a rectangular block with lines of various widths in horizontal, vertical, and diagonal directions to avoid a directional bias [120].
- **3D CAD software** - Solidworks is used to create all CAD models.
- **Slicer software** - Lycheeslicer and Chitubox are used to slice STL files.
- **Photoresins** - Anycubich High Clear and Liqcreate Elastomer-X.
- **UV curing device** - A Formlabs Form Cure is used for UV post-curing.
- **Cleaning solvent** - Isopropanol alcohol is used to rinse 3D printed objects and clean the build plate and resin vat.
- **Ultrasonic cleaning** - A Sonorex ultrasonic cleaner is used for seperate parts. A Nanografi Ultrasonic Processor is used for parts attached to the build plate (during print-pause-print).
- **Digital microscope** - To clearly visualize and measure the resolution and minimum feature size, a Keyence VHX-6000 Digital Microscope is used.
- **Data analysis software** - To analyze the resolution of samples, the free software ImageJ is used [120].
- **Tensile testing device** - A Zwick Roell Z005 tensile testing device is used for tensile testing.
- **Safety equipment** - Safety equipment consists of gloves and protective eyewear.

3.2.2. Resin preparation

A rigid and a soft (flexible) resin are chosen to create a microfluidic valve. Anycubic High clear, a rigid resin, is used to create the body of the microfluidic valve. Liqcreate Elastomer-X, a soft resin, is used to create the flexible membrane.

Both materials are acrylate based, this ensures covalent bonding of both materials. The red dye is used to visualize the membrane layer, during operation this membrane should be distinguishable from the transparent Anycubic High Clear layers. Besides, the mechanical properties of dyed Liqcreate Elastomer-X are compared to their non-dyed counterparts.

3.2.3. Material Characterization

Tensile testing is performed using the Zwick Roell 005 to characterize both materials separately and the combination of both materials in a multi-material sample. Using Hooke's law, the young's modulus of both materials is determined, graphs are made of several dog-bone-shaped specimen. For the multi-material dog-bone-shaped specimen, the tensile strength is used to draw conclusions about layer bonding.

3.2.4. Printing Parameter Optimization

The printing parameter optimization starts with the design of the designed resolution block, the model is created with grooves of various widths in horizontal, vertical, and diagonal directions to avoid a directional bias [120]. This resolution block is used to measure the dimensional accuracy and the minimum feature size (by use of a VHX-6000 Digital Microscope and ImageJ). Only Anycubic High Clear is evaluated using this approach, because the channels will be created out of this material. The output of this stage is a graph which covers the intended size vs the measured size, as described by Wang, Enders, Preuss, *et al.* [119]. After graphing the data, conclusions are drawn on how to minimize channel sizes using known and documented settings.

3.2.5. Multi-material 3D Printing

To enable MMAM on the Elegoo Mars 4 9K, a pause step is initiated using the UVTools software. Afterwards, the printer is paused using its firmware and the build plate and object are cleaned using a Nanografi Ultrasonic Processor. After this cleaning step, a new vat containing the second material is placed and printing is resumed.

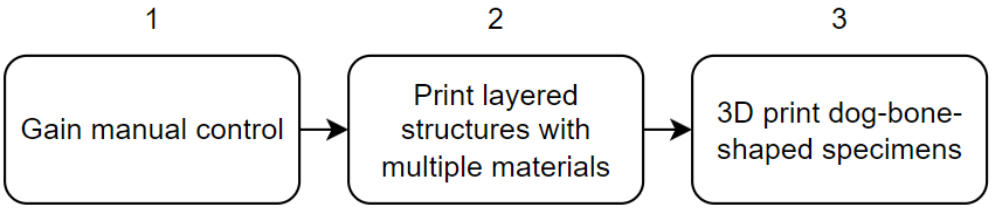

Figure 3.2: A schematic overview of the 3D printing process. First, manual control over the 3D printer is obtained, to allow for the print-pause-print method. Second, layered structures with multiple materials are printed using this method. Lastly, 3D printed dog-bone-shaped specimens are created to evaluate the material properties using tensile testing.

After printing the multi-material dog-bone-shaped specimens, post-processing of the 3D printed structures is executed by cleaning and post-curing them. After post-processing, the structures are ready to be tested in a tensile testing setup (as described previously).

3.2.6. Design a multi-material microfluidic valve

A multi-material microfluidic valve is designed using Solidworks. The design is based on the Quake valve with incorporated desired features and functionalities suitable for 3D printing. Directions of channels, width and height of channels and membrane diameter are taken into account in this design. The membrane's performance is theoretically proven using a FEM analysis and an analytical approach.

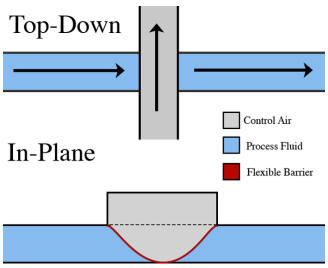

Figure 3.3: The basic working principle of a Quake valve. The control channel and flow channel are separate channels, the flexible membrane expands when pressure is applied to the control channel, which blocks the flow channel. Picture adapted from [121]

3.3. Project Outline

This thesis explains the development of a novel multi-material 3D printing protocol using a stepwise approach. **Chapter 4** of the thesis consists of the optimization of the print process, incorporating several aspects such as geometrical dependency on exposure times and the investigation of mechanical properties for both Anycubic High Clear and (dyed) Liqcreate Elastomer-X. **Chapter 5** of this thesis is dedicated to the minimum channel size which can be reproduced by an affordable MSLA 3D printer. Chapter 5 also discusses the design of a resolution block and its application to find the minimum groove width. **Chapter 6** discusses the steps required to obtain multi-material structures, the stepwise protocol is based on the print-pause-print protocol, and is adapted to print

a multi-material dogbone. This dogbone is tensile tested to assess the layer bonding between both materials. In **chapter 7** the creation of the microfluidic valve is discussed, this valve is designed and FEM simulated in Solidworks, an analytical approach is used to check these FEM simulations. In **chapter 8** an overview of the conclusions from this thesis is provided and future work is discussed.

4

Print Process Optimization

This chapter aims to optimize the printing process for both Anycubic High Clear and Liqcreate Elastomer-X seperately, before expanding the research to multi-material 3D printing. First, the objectives are defined in Section 4.1. Secondly, an overview of parameters and performed measurements is provided in Section 4.2. The results are presented in Section 4.3 and lastly a conclusion is drawn in Section 4.4.

4.1. Resin characterization objectives

The primary objective of this chapter is to characterize the rigid material (Anycubic High Clear), which is used to create the valve's body, by examining the relationship between exposure time and feature size. This chapter aims to determine how variations in exposure time influence the accuracy and resolution, and mechanical properties of 3D printed features, providing insight into optimal settings to achieve a desired level of detail and strength. Additionally, the ease of printing of dyed resins is investigated, assessing how the introduction of a red dye influences print quality and exposure time requirements. The aim of this section is to combine the objectives to answer the following research question: *How do the 3D printing process parameters influence the resolution of microfluidic channels in multi-material microfluidic structures?*

4.2. Materials and methods

This section discusses the parameters and measurements of several 3D printed samples.

4.2.1. Anycubic High Clear

XP2 Validation Matrix

The body of the multi-material microfluidic valve will be created out of Anycubic High Clear. In this Subsection, this resin is used to print the XP2 validation matrix [122] (see Figure 4.1a), which is designed by Photonsters to determine the optimal exposure time for accurate feature replication. The XP2 Validation Matrix includes several features such as holes, pins, bars, and grooves which can be seen from Figure 4.1b.

The STL file is sliced using the LycheeSlicer software, with the layer height set to 0.01 mm (see Figure 4.2). The exposure time is varied between 1 and 15 seconds to identify the exposure time that produces the most accurate features.

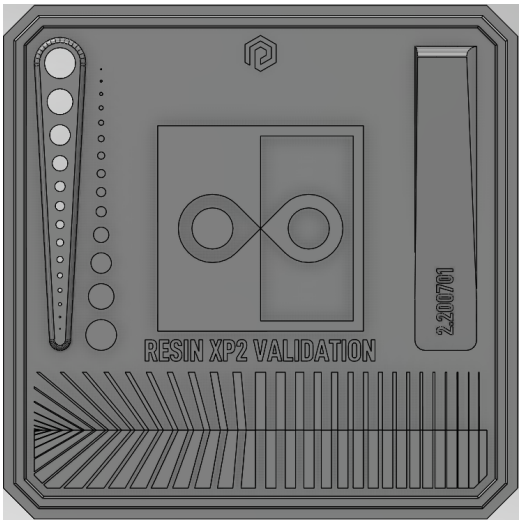

(a) Photonsters XP2 Validation Matrix to find the right exposure time.

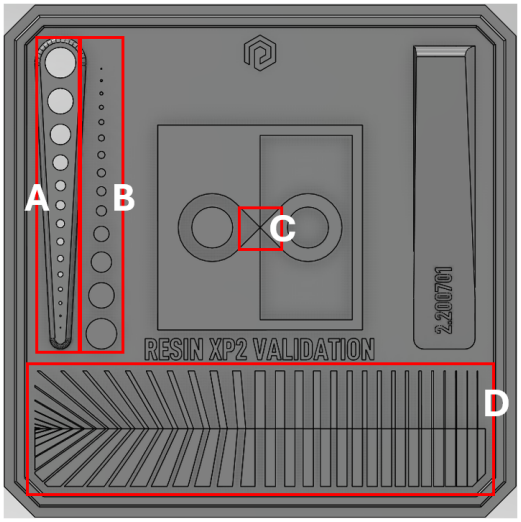

(b) (A) holes, (B) pins, (C) connecting halves of the infinity sign, (D) bars and channels.

Figure 4.1: The XP2 matrix and its relevant features.

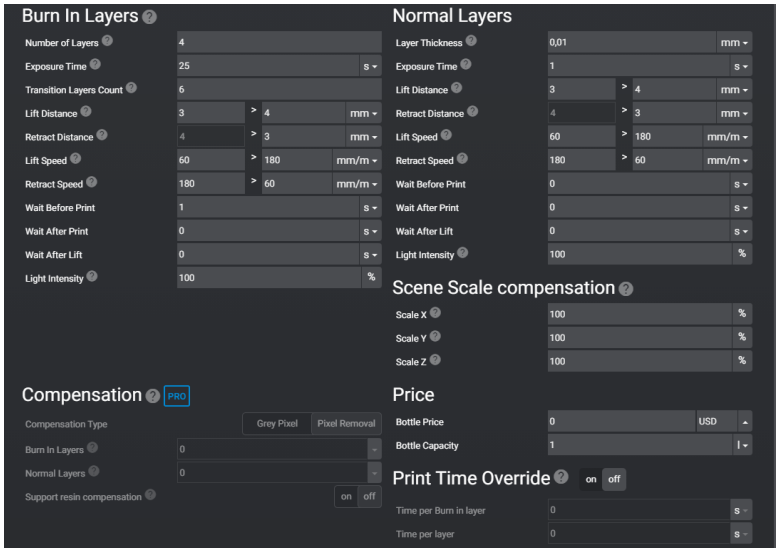

Figure 4.2: Settings in Lychee slicer for Anycubic High Clear

XP2 validation matrix measurements

To assess the accuracy of the 3D printed features on the XP2 validation matrix, the largest hole, pin, bar, and groove are measured using the Keyence VHX-6000 Digital Microscope. Measurements are performed using the built in measurement tools of this microscope. The largest features are chosen, because discrepancies in size will occur due to the nature of STL files, round objects are merely straight lines connected to each other to form a circle. It is observed that smaller diameter circles consist of less straight line segments and larger diameter circles consist of more straight line segments, which can be seen from Figure 4.3a and Figure 4.3b respectively. This means that larger holes or pins have more line segments and are therefore a more accurate representation of a certain shape.

The measurements are repeated three times to minimize measurement errors and are compared to their intended size as found in the STL file (as measured in Solidworks). The measurements with the digital microscope were taken for the largest hole (3000 µm), largest pin (3000 µm), largest bar (1000 µm), and largest groove (999.1 µm). The graphs contain the exposure time on the X-axis and the measured size on the Y-axis, revealing the relationship between exposure time and accuracy. The standard error of the mean is calculated for each measurement and added to the graph.

Post processing

After the 3D printing process, all samples are cleaned using a Sonorex ultrasonic cleaner which is filled with demineralized water. The samples are submerged in IPA in a plastic beaker, this beaker is inserted in the

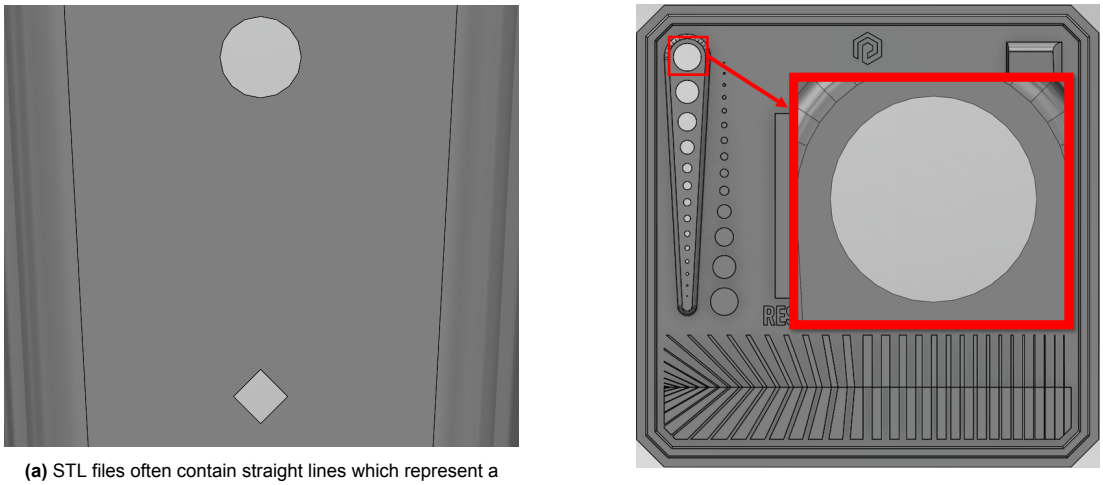

(a) STL files often contain straight lines which represent a circle, on the bottom of this figure it can be seen that for very small holes the software creates a rectangle.

(b) More straight line segments lead to more accurate circles.

Figure 4.3: A comparison between straight line segments in an STL file.

ultrasonic bath for 10 minutes. This ensures that the printed parts are clean and free of any residual uncured resin, which could otherwise interfere with the measurements.

4.2.2. Liqcreate Elastomer-X

Print settings

The membrane of the multi-material microfluidic valve is created out of Liqcreate Elastomer-X. This is a 3D printing resin which is developed specifically for producing flexible, rubber-like parts where elasticity and durability are of key importance. Even though this is a specialty resin, it can be used for SLA, MSLA, and DLP 3D printers with a wavelength of 385 to 420 nm, making it compatible with a range of affordable printers such as the Elegoo Mars 4 9k which is used for this research. Due to the resin's soft and IPA absorbing nature, XP2 matrices are difficult to measure accurately, it is recommended by Liqcreate to use the optimal settings for a 50 µm layer height which are provided by Liqcreate and can be seen from Figure 4.4.

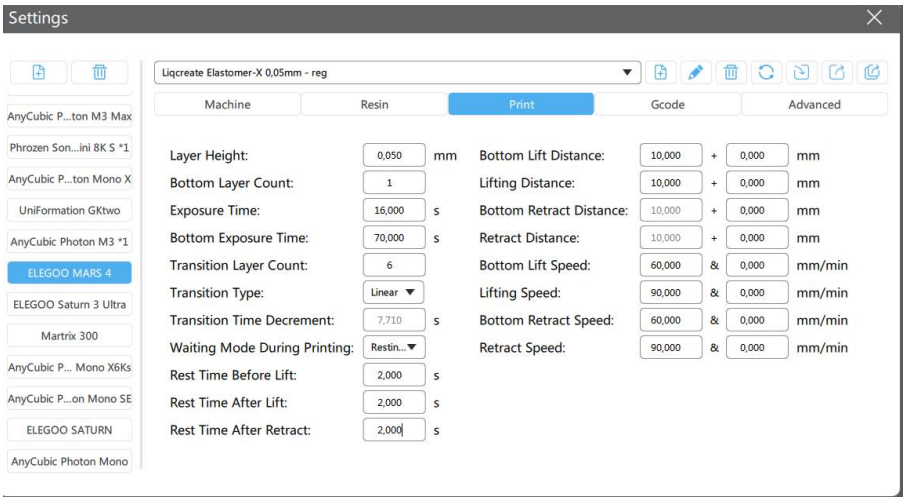

Figure 4.4: Recommended settings for Liqcreate Elastomer-X, using the settings provided by Liqcreate after contacting them directly.

Ultrasonic cleaning and swelling test

To investigate the effects of IPA absorption on dimensional stability, a sample strip of Liqcreate Elastomer-X resin with 1 wt% of red dye is prepared with dimensions of 1 cm by 2 cm and a thickness of 0.4 mm, this design is created in Solidworks. These samples are used to determine the optimal cleaning time, measure dimensional changes after an ultrasonic IPA bath and to determine the time required for the sample to shrink back to its original dimensions. Additional images of this process are provided in Appendix C.

After a 30-minute ultrasonic IPA bath, the sample's length is measured using a ruler. The length of the samples is monitored over a 4-hour period to observe the shrinkage. The measurements are conducted at both ambient temperature (27°C) and at 50°C within a heated enclosure to assess the effects of temperature

on the shrinkage rate. Each measurement was captured by photographing the sample and creating a scale bar in ImageJ using a ruler as a reference.

Preparation of Dyed Elastomer-X Samples

The colorant of choice is the color ”traffic red” from 3D Jake, this company offers a wide variety of colors which are also discussed and used by Liqcreate. 3D Jake states that the maximum amount of colorant should be equal to or less than 2.44 wt%, this corresponds to 25 g of colorant with 1000 g of resin [123]. Higher amounts of colorant could potentially lessen the printing quality or material properties. This is in line with statements from Liqcreate, properties of the resin can change due to the addition of a colorant. Therefore, weight percentages of colorant should not exceed 2.5 wt% [124], because pigment stability, print speed and mechanical properties can be impacted drastically. To use this colorant, several best practices are described by the manufacturer (3D Jake) and are listed below.

1. Shake the bottle of resin colorant for 15-20 seconds.
2. Pour the colorant into the resin and shake or stir until a homogeneous mixture is obtained.
3. Leave the resin for a few minutes to remove air bubbles.
4. When the resin has been stored for a while, it should be shaken or stirred before use.

Liqcreate states that the colorant and resin should both be homogeneous (mixed properly) before mixing the two together, otherwise it becomes impossible to duplicate results. It is stated that translucent pigments will not alter the mechanical properties or the printing behavior. These problems only occur when colorants block or absorb the emitted UV light coming from the LCD screen. When printing at 405 nm, this might occur using the colors yellow, orange, black and other opaque colorants [125]. However, opaque resins block UV light and therefore reduce light bleeding, which in turn has a positive effect on the accuracy. A trade-off between opaqueness (contrast) and printing properties has to be made.

The resin is mixed using a plastic cup, wooden stick and a calibrated scale. The Liqcreate Elastomer-X is shaken and poured into the cup to the desired amount, any excess is removed using a syringe. The red dye is shaken and extracted from the bottle using a pipette, several droplets were meticulously dispensed into the resin to the desired amount. The resin was gently stirred with a wooden stick, carefully blending the droplets to achieve a homogeneous mixture without introducing bubbles. The dyed resin is assessed for 1, 2 and 3 wt% respectively. For example, to create a red resin with 1 wt% of red dye, 0.5 g of red dye is added to 49.5 g of Liqcreate Elastomer-X resin, of interest are the color (contrast) and the ease of printing.

4.2.3. Tensile testing

Preparation of dog-bone-shaped specimens

For tensile testing, dog-bone-shaped specimens, also referred to as tensile bars or simply dogbones, were used to perform tensile testing. This design, developed and distributed by staff at the TU Delft, has a total length of 100 mm, a width of 12.0 mm, and a thickness of 2.00 mm, with a narrower section in the middle of 6.00 mm wide. This narrow section is called the gauge length (effective straining region) and equals approximately 30.6 mm when measured in Solidworks. The specimen with its respective measurements taken in Solidworks can be seen from Figure 4.5. The most important measurements are the gauge length and its respective area.

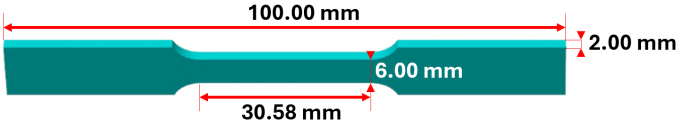

Figure 4.5: Measurements of the provided dogbone design.

To improve build plate adhesion and ensure stability during printing, a raft was designed in Solidworks and added to the base of each dogbone (Figure 4.6). This raft negates the need for additional support material, simplifying the post-processing phase while enhancing print reliability. Post-curing of these dogbones is performed using a Formlabs Form Cure. Anycubic High-Clear samples are post-cured for 5 or 30 minutes. Liqcreate Elastomer-X samples are post-cured for 5 minutes in demineralized water, followed by 0, 30 or 60 minutes of dry post-curing.

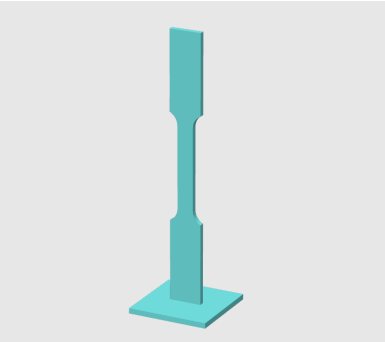

Figure 4.6: A raft has been added to enhance build plate adhesion.

Tensile testing procedure

The 3D printed dogbones are tested on a Zwick Roell Z005 tensile testing machine, which provides stress-strain data in the form of a .TRA file. This file is imported into Matlab to extract the data and to generate stress-strain curves. From these curves, the Young's modulus is calculated using a linear fit in Matlab. The Young's modulus is a key parameter that indicates a material's resistance to deformation and provides a basis for subsequent FEM simulations. In short, the Young's modulus describes the relationship between force per unit area (stress) and the proportional deformation of an object (strain).

4.3. Results and discussion

This section discusses the results of measuring the digital microscopy images of XP2 matrices and the tensile testing of dogbones, both printed using Anycubic High Clear resin.

4.3.1. Anycubic High Clear

Hole size vs exposure time

The size of the largest hole on the XP2 matrix, initially designed to be 3000 µm in diameter, is measured across various exposure times ranging from 1 to 15 seconds. The results show a clear trend, when the exposure time increases, the measured hole size decreases. This suggests that the hole size is inversely proportional to the exposure time. This is likely due to over-exposure (and thus over-polymerization) of the resin. It can be observed from Figure 4.7 that the red line, which is the intended size of 3000 µm is not reached for any amount of exposure time. This is likely due to light bleeding, which can be explained by the fact that scattered or diffused light unintentionally cures resin beyond the boundaries of the desired area, reducing precision and causing features to deviate from their intended dimensions.

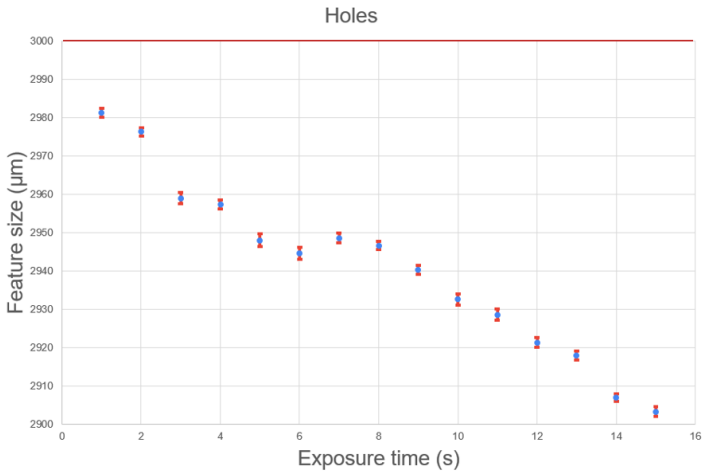

Figure 4.7: Hole size vs exposure time.

Pin size vs exposure time

For the largest pin on the XP2 validation matrix, which also has a size of 3000 µm, the results show that the measured size increases when the exposure time is increased. The perfect exposure time, where the measured size is equal to the intended size (red line), is approximately between 11 and 12 seconds according to the graph

which can be seen from Figure 4.8. Beyond this exposure time, the pin size begins to exceed the intended size, reaching sizes of almost 3050 µm, which indicates overexposure of the resin.

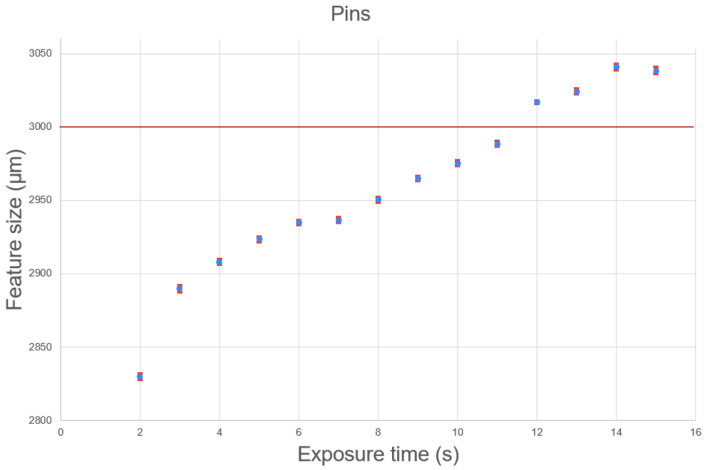

Figure 4.8: Pin size vs exposure time.

Bar size vs exposure time

The largest bar, located under the ”v” of the text ”validation matrix” on the XP2 matrix, is intended to be 1000 µm wide. The results from Figure 4.9 show that for exposure times of 3 to 4 seconds, the measured bar size closely matches the intended size (red line). As the exposure time is increased, the measured bar size grows far beyond the intended dimensions with measured sizes reaching almost 1070 µm. This can be explained by the broadening effect caused by overexposure, which causes the bar to expand in size. It is also observed from 4.9 that the distribution of data points is less linear than for other features. This is likely due to light bleeding, and refraction, which occurs when light travels through different media, such as the uncured-cured interface. The refraction index of cured resin is different than for uncured resin [126] and is thus a viable explanation for the nonlinear behaviour which occurs for features which are very close to each other.

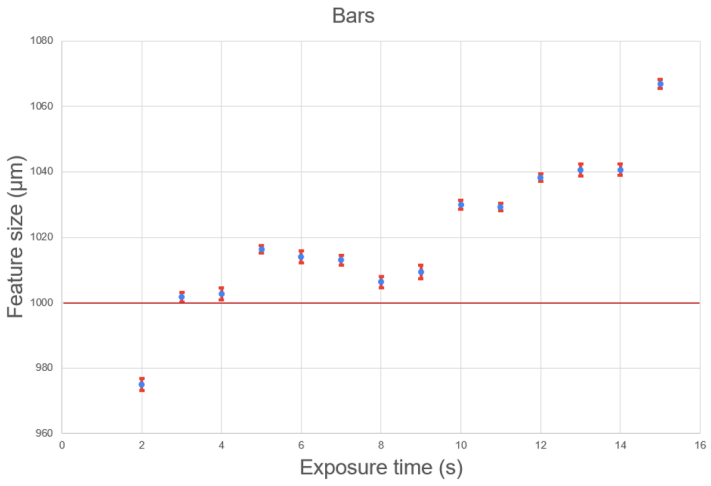

Figure 4.9: Bar size vs exposure time.

Groove size vs exposure time

The largest groove, intended to be 999.1 µm, is measured for various exposure times. The results from Figure 4.10 reveal that the groove size closely matches the intended size (red line) around 3, 4 and 5 seconds, with 4 seconds resulting in the closest match between intended size and measured size. When the exposure time increases beyond these ranges, the groove size decreases. This is likely due to overexposure causing the extrusions around the channel to broaden.

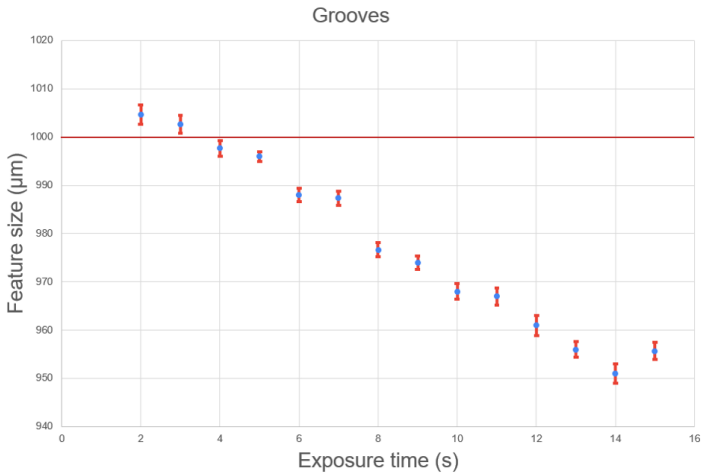

Figure 4.10: Groove size vs exposure time.

Observations and optimal exposure time

The found results indicate that exposure time plays a crucial role in determining the accuracy of 3D printed features. Shorter exposure times result in incomplete curing or under-exposure, leading to smaller sizes than intended, whereas longer exposure times do the exact opposite. A clear difference in exposure time has been observed for rectangular shaped features and round features, therefore it is recommended to determine the exposure time with the intended shape in mind (rectangular or circular). The optimal exposure times for Anycubic High Clear are as follows:

- **Hole:** No correct exposure time matches the intended size.
- **Pin:** Approximately 11 seconds brings the measured size closest to the intended size.
- **Bar:** 3 or 4 seconds can be used to match the intended size closest, with 3 seconds being a bit more accurate.
- **Groove:** 3 or 4 seconds can be used to match the intended size, with 4 seconds being a bit more accurate.

For the design of a microfluidic valve, the only feature type of interest is the groove. For other feature types, such as bars, pins, and holes, the design could be adjusted by scaling specific features to account for variations in exposure times if needed.

4.3.2. Liqcreate Elastomer-X

Observations on dye concentration

To enhance the visibility of the 3D printed membrane, a red dye is mixed into the resin. The printed samples containing 1, 2 and 3 wt% of red dye can be seen from Figure 4.11. Increasing the dye concentration leads to a more saturated red color. A change in mechanical properties and build plate adhesion is observed.

Figure 4.11: Comparison of 1, 2 and 3 wt% red dye respectively.

- **1 wt% red dye:** The addition of 1 wt% of red dye to Liqcreate Elastomer-X resin results in a slightly translucent sample with good adhesion to the build plate. The material's flexibility is maintained. This

concentration of red dye meets all demands for a suitable colored resin without sacrificing print quality or durability.

- **2 wt% red dye:** The sample with 2 wt% of red dye concentration presents a slightly more saturated red color, it is observed that translucency is not much reduced from the previous sample. It must be noted that print defects are in exactly the same region compared to the 1 wt% sample. This means that the print parameters do not have to be altered (there is no under- or overexposure due to the addition of a red dye).
- **3 wt% red dye:** At 3 wt% notable decreases in build plate adhesion and durability are observed. The sample did not stick to the build plate and broke when it was removed from the build plate, see Figure 4.12. This underlines the statements from Liqcreate and 3D Jake, and indicates potential issues with printability at higher dye concentrations. This brittleness is likely due to the increased dye concentration. This supports Liqcreate's and 3D Jake's statements that opaque pigments, which absorb or block UV light, can have a negative impact on printing stability and material properties. However, it must be noted that print defects are in exactly the same region compared to the 1 and 2 wt% samples. This means that also for 3 wt% the print parameters do not have to be altered.

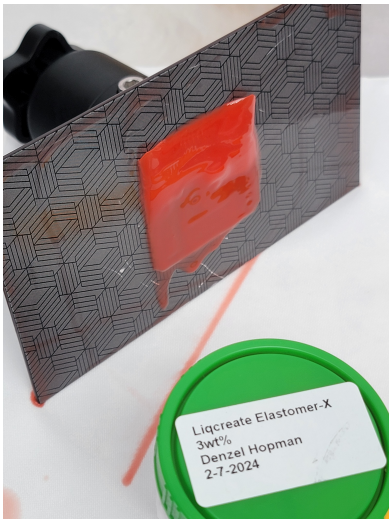

(a) The XP2 validation matrix containing 3wt% of red dye does not stick to the build plate using the recommended settings.

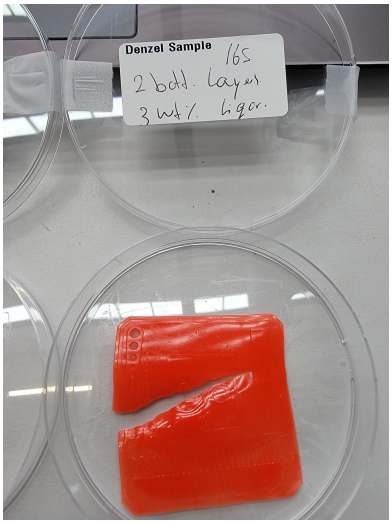

(b) The XP2 validation matrix broke directly when a small force was applied to remove it from the build plate, indicating brittleness and loss of material strength/elasticity.

Figure 4.12: Liqcreate Elastomer-X with 3 wt% red dye.

Observations on cleaning time of sample strips

After 3D printing, shiny spots can be observed on the features, these shiny spots represents dirty areas containing unpolymerized resin. From the pictures in Appendix C, it can be concluded that 25 to 30 minutes of ultrasonic cleaning has the best effect on removing these shiny parts (see Figure 4.13).

Figure 4.13: A cleaned sample using ultrasonic cleaning for 25 minutes.

Observations on swelling behavior in IPA

Multiple samples have been measured after 30 minutes in an ultrasonic IPA bath, it can be observed from Figure 4.14 that the samples grow from 2 cm to 2.5 cm in length. The results of ultrasonic cleaning these sample strips in IPA indicate that Liqcreate Elastomer-X samples tend to swell upon exposure to IPA. This swelling is likely due to IPA absorption, which temporarily increases the sample's dimensions.

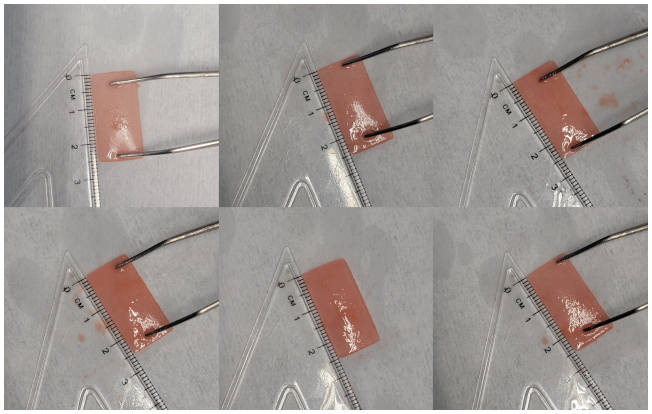

Figure 4.14: Measured sizes of 6 samples after a 30-minute ultrasonic IPA bath.

Observations on shrinkage at different temperatures

To further investigate the shrinkage behavior, the sample strip's length was recorded over a 4-hour period at both ambient temperature (27°C) and at an elevated temperature (50°C). Figure 4.15 illustrates the length of the sample over time, showing that samples return more quickly to their original dimensions at elevated temperatures compared to ambient conditions, the error is associated with the spacing between the lines of the ruler. This graph suggests that elevated temperatures accelerate the evaporation of absorbed IPA in Liqcreate Elastomer-X samples, which promotes faster dimensional recovery. However, this measurement method is not very accurate, but is nonetheless useful to show a clear difference in shrinkage between ambient temperature and elevated temperature.

The findings show that usage of IPA for cleaning Liqcreate Elastomer-X samples can cause temporary expansion, with dimensional recovery being highly dependent on temperature. For applications requiring precise dimensions, it is essential to allow the samples to revert back to their original size after IPA exposure.

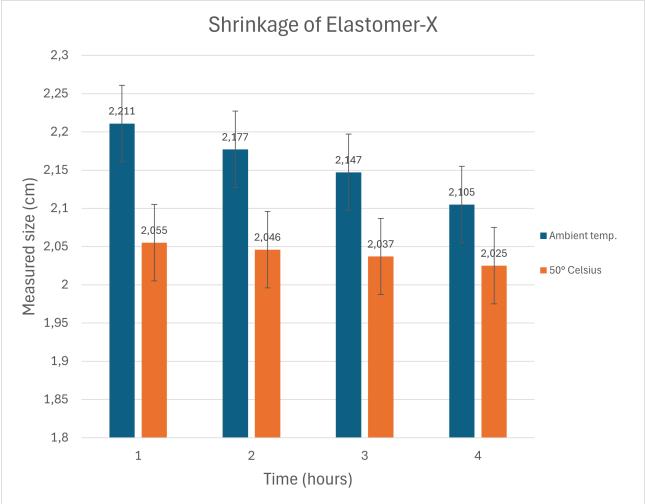

Figure 4.15: Shrinkage visualized with a graph of the measured size using ImageJ.

4.3.3. Tensile testing

Anycubic High Clear

The Anycubic High Clear dogbones are printed at exposure times of 5 and 10 seconds per layer, followed by washing in an ultrasonic IPA bath for 10 minutes. Subsequently, the samples are subjected to either 5 or 30 minutes of post curing in the UV curing device. The mechanical properties of these samples, specifically the average stress at break, ultimate tensile strength (UTS), and Young's modulus, were evaluated through tensile testing. An example of a single graph showing the maximum stress at break, the Young's modulus and the ultimate tensile strength can be seen from Figure 4.16.

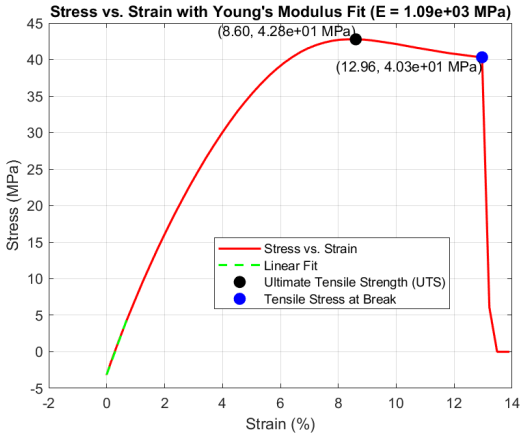

Figure 4.16: An example of a graph showing the fit of the Young's modulus, the maximum stress at break and the ultimate tensile strength.

The results of the combined (averaged) stress at break, ultimate tensile stress and Young's modulus are shown in Figure 4.17, the stress-strain data is accompanied by the standard error of the mean for each group. The following experimental groups are tested:

- **A:** Anyc. HC - 5 seconds exposure time, 5 min post curing
- **B:** Anyc. HC - 10 seconds exposure time, 5 min post curing
- **C:** Anyc. HC - 5 seconds exposure time, 30 min post curing
- **D:** Anyc. HC - 10 seconds exposure time, 30 min post curing

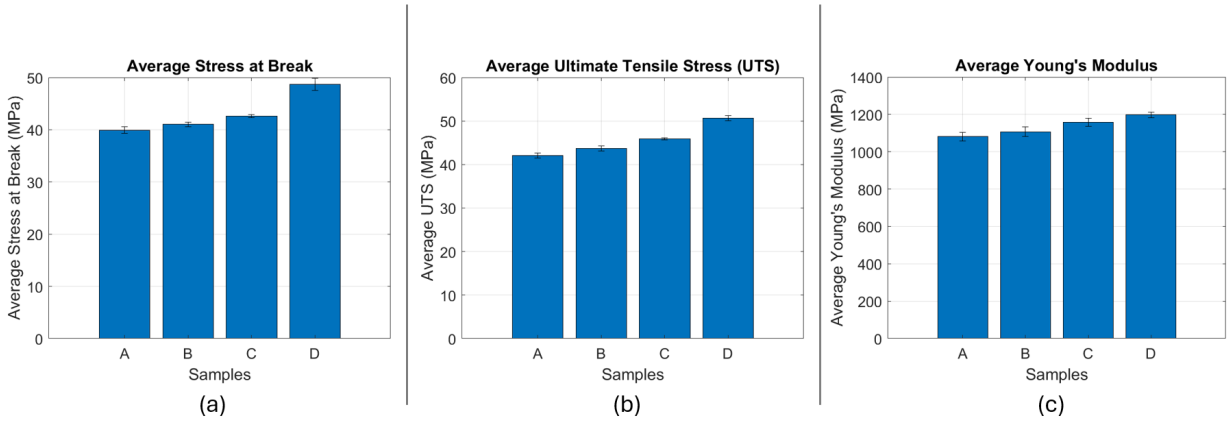

Figure 4.17: The average stress at break, UTS and Young's modulus accompanied by the standard error of the mean.

From the tensile testing results, it becomes evident that exposure time and post curing duration significantly influence the mechanical properties of 3D printed samples. The samples with a 5 second exposure time and 5-minute post curing time (Group A) exhibit lower mechanical properties compared to those printed with a 10 second exposure time (Group B). This is fully in line with expectations since longer exposure times generally lead to higher levels of curing and polymerization of the resin, improving the material's structural integrity.

The samples which are subject to 30 minutes of post curing time (Groups C and D) show an increase in the ultimate tensile strength (UTS), average stress at break and Young's modulus, suggesting that longer post curing times enhance the material's final stiffness and resistance to deformation. The increase in mechanical strength is likely due to the enhanced crosslinking (polymerizaton) achieved through longer post-curing.

Overall, the results suggest that both the exposure time and the post-curing time are crucial parameters that dictate the mechanical performance of Anycubic High Clear printed samples. The optimal mechanical properties, including the highest UTS, stress at break and Young's modulus, were achieved with the 10 second exposure time and 30 minutes of post curing time (Group D). During these tests, no brittleness due to over-curing was observed, from these 4 test groups, Group D shows optimal resin curing and thus mechanical performance.

Liqcreate Elastomer-X

For the Liqcreate Elastomer-X samples, both dyed and undyed samples are washed in an ultrasonic IPA bath for 30 minutes and heated at 50°C for 1 hour to recover the original dimensions. As per the manufacturer's (Liqcreate) guidelines, the samples underwent an initial curing step in demineralized water for 5 minutes. Subsequently, UV post-curing for different times (0, 30, and 60 minutes) is executed to assess the impact of post-curing duration on mechanical properties.

The mechanical properties of the samples are analyzed by evaluating their stress-strain behavior, as shown in Figure 4.18. The results clearly indicate that both post-curing duration and the addition of a red dye, do not play a significant role in enhancing or reducing the mechanical strength of the Liqcreate Elastomer-X material. Between 0 and 175% of strain, it is safe to conclude that the mechanical properties are not affected. Large deviations which are observed above 175% of strain may come from defects such as air bubbles or small indentations.

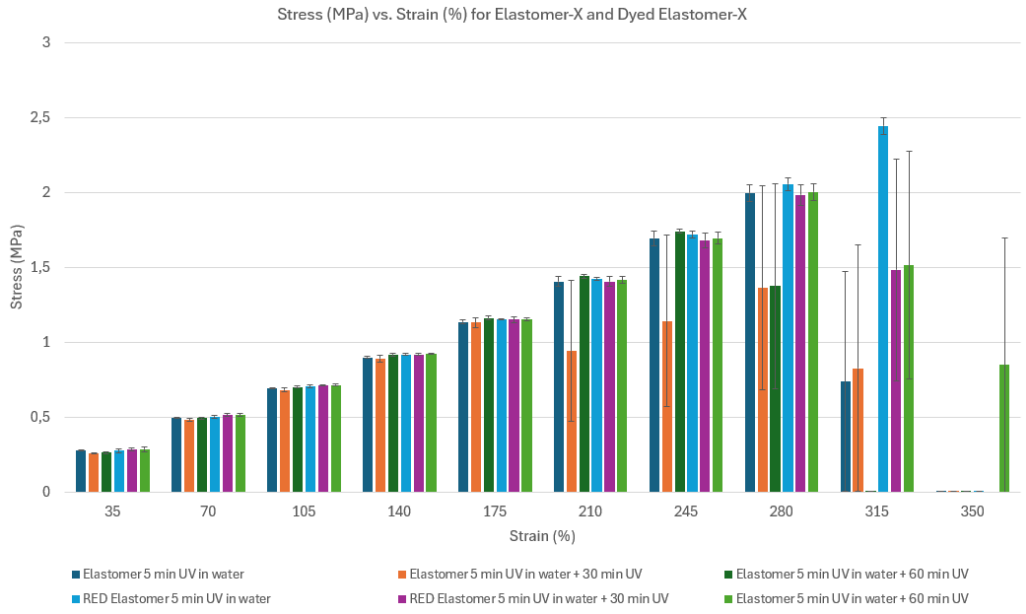

Figure 4.18: Stress vs strain for (dyed) Elastomer-X.

However, it must be noted that the base of the dogbone also adds to the elongation of the sample. This is due to the soft and elastic behavior of Liqcreate Elastomer-X, which makes it almost impossible to stretch the gauge length in an isolated manner.

4.4. Conclusion Print Process Optimization

This chapter has outlined the methodology to characterize resins, namely Anycubic High Clear and Liqcreate Elastomer-X with varying dye concentrations. The effects of exposure time on feature accuracy have been examined, as well as the influence of red dye additions on mechanical properties. The outcomes are relevant for the fabrication of multi-material microfluidic devices, particularly valves, where the soft material (Liqcreate Elastomer-X) will form the membrane, and the rigid material (Anycubic High Clear) will create the channels.

The primary objective of this chapter was to understand how the exposure time impacts the accuracy of 3D printed features using an affordable MSLA 3D printer (Elegoo Mars 4 9k). The Keyence VHX-6000 Digital Microscope has been used to systematically measure the feature size on the XP2 validation matrix, revealing that altering the exposure time significantly affects the accuracy and resolution of 3D printed features. For

Anycubic High Clear resin, exposure times of 3 to 4 seconds yielded optimal results for bars and grooves (rectangular sections), while pin sizes were most accurate at approximately 11 seconds. However, no optimal exposure time was found for the holes, which highlights challenges in achieving accurate void circular features.

In addition to exposure time, the effect of adding a red dye to Liqcreate Elastomer-X was investigated in this chapter. It was observed that small dye additions (1-2 wt%) have minimal impact on print quality and mechanical properties, making them suitable for customizing the appearance or optical properties of membranes without compromising performance. However, higher dye concentrations (3 wt%) reduce build plate adhesion and part durability, which could affect the reliability of the membranes in microfluidic valve applications.

Ultrasonic cleaning in IPA and dimensional stability were also investigated in this chapter. It was found that Liqcreate Elastomer-X samples are sufficiently clean after 25-30 minutes of ultrasonic cleaning in IPA . However, it was observed that these samples swell in IPA, to allow for dimensional recovery the samples can be put in a heated enclosure of 50°C for at least one hour. This observation suggests that a deeper understanding of cleaning processes is required to maintain dimensional accuracy across samples.

Tensile testing on the Zwick Roell Z005 highlighted the influence of exposure and post-curing times on the mechanical properties of Anycubic High Clear. The highest mechanical properties were achieved with a 10-second exposure time with 30 minutes of UV post-curing. For Liqcreate Elastomer-X, post-curing and dying of the resin had minimal impact on mechanical characteristics for strains between 0% and 175%, although some variability was observed at higher strains. The minimal impact of dye addition and post-curing on its mechanical behavior further supports its suitability for application in microfluidic valves as a membrane.

5

Finding the minimum channel size

This chapter discusses the stepwise approach to obtain the minimum groove size which an affordable MSLA 3D printer can produce. This minimum groove size will represent the minimum channel size which can be obtained and created in the rigid part of the valve. To do so, a resolution block has been designed using Solidworks, 3D printed in Anycubic High Clear and is lastly imaged using a digital microscope and measured using ImageJ.

5.1. Minimum channel size objectives

The objective of this chapter is to determine the minimum groove size which is achievable by an affordable MSLA 3D printer. The minimum groove size is assumed to be the minimum channel size, this leads to design properties which can be used to create flow and control channels in the rigid part (valve body) of the microfluidic valve. This process involves designing a resolution block in Solidworks, which is then 3D printed using Anycubic High Clear resin. The printed resolution block is subsequently analyzed using the Keyence VHX-6000 Digital Microscope to capture high-resolution images, which are further processed and measured using ImageJ software. The goal is to systematically assess the limitations of the 3D printing process in terms of channel width, and to identify the smallest functional features that can be reliably produced for microfluidic applications.

5.2. Materials and methods

This section discusses the design of a resolution block and the measurements which are executed to obtain a minimum groove width.

5.2.1. Design of a resolution block

A tool is designed in Solidworks to measure various groove widths, the design consists of a rectangular block with a total width and height measuring 24 mm and 25 mm respectively. The width of the wells (grooves) and extrusions on the resolution block features can be seen from Figure 5.1 and range from 10 µm to 200 µm in steps of 10 µm. Therefore, the minimum reproducible groove width in the desired orientation can be visualized. In this chapter, only the wells are investigated and discussed, extruded surfaces are not required for the fabrication of micro channels. The wells are oriented in vertical, horizontal and 2 diagonal directions with respect to the build plate. For simplicity, the first diagonal direction is called ”diagonal 1” and the second diagonal direction is called ”diagonal 2” in subsequent sections. The samples are printed using the settings from LycheeSlicer (see Figure 4.2) with an exposure time of 4 seconds which is based on the results from the previous chapter.

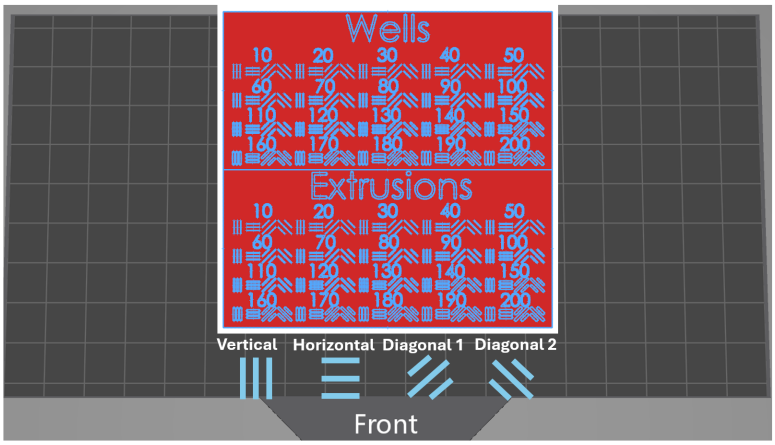

Figure 5.1: Resolution block.

5.2.2. Measuring the resolution block

A Keyence VHX-6000 Digital Microscope is used to take high-resolution pictures of the resolution block samples. These pictures are taken of 2 groove sizes at a time to reduce the number of pictures, an example of such a picture containing 2 groove sizes (150 and 200 µm) can be seen from Figure 5.2.

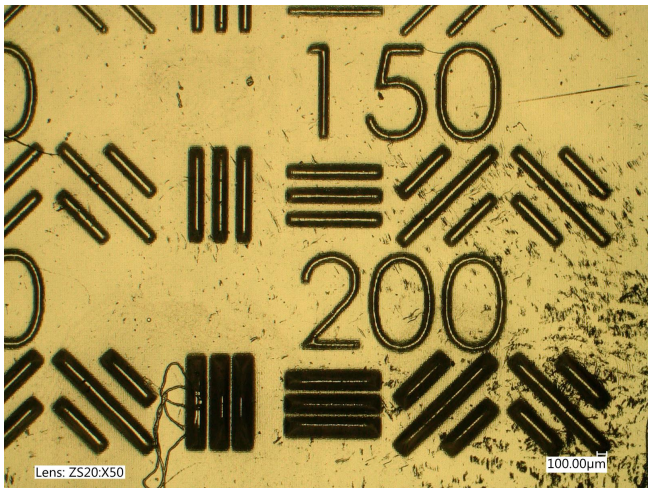

Figure 5.2: Picture taken with the Keyence microscope of grooves with a width of 150 and 200 µm. A scale bar is added for digital imaging.

These pictures are imported in ImageJ software, this software is used to measure the width of 3D printed grooves on the resolution block samples. The analysis involves selecting regions of interest, which are highlighted by yellow rectangles, these yellow rectangles and the fitted ellipses can be seen in Figure 5.3 and Figure 5.4.

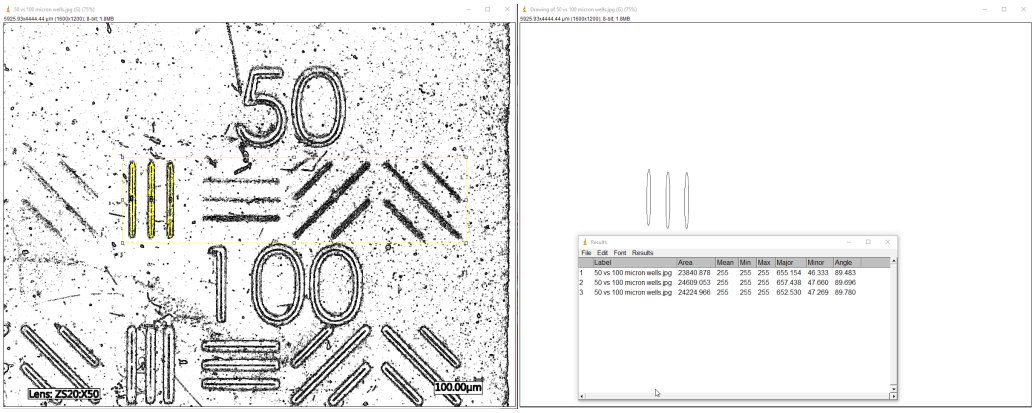

Figure 5.3: ImageJ analysis for a 50 µm groove width.

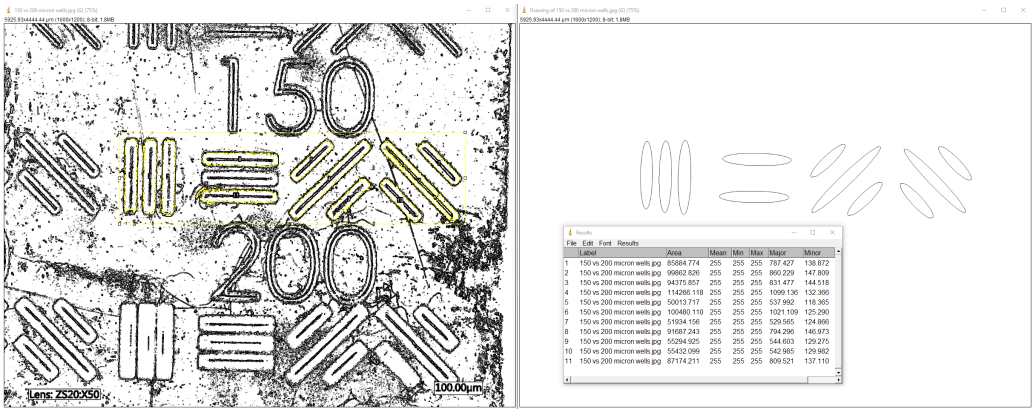

Figure 5.4: ImageJ analysis for a 150 µm groove width.

The ImageJ software tries to fit ellipses to all grooves within these selected regions. These ellipses consist of a minor and major axis, which relate to width and length. The ImageJ software calculates the groove width using the minor axis of the fitted ellipses. These measurements are conducted on grooves ranging from 10 to 200 µm, using three resolution block samples to minimize measurement errors. The resulting data was recorded in Excel for subsequent graphing and analysis. A summarized version of the workflow to accurately measure the width of grooves in 2D can be seen from Figure 5.5, the detailed explanation of this workflow can be found in Appendix A.3.

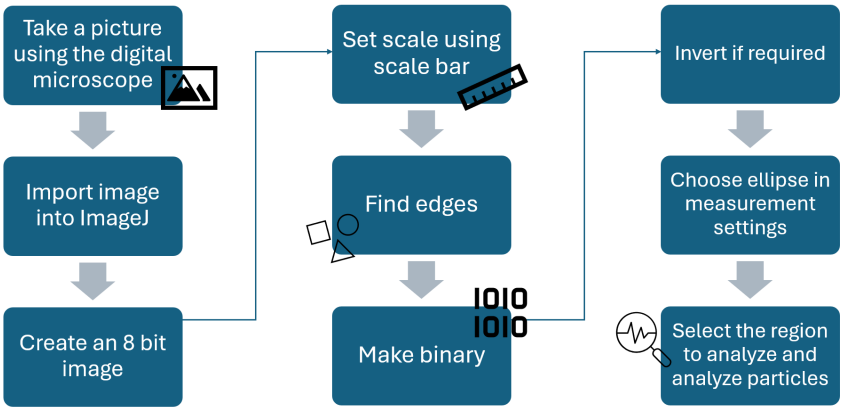

Figure 5.5: Workflow to obtain elliptical measurements from particles in ImageJ.

5.3. Results and discussion

5.3.1. Observations measurements

During these measurements, limitations of the ImageJ software were observed. For smaller groove widths, such as 50 µm, the software occasionally failed to fit ellipses accurately as can be seen from the right side of Figure 5.3. In some cases, the software did not display any fitted ellipses despite the region of interest encompassing all grooves. For larger groove widths, such as 150 µm, almost all ellipses can be fitted accurately as can be seen from Figure 5.4. The yellow rectangle or region of interest, results in the ellipses which are shown on the right.

5.3.2. Measured size vs intended size resolution blocks

The following graphs depict a comparison between the intended size and the measured size (in µm) of grooves on the designed resolution block, the data points are connected by the blue line. The red line represents the intended size, which would represent perfect accuracy. A trend closely following the red line indicates an overall consistency between intended and actual measurements.

Vertical

From Figure 5.6 it can be seen that the measured size deviates a lot from the intended size especially at smaller feature sizes and around 190 µm. These deviations at the higher range can be explained by the fact that the grooves are too close to each other on the resolution block, which the ImageJ software can not distinguish. Also, the LCD screen plays an important role with its organized pixels. It is hard to align the channels perfectly with the pixels on the LCD screen, perfect alignment is rarely guaranteed. As a result, aliasing may occur, where misalignment between the feature and the pixel grid causes distortions, such as inaccuracies in the intended geometry of the grooves.

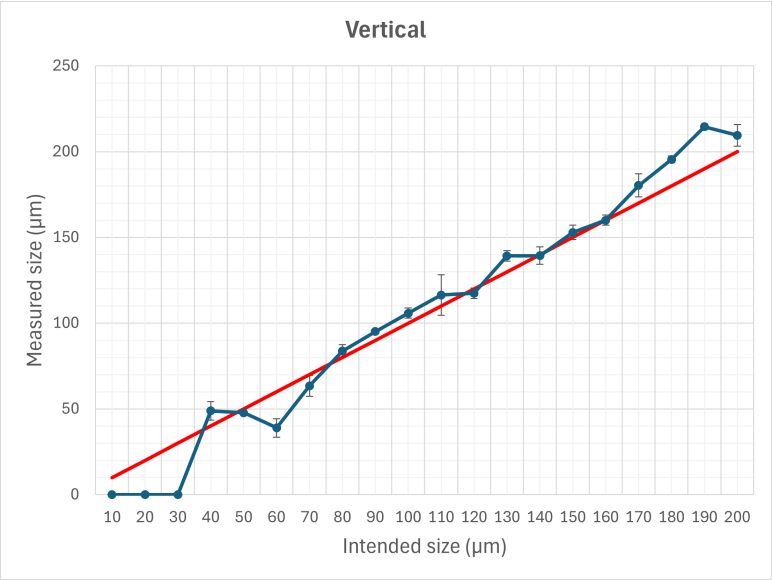

Figure 5.6: Measured size vs intended size for vertically oriented grooves.

Horizontal

The data shows that for mid-range sizes (approximately 120 to 170 µm), the printer performs reliably, with measurements aligning closely to intended values. The lower values have a larger standard error of the mean, therefore these measurements can not be trusted. In reality, they might be closer or further away from the intended size. In this case, a visual interpolation between 90 µm and 110 µm shows that the value at 100 µm is likely higher than depicted. The same goes for the value at 80 µm, which can be printed reliably using a vertical orientation. It is assumed that 80 µm could in theory work, since values closer to the red line have been found (standard error of the mean taken into account). Also, the pixel density of the LCD screen plays a huge role, alignment of these pixels with the channels is difficult as discussed previously for the vertical channels.

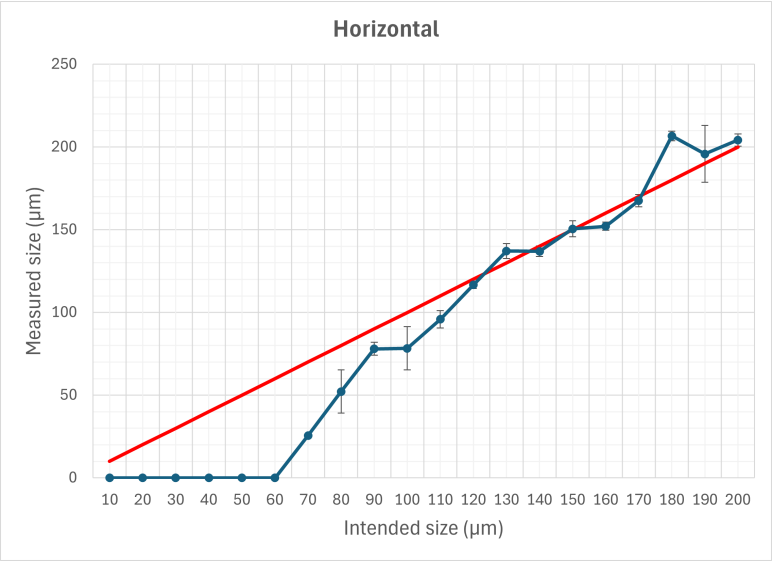

Figure 5.7: Measured size vs intended size for horizontally oriented grooves.

Diagonal 1

The results from the diagonal measurements of the resolution block demonstrate the MSLA 3D printer's capacity and limitations when printing features at a 45 degree angle. As shown in Figure 5.8, 90, 130, 170 and 190 µm wide channels can be accurately printed. All other channels deviate from the intended size with small error bars, this means that the measurements are likely acceptable and the problem lies elsewhere. One explanation might be the LCD screen, which has to perform aliasing to illuminate overlapping pixels. This might describe the fact that every step of 40 µm (almost 2 pixel sizes, 18 µm for Elegoo Mars 4 9K) from 90 µm results in a close resemblance of the intended size. The influence of aliasing reduces when the size increases, which can be seen from 190 µm.

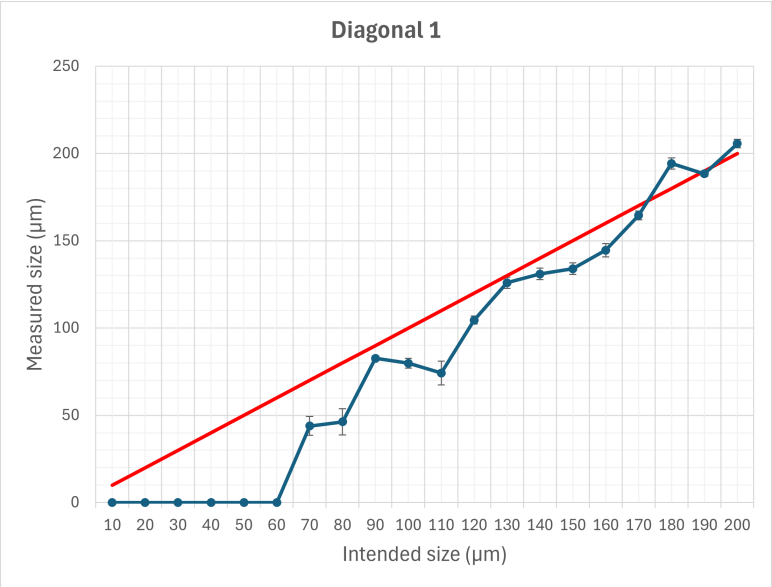

Figure 5.8: Measured size vs intended size for diagonally oriented grooves.

Diagonal 2

In Figure 5.9, the diagonal measurements for the second orientation of the resolution block reveal results similar to previous observations, it is observed that 120, 170, 190 and 200 µm replicate the intended size very well. Again, this is likely due to the interaction between the print angle and pixelation effects (aliasing). This data further emphasizes the importance of optimizing feature orientation when aiming for precise microstructures on MSLA 3D printers.

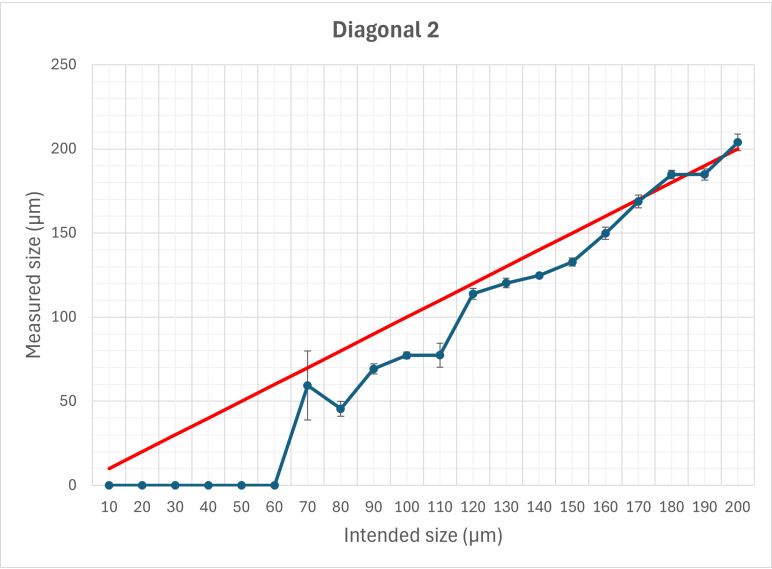

Figure 5.9: Measured size vs intended size for diagonally oriented grooves.

5.4. Conclusion minimum channel size

The primary objective of this chapter was to identify the minimum achievable groove width by following a structured approach. This methodology uses digital microscopy using a Keyence VHX-6000 Digital Microscope and imageJ image analysis software, revealing the deviations between the intended feature size and printed feature size. The resolution block design includes a variety of groove widths, ranging from 10 to 200 µm in steps of 10 µm, and is oriented in multiple directions to ensure the diagonal bias is visible in the results. It was observed that aliasing may have a larger influence on diagonal grooves, whereas horizontal and vertical grooves can be printed more accurately.

The results indicate that the used 3D printer can reliably produce grooves as small as 80 µm, with variations observed based on orientation and proximity of next to each other located large features. Some deviations at small scales could be attributed to limitations in the printer's resolution and the influence of pixel alignment on

the LCD screen. These results show the importance of considering both design aspects (channel orientation) and printer capability (resolution) in microfluidic applications.

6

Multi-material 3D printing

This chapter discusses the created protocol to enable for MMAM. The protocol involves several manual as well as software dependent steps. All aspects will be discussed and a conclusion will be drawn.

6.1. Multi-material objectives

The objective of this chapter is to create a novel 3D printing protocol which enables for multi-material 3D printing to aid in the creation of microfluidic devices using an affordable MSLA 3D printer. A multi-material microfluidic valve is chosen as a showcase for this protocol. First, the **research question:** *How do the 3D printing process parameters influence the mechanical properties of LCD 3D printed multi-material structures?* will be answered. The combination of the newly created protocol and the results regarding the mechanical properties will answer the following **research question:** *Which 3D printing protocol can be used to develop a high-resolution multi-material microfluidic structure?* and the **main question** of this research: *How to develop a novel 3D printing protocol which enables for the fabrication of a high resolution multi-material microfluidic device in a single step fabrication process?*

6.2. Materials and methods

This section discusses the adaptation and refinement of the existing print-pause-print protocol.

6.2.1. Print-pause-print

The used protocol is based on the existing Print-Pause-Print protocol, see Figure 6.1. This protocol can be carried out utilizing a single affordable MSLA 3D printer and multiple resin vats. The first step is to print with material A, the printer is then paused through a software called UVTools, all aspects of this software will be explained in Section 6.2.2. After this pause step, the build plate has to be cleaned which is the most challenging part. A thorough explanation of this cleaning step is provided in Section 6.2.3. When the part is fully clean, the resin vats can be switched and the printing can be resumed with material B. This protocol can be iterated without upper limit on executions and materials.

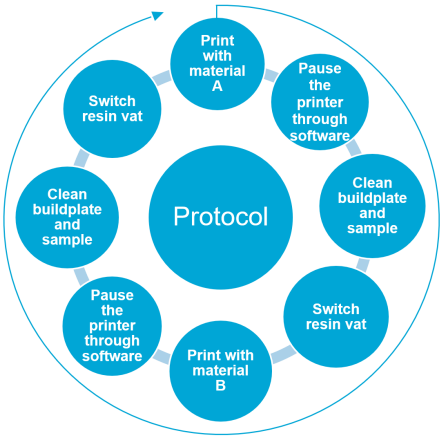

Figure 6.1: Protocol for print-pause-print.

6.2.2. Software

To enable for switching of the material during multi-material 3D printing, while using the print-pause-print protocol, a unique software called UVTools is used. This computer program enables for a pause step and custom slicing (exposure time, layer thickness etc.) which can be used by the MSLA 3D printer. To import a file into UVTools, a presliced .goo file is required in which the right printer is chosen. This .goo file is obtained by slicing an STL file in Chitubox. However, other slicer softwares are equally capable at this task.

To create a multi-material structure, consisting of 3 layers (a valve), it is required to have 2 pause steps. The first pause step will be directly after the first part which is made out of Anycubic High Clear, to enable for such a pause step several settings are required. In UVTools a setting called ”Timelapse” can be found from the ”Tools” menu. Timelapse was initially created to raise the build plate after each layer to take pictures of the process (a timelapse video consists of these images). This setting can be used to enable for 1 pause step per layer. There are four variables which are of particular interest. The first is the layer range selector (number 1 in Figure 6.2). When only 1 layer is required to pause, both input boxes should contain the same number. The height of the build plate also has to be specified (number 2 in Figure 6.2), in this case the maximum height of the Elegoo Mars 4 9K is automatically entered when the ”Max” button is pressed. It also needs to be specified wether it is required to raise per amount of layers (number 3 in Figure 6.2). When 0.0 is entered, the software accepts that only 1 lift is required. Lastly, the wait time for the pause step is entered (number 4 in Figure 6.2). Any arbitrary number between 0 and 1000 seconds can be chosen, as an example 600 seconds has been chosen. Care must be taken to provide enough time to pause the printer using the pause button on the printer itself, allowing for enough time to clean the build plate.

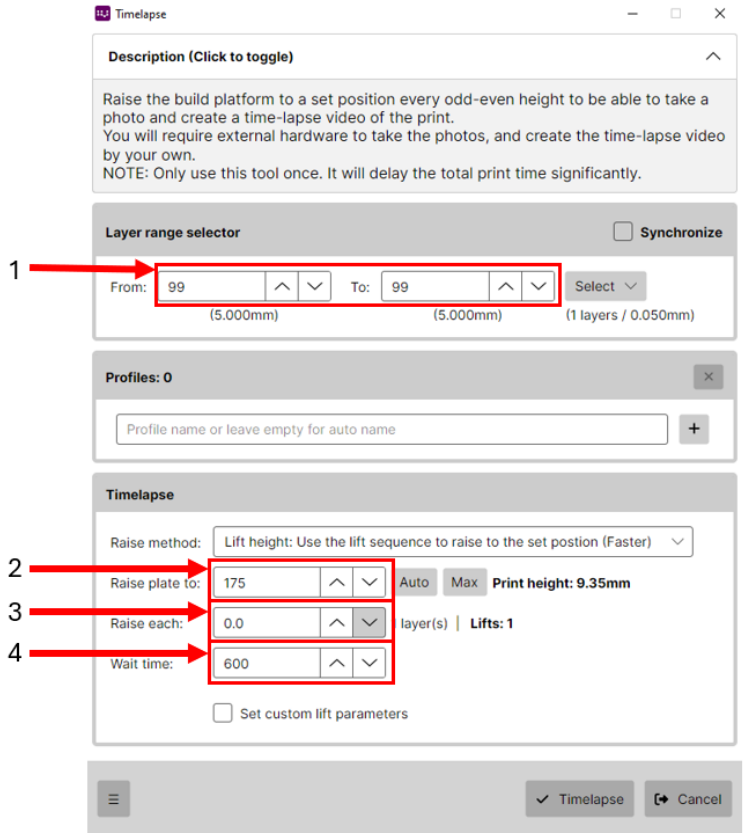

Figure 6.2: Step 1: Set the required layer range to create the timelapse on. Step 2: Raise the build plate to the required height, in this case maximum (Max) was chosen. Step 3: Only 1 lift is required per pause step, choose 0.0. Step 4: The wait time can be chosen, in this case 5 minutes was chosen.

The next important setting from the ”Tools” menu is the ”Phased exposure”. Using this setting, the exposure time can be altered for a selected range of layers. From Figure 6.3, it can be seen from number 1 that the range is set from 30 to 60, a total of 31 layers will be affected by this altered exposure time. The layers which will be altered for the creation of a microvalve are at the middle section of the valve, therefore the bottom exposure does not have to be altered (only applicable to the first layers of Anycubic High Clear). From number 2 in Figure 6.3, it can be seen that only the normal exposure time has to be altered. The printing time will increase substantially when the exposure time is increased, the software ”adds” or duplicates layers with the added exposure time. For example, when the exposure time is increased from 10 to 16 seconds, a 10 seconds original layer and a 6 second additional layer are created without raising the build plate between those layers.

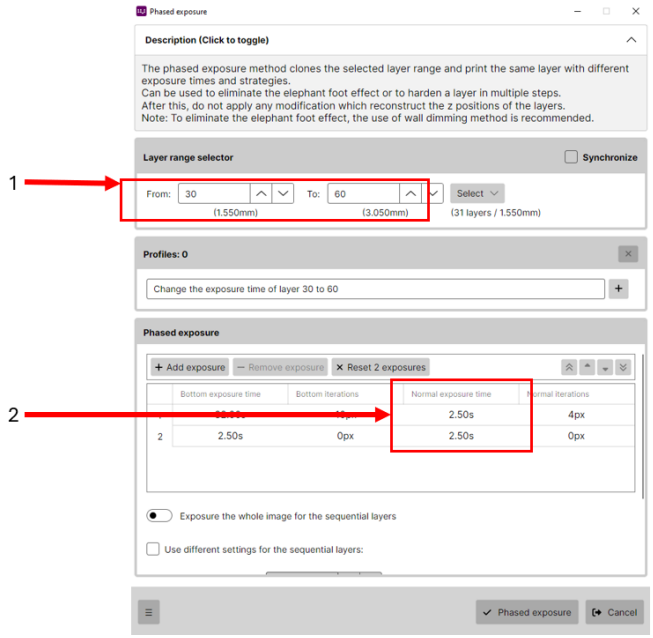

Figure 6.3: Phased exposure is used to alter the exposure time for a selected range of layers.

It is known from Liqcreate (by contacting them directly) that Liqcreate Elastomer-X does not print well at layer heights less than 0.05 mm or 50 µm due to the soft nature of the material, therefore 50 µm is chosen as the layer height for this material. However, Anycubic High Clear prints perfectly fine on 0.01 mm or 10 µm. Therefore, another setting is required to alter the layer height during printing, it is required to change the layer height for layers associated with Liqcreate Elastomer-X from 10 µm to 50 µm as described, this can be realized with the ”Edit print parameters” setting from the ”Tools” menu. When the ”Change settings per a layer range” box is ticked, settings can be altered per layer. For example, from Figure 6.4 it can be seen that Z-position is at 1.550 mm, this layer can be edited to 1.510 mm to obtain a 10 µm increase at layer 30, instead of 50 µm. It must be noted, that subsequent layers must be altered manually, the software does not calculate the Z-position of the remaining layers automatically. Another note for this setting is the exposure time, this can also be manually altered using ”Edit print parameters” setting instead of the ”Phased exposure” setting.

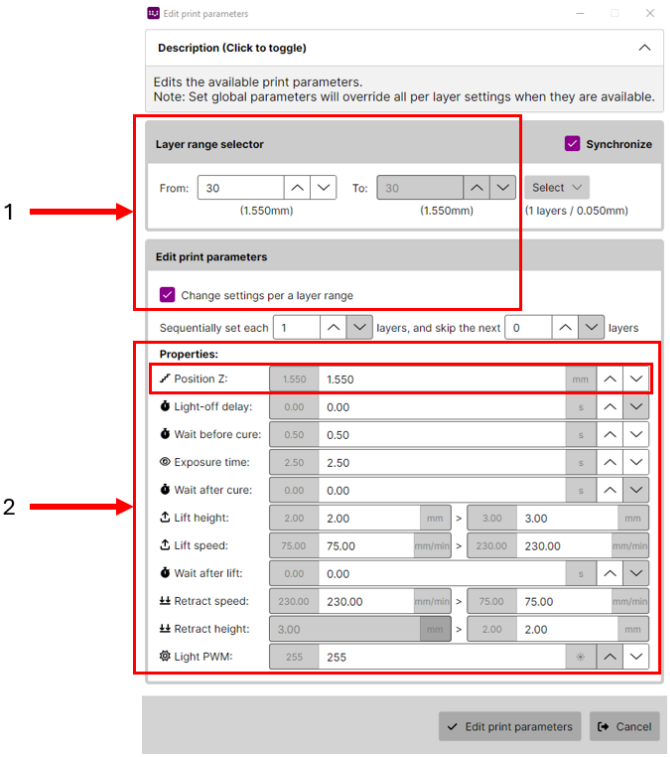

Figure 6.4: The edit function is used to manually alter the layer height per layer.

The edited layer height has been tested on a small sample, this sample is a unit cube with dimensions of 1x1x1 mm, it is designed in Solidworks. The layer height for several separate layers is altered from 0.01 mm to 0.05 mm, which creates a total length of 1.8 mm in the UVTools software. The total size of the unit cube after editing of the layer height is 1x1x1.8 mm, an increase in height of 0.8 mm with respect to the original size should be observed. After printing the sample, it's length is measured with digital calipers to validate the expected size, which is 1.8 mm in this direction. Using the calipers, the found value is 1.7 mm, which is significantly higher than 1 mm, it can be concluded from this test that manually altering the layer height is a valid method. The measurement using the digital caliper can be seen from Figure 6.5. Note that these cheap digital calipers are not accurate, nonetheless a large difference between the expected size of 1.8 mm and original size of 1 mm is observed.

Figure 6.5: Calipers were used to validate if the printed object has the correct dimension, as edited in the UVTools software.

6.2.3. Cleaning and MMAM

The first step to enable for MMAM is to create a cleaning stand, which can be used to clean the build plate and the partially printed sample during the pause step of the printer. Ultrasonic cleaning will be performed using a Nanografi Ultrasonic Processor. The cleaning stand is created using a custom frame, several parts are designed in Solidworks and 3D printed on an FDM printer (Bambulab X1C) using PETG filament. The frame itself is created out of 2020 and 2040 aluminum profiles, which are often used to create stands and devices or machines. This makes it easy to attach other pieces onto the frame using T-nuts and M5 bolts. The designed parts consist of 2 brackets which attach to the 2020 profiles, the Nanografi Ultrasonic Processor and the IPA bath are mounted to these brackets. The complete stand accompanied by its 3D printed attributes can be seen from Figure 6.6.

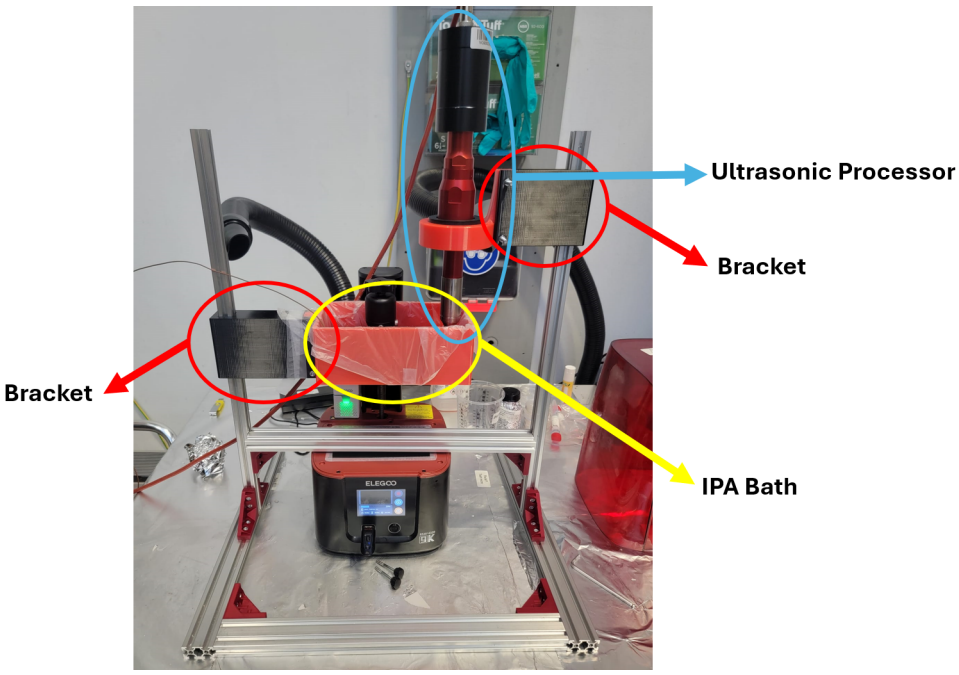

Figure 6.6: The cleaning stand is created out of 2020 and 2040 aluminum profiles and consists of an IPA bath, a holder for the Nanografi Ultrasonic Processor and brackets to connect these attributes to the frame.

The attributes consist of an IPA bath, a holder for the Nanografi Ultrasonic Processor, and brackets to mount the IPA bath and holder. Pictures of the CAD files which are used to create this cleaning stand can be seen from Figure 6.7.

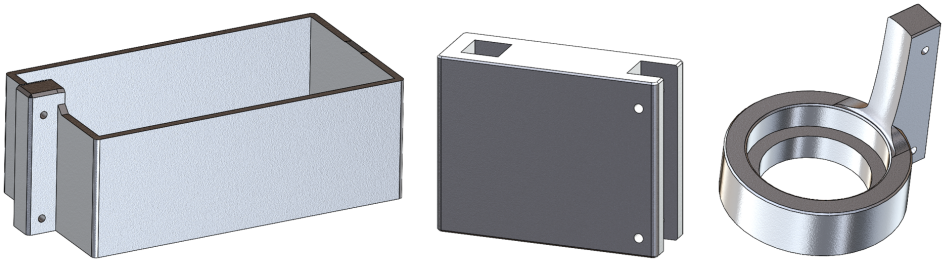

Figure 6.7: Attributes for the cleaning stand, with (a) the IPA bath, (b) the bracket and (c) the holder for the Nanografi Ultrasonic Processor.

First, initial testing of the developed cleaning stand is required, the first cleaning was executed on a multi-material test sample. The samples of choice are multi-material dogbones, which are required to evaluate the bonding strength between both materials. These dogbones were shortened to eliminate long printing times, otherwise the print could not be finished in one day. This shortened dog bone is created in Solidworks using the original dog bone as base design. The gauge length of this modified shorter dogbone is 15 mm. However, it must be noted that this dogbone will be printed in both materials, Anycubic High Clear and Liqcreate Elastomer-X, it is assumed that the Elastomer-X will provide the most elasticity, therefore the effective gauge length is assumed to be 7.5 mm (0.5*15 mm). The design of this shortened dog bone can be seen from Figure 6.8.

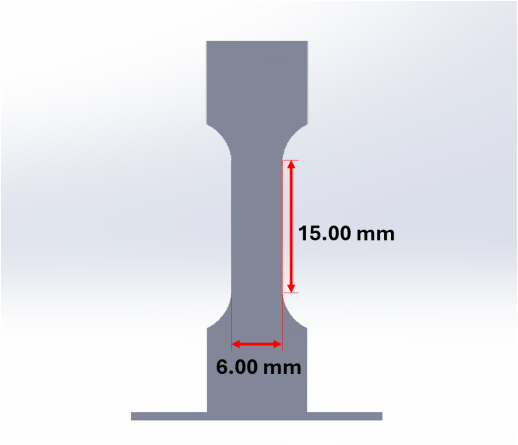

Figure 6.8: The dogbone is shortened to reduce printing time, in order to be able to pause the printer in time.

The shortened dog bones are saved in Solidworks as an STL file, this STL file is sliced in Chitubox using the exposure settings for Anycubic High Clear and the retraction settings for Liqcreate Elastomer-X, these retraction settings are chosen because Liqcreate is a more viscous liquid, therefore these retraction settings are viable for both materials. This file is saved and imported into UVTools. During this test, both layer heights are kept at 50 µm due to ease of programming. The pause step is enabled at layer 453 in UVTools, which is exactly at the middle of this shortened dog bone. This pause step is set to a Z height of 175 mm (max. height of the print bed) and a wait time of 1000 seconds, which is the maximum pause time and equals around 16 minutes and 40 seconds. The file is saved to a USB drive and the usb drive is inserted into the 3D printer.

The sliced file is selected on the 3D printer and the first 452 layers are printed in Anycubic High clear. The second vat with material B (Liqcreate Elastomer-X) can be prepared before or during printing with material A (Anycubic High Clear). It is advised to cover the second vat to avoid UV exposure or dust particle contamination.

When the printer is done with layer 452, it will pause on layer 453 and raise the build plate to a Z height of 175 mm. The 16 minutes and 40 seconds of pause time starts immediately. It is advised to press the pause button manually during these 16 minutes and 40 seconds to elongate the pause time, it is of strong importance to stay in proximity of the 3D printer to press this button in time.

When the printer pauses, the build plate is covered in material A (Anycubic High Clear). To prevent dripping of resin directly onto the LCD screen, aluminum foil is used to cover the build plate with the partially printed sample attached. The resin vat can be safely removed when everything is covered correctly. Cleanroom paper is placed on top of the LCD screen to prevent damage or scratches.

The cleaning stand is placed around the 3D printer, the IPA bath is on its lowest position and the homogenizer is placed in the holder. When everything is in place, the aluminum foil is removed from the build plate and the IPA bath is raised to the desired level and filled with IPA until the build plate is fully submerged in IPA.

The homogenizer can be turned on when no leakage is observed, in this example a cleaning time of 15 minutes at 10% of power is used. During ultrasonic cleaning, it is observed that cavitation occurs locally around the homogenizer tip. Besides this observation, the temperature (19 degrees Celsius) of the IPA in the bath is monitored to prevent IPA from evaporating too quickly.

Figure 6.9: Temperature of IPA bath during ultrasonic cleaning is observed to be 19 degrees Celsius

After the cleaning time is elapsed, the homogenizer is turned off and the IPA bath is lowered to its lowest

point. The IPA which is still on the build plate will evaporate over time. Compressed nitrogen or air can be used to speed this process up. The result of the ultrasonic cleaning can be seen from Figure 6.10. When the build plate is sufficiently dry and no wet spots are observed, the stand can be removed from the 3D printer.

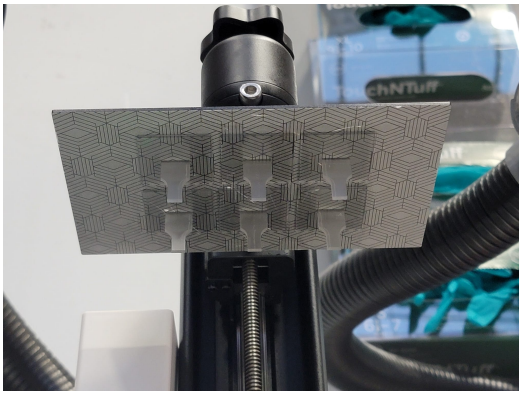

Figure 6.10: The partially printed dog bones are cleaned using ultrasonic cleaning.

The cleanroom paper is removed from the LCD screen and the new vat consisting of material B (Liqcreate Elastomer-X) is placed on top of the LCD and screwed firmly in place. The red UV cover is placed back on the 3D printer and the printing is resumed using the resume button on the 3D printer's touch screen.

When the print is complete, it can be cleaned like a normal single material 3D printed object using the steps described in Appendix A.1.

To assess layer bonding between both materials, the dog bones are tensile tested in the same way as described in Chapter 4 and their ultimate tensile stress (UTS) is compared to the UTS of single material 3D printed dog bones using Liqcreate Elastomer-X. The results of this comparison can be seen from the graph in Subsection 6.3.2.

6.2.4. Protocol for MMAM microvalves

This protocol outlines and summarises the previous steps involved in the multi-material 3D printing process, from preparing the model to post-processing the 3D printed part. The intermediate (between 2 materials) cleaning step can be found in Appendix A.2 and will be referenced throughout this thesis to keep the protocols short and to the point. Also listed are the used equipment, used chemicals, associated dangers and the protective gear which is advised to perform these tasks.

Step 1

Cleaning solution

1. Create a frame
2. Design attributes to hold vat and homogenizer
3. Waterproof the IPA bath by using a plastic bag
4. Attach the attributes to the frame

Step 2

Software and model preparation

1. Prepare STL file in slicer
2. Import the file in UVTools
3. Export the file to a USB drive

Step 3

Printing material A

1. Insert USB drive in 3D printer
2. Select the model and start the print
3. Prepare resin vat with material B and cover the vat

Step 4

Pause and cleaning

1. Follow the protocol as described in Appendix A.2.

Step 5

Printing material B

1. Resume the printer
2. Clean and post cure the part as described in Appendix A.1

Equipment

- MSLA 3D printer
- 2 resin vats
- Resin vat cover
- Nanografi ultrasonic processor / Homogenizer
- 3D printing Resin
- Aluminum foil
- Cleanroom paper
- Plastic bag
- Isopropanol (IPA)

Chemicals

- Anycubic High Clear
- Liqcreate Elastomer-X
- Isopropanol (IPA)

Dangers

- Dripping resin onto LCD screen.
- Dripping IPA which can drip into the printer.

Protective gear

- Protective glasses
- Gloves

6.3. Results and discussion

6.3.1. Multi-material 3D printing interface observations

After printing with both materials, it was observed that the protocol resulted in successful multi-material 3D printed objects, in this case dogbones were printed. The 3D printed dogbones were printed in Anycubic High Clear and Liqcreate Elastomer-X. The results of multi-material 3D printing on an affordable 3D printer can be seen in Figure 6.11.

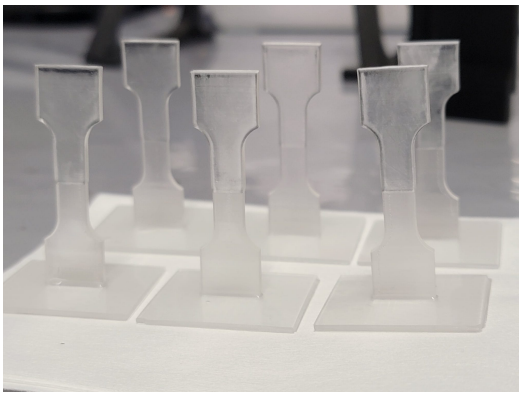

Figure 6.11: MMAM dog bones, created in Anycubic High Clear and undyed Liqcreate Elastomer-X.

These clear samples were used to evaluate the bonding strength, this evaluation can be found in the next subsection (Subsection 6.3.2). To visualize the bonding between both materials, dyed dogbones have been created, showing a distinct variation in color (clear and red). These samples can be seen from Figure 6.12.

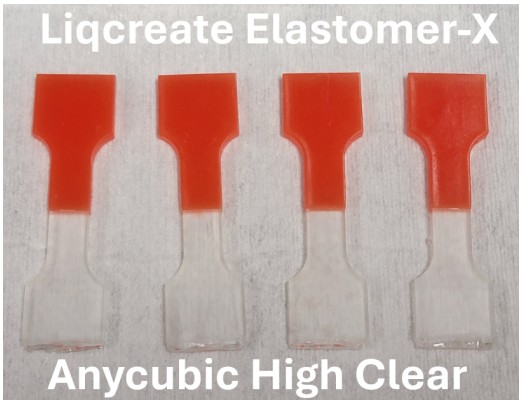

Figure 6.12: MMAM dog bones, created in Anycubic High Clear and dyed Liqcreate Elastomer-X.

A closeup of the bond between both materials can be seen from Figure 6.13. The sharp interface indicates a well-aligned printing and cleaning process, with no visible misalignment or delamination.

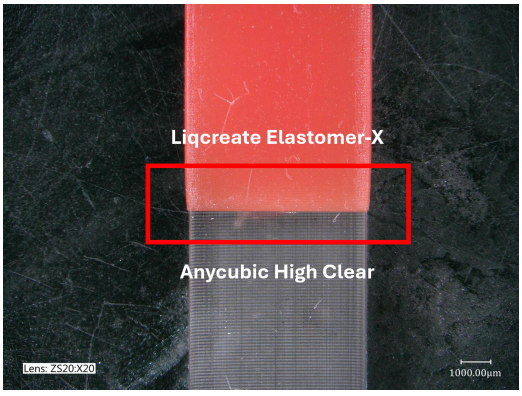

Figure 6.13: Material interface on a multi-material dogbone.

6.3.2. Results for multi-material tensile testing

To verify the performance of the interface (bonding strength) between Liqcreate Elastomer-X and Anycubic High Clear, tensile testing is performed and the average UTS is compared to the average UTS of single-material Liqcreate Elastomer-X dogbones. Using Matlab, the average UTS of all single-material Liqcreate samples (dyed and undyed) is found to be 2.28 MPa. The same Matlab script (Appendix B.6) has been used to calculate the average UTS of all multi-material dogbones, of which the average UTS is 2.43 MPa.

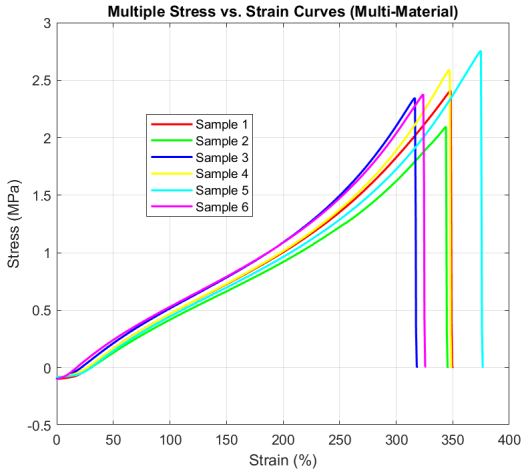

Figure 6.14: Six multi-material samples have been tensile tested.

It is remarkable that the multi-material dogbones show a higher UTS than its single-material counterpart. This can be explained by several factors. The interface strength may have gotten even higher than with the single-material Liqcreate Elastomer-X samples due to covalent bonding, the composite interface may therefore not experience the same localized failure such as delamination that a single material might. It can be seen from Figure 6.15 that failure does not occur exactly at the interface, indicating a strong covalent bonding. This strong and rigid interface could allow the stress to be distributed more evenly over the area of the dogbone, enhancing its UTS.

Figure 6.15: Broken tensile testing samples, it can be seen that failure does not occur across the (entire) interface. It is observed that a small piece of Elastomer-X stays attached to the Anycubic High Clear, indicating a good bonding strength.

6.4. Conclusion multi-material 3D printing

In this chapter, a novel protocol for multi-material additive manufacturing (MMAM) is successfully created and implemented using the print-pause-print method as foundation to fabricate microfluidic devices. The focus in this chapter lies on the fabrication of multi-material dogbones and the bonding strength between both materials.

Key to this process is the ability to pause the 3D printer while printing, and effectively and efficiently clean the build plate and attached part. It was discovered that the printer can be paused manually during the pause step provided by UVTools. This provides enough time to clean the part, which ensures a clean multi-material interface.

It was shown that the interface between both materials had no defects and was consistent across the entire width. This sharp interface indicates that no visible misalignment or delamination occurs while printing multi-material objects, however this is only applicable to the used materials.

The experimental results show that the multi-material interface enhances the ultimate tensile strength (UTS) compared to single-material Liqcreate Elastomer-X dogbones with an observed average UTS of 2.43 MPa, surpassing the 2.28 MPa of single-material Liqcreate Elastomer-X dogbones. This improvement can be attributed

to the robust interface bonding that potentially creates an even stress distribution across the multi-material interface.

These findings underscore the viability of the multi-material protocol and creates high hopes for the fabrication of more complex structures such as multi-material microfluidic valves which will be discussed in the next chapter.

7

Multi-material microvalve

This chapter discusses the simulation and validation of membrane deflection under pressure. As well as the CAD design of a multi-material microfluidic valve which could be created through multi-material additive manufacturing (MMAM). Finite Element Method (FEM) simulations using Solidworks are employed to predict the valve's behavior, allowing for precise analysis of the performance of the valve for various membrane diameters. To ensure accuracy, these simulations are validated using an established analytical approach from relevant literature, providing a robust assessment of the valve's functionality. Lastly, a protocol is proposed and validated on a simplified valve-like sample without the membrane and channels, consisting of 2 material interfaces.

7.1. Valve objectives

The primary objective is to show that a valve can be created, which complies with certain performance requirements. FEM simulations are used to predict the valve's mechanical performance for various membrane diameters, enabling an in-depth understanding of its operational behavior. The second objective of this chapter is to validate the accuracy of FEM results by comparing them against an established theoretical formula from relevant literature. The third objective is to create a robust design in Solidworks, which serves as a foundation for the MMAM microfluidic valve. The last objective is the creation of a protocol which allows for the fabrication of this designed and simulated microfluidic valve. This protocol is validated by showcasing the fabrication of a valve-like sample. These objectives combined will provide a robust design and fabrication strategy for 3D printed multi-material microfluidic valves.

7.2. Materials and methods

7.2.1. CAD Design

The design of this microfluidic valve is based on the Quake valve, which is a type of valve which is open at rest. This active valve requires air pressure in the control channel to close the flow channel. The design consists of 2 orthogonal channels lying on top of each other, these channels are separated by a thin elastomer membrane. Several dimensions and their justification will be provided in this paragraph. The dimensions of interest are the:

- **Channel width:** The width of the channel is already provided in Chapter 5.3, therefore 80 µm wide channels will be used for the final design of the microfluidic valve.
- **Channel height:** The height of the channel is dependent on the flow rate, the optimization of the channel's flow rate is out of scope for this study. Therefore, any arbitrary height can be chosen, in this case an aspect ratio of 1:1 is chosen which makes the channel square.
- **Membrane diameter:** The membrane diameter can be chosen arbitrarily, allowing for flexibility in the design to meet specific requirements for deformation, pressure response, or integration within the overall device dimensions. A membrane diameter of 1 to 3 mm is chosen for this exemplary simulation and design.
- **Membrane thickness** The membrane thickness is chosen to be one or two layer heights of Liqcreate Elastomer-X, which equals 50 µm and 100 µm respectively.

It must be noted that for an optimized microfluidic device, several requirements have to be made beforehand. This ensures that the performance of the device is linked to its design elements. However, optimization of flow and measurements on leakage rates etc. are out of scope for this research.

An example of a multi-material microfluidic valve has been designed in Solidworks. This exemplary design can be seen from Figure 7.1, the design consists of 2 materials and 3 sections. The first section is created using Anycubic High Clear and contains the flow channel. The second section is the thin membrane, which is created out of Liqcreate Elastomer-X. Lastly, another section is created out of Anycubic High Clear, which consists of a control channel and Luerlock connectors. This way, syringes can be applied as a pressure source.

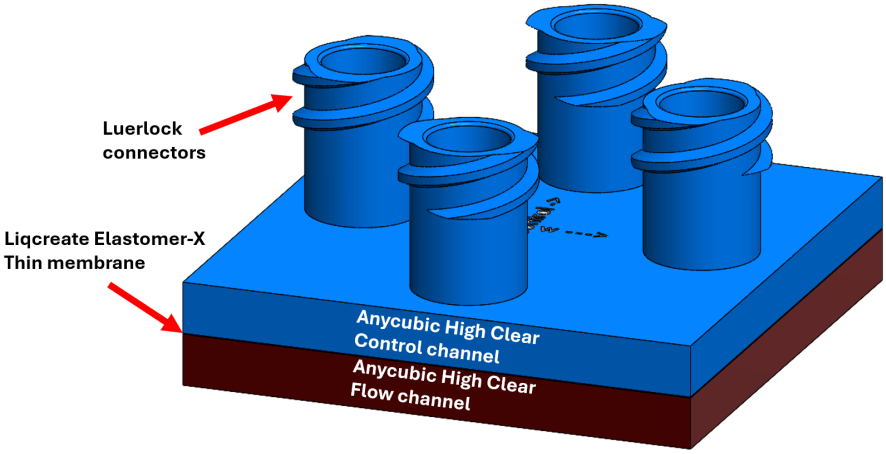

Figure 7.1: An assembled microfluidic valve; consisting of a rigid part with 4 Luerlocks (blue), a thin flexible membrane in the middle and a rigid base (red).

The separate sections can be seen from Figure 7.2, it can be seen that the flow channel consists of a seat for the membrane. The seat is designed to have a diameter of 3 mm. The top section and the thin membrane are shown in (b) and (c) respectively.

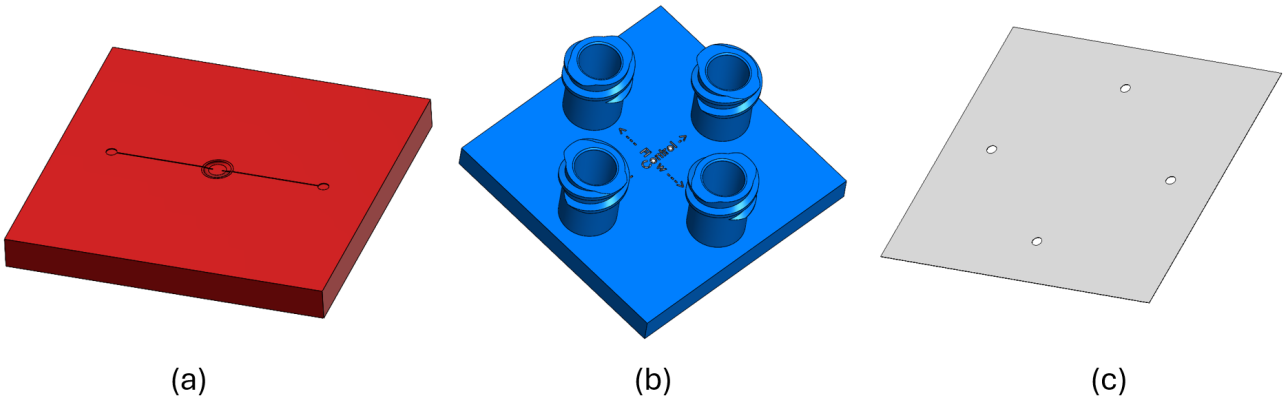

Figure 7.2: An overview of parts to create the valve. (a) The base consisting of a flow channel and a seat for the membrane, (b) the top of the valve consisting of the control channel and Luerlocks to attach a pressure source, and (c) the thin and flexible membrane.

This design is exemplary and will not be created during this research. However, to prove that this design can be manufactured, a simplified 3-section design without the membrane, channels and Luerlocks will be created as a showcase.

7.2.2. FEM simulation

Simulation of the flexible membrane

Elastomeric and rubber-like materials, such as Liqcreate Elastomer-X, typically demonstrate isotropic and elastic behavior without any permanent set (like plasticity). Besides, they demonstrate a nonlinear stress-strain behavior, therefore Hooke's law is usually not applicable. A full non-linear model would describe this behavior best, but would require a lot of computational resources. Another option is to use the first portion of the graph, this portion of the curve often leads to the estimated Young's modulus as can be seen from Figure 7.3. However, this method is only applicable to low strain levels before non-linearities occur.

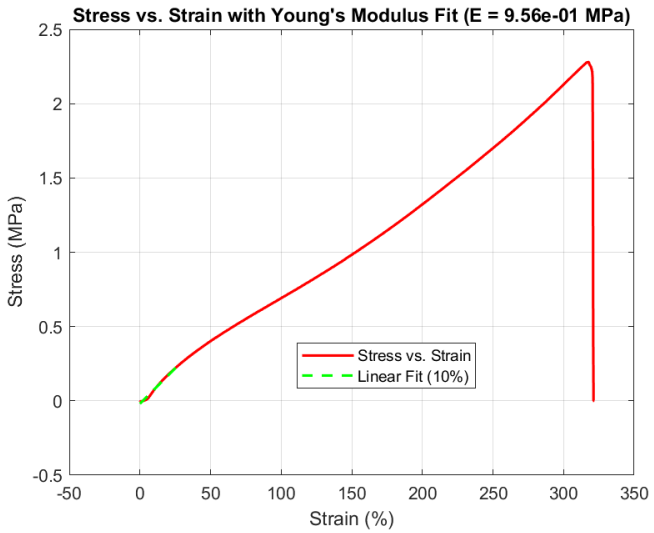

Figure 7.3: An example of the approximation of the Young's modulus of Liqcreate Elastomer-X using a 10% linear fit in Matlab.

It is observed that a linear fit across the entire graph resembles the stress-strain curve quite well. The same Matlab code with small adjustments can be used to increase the reach of the linear fit. The result of this method can be seen from Figure 7.4. The average Young's modulus is calculated for all Elastomer-X samples and is found to be 0.693 MPa, this is calculated using the Matlab code which can be found in Appendix B.7. The output of this matlab code can be seen from Figure 7.3.

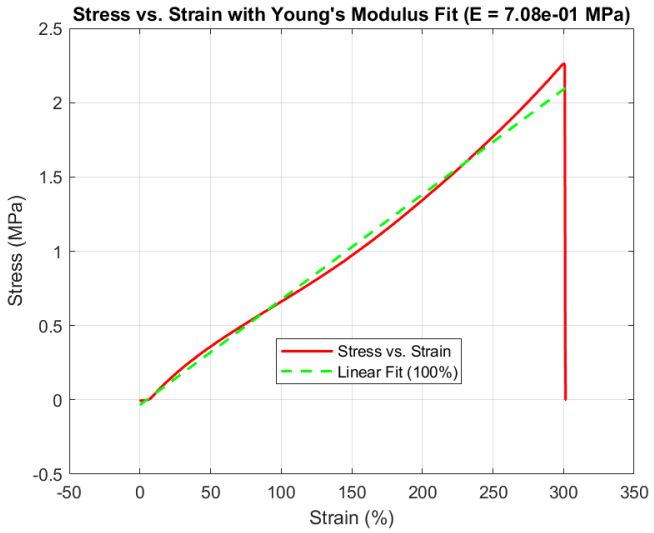

Figure 7.4: An example of the approximation of the Young's modulus of Liqcreacte Elastomer-X using a 100% linear fit in Matlab.

To use this linear fit, the coefficient of determination, R^2, has to be provided to make a good estimate of the correctness of this fit. A value close to 1 indicates that a large proportion of the variance is explained by the model, meaning a better fit. Values close to 0 indicate a poor fit. The R^2 for each linear fit can be found in Table 7.1.

Sample	1	2	3	4	5	6	7	8	9
R^2	0.95223	0.95572	0.95708	0.95378	0.91630	0.95631	0.95858	0.94992	0.95517

10	11	12	13	14	15	16	17	18	Avg.
0.95960	0.95285	0.94827	0.95604	0.95120	0.95211	0.94529	0.96513	0.95875	0.95246

Table 7.1: The R^2 for each linear fit, performed on graphs of tensile tested Liqcreate Elastomer-X.

Based on the found R^2 values for the linear fits on Liqcreate Elastomer-X tensile test graphs, the results consistently show high correlation values. The average R^2 value of 0.95246 further confirms the strong linear relationship in the dataset. This indicates that a linear model using 100% of data points, provides an excellent fit for the tensile test data across all samples.

In conclusion, a 100% linear fit describes the data very well with an average R^2 of 0.95246. This fit represents the entire strain range, whereas a 10% linear fit is limited to a very small strain region. Therefore, it is chosen to perform the FEM simulations with data (average Young's modulus) from the 100% linear fits, because this option allows for a larger stress range to simulate while representing a large portion of the curve. This average Young's modulus is found to be 0.693 MPa.

Second, the Poisson ratio must be known, the Poisson ratio can be estimated to be close to the value of 0.5 [127], in this case 0.495 is chosen, because a Poisson ratio of exactly 0.5 corresponds to an incompressible material. This can sometimes lead to issues with the finite element solver, to avoid these issues a slightly lower value of 0.495 is used to approximate near-incompressibility while maintaining numerical stability. Third, the average ultimate tensile strength (UTS) must be known, this value is found using a Matlab code which averages the highest values from each tensile test, this code can be found in Appendix B.6. This value is found to be 2.43 MPa and is entered in the "Tensile strength" field of the custom material in Solidworks. Lastly, the density of the material has to be considered, this density is provided by Liqcreate and is equal to 1180 kg/m^3. A picture summarizing these values can be seen from Appendix D.

The membrane can be simulated while it's integrated in the valve or isolated from the valve. The first option is to simulate the entire valve with an integrated membrane. The main benefit of this method is that the pressure for full wall contact of the membrane is correctly simulated. However, this requires more computational cost and can not be validated manually. The second option is to design an isolated membrane on which a pressure can be applied, this membrane deformation can be validated using a theoretical approach. Full wall contact can be realized by modeling a negative of the deformed membrane's shape as the valve seat. This ensures proper wall contact during operation for a certain pressure. Therefore, due to ease of operations, the second method is chosen for these FEM simulations. Trial and error is used to match the deformation of the membrane's center to the channel depth (80 µm) to ensure full sealing of the channel. The mesh is left unchanged, the standard setting for Solidworks simulations has been used and an example of the mesh can be seen from Figure 7.5, which shows the mesh for a membrane with a diameter of 2 mm and a thickness of 50 µm. Membranes with a diameter of 1, 2 and 3 mm are simulated using the described method.

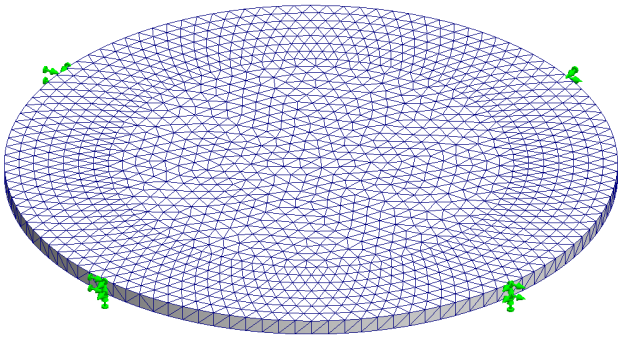

Figure 7.5: The mesh for a membrane with a diameter of 2 mm and a thickness of 50 µm.

Workflow

The stepwise workflow to create FEM simulations for thin membranes is described in this paragraph, the list of steps can be seen from the list below.

1. Design a circular membrane in Solidworks, using dimensions which are either provided or required. In this case, combinations of thicknesses of 50 and 100 µm, and diameters of 1, 2 and 3 mm are used.
2. Add a material to the membrane in Solidworks, go to "Edit material" and create a custom material. In this case, the custom material was named "Liqcreate Elastomer-X".
3. The material properties can be entered, a Young's modulus of 0.693, Poisson ratio of 0.495 and density of 1180 kg/m^3 are entered in the table, as well as the Tensile strength of approx. 2.4 MPa.
4. The Solidworks simulation manager requires several settings before a simulation can be executed. First, the type of simulation has to be chosen, in this case non-linear was chosen. Second, the fixtures or constraints have to be chosen. The membrane is connected to the valve at its edges, therefore these

edges (or outer face) can be chosen as constraints. Third, a uniform pressure of arbitrary magnitude must be applied.

5. A mesh has to be created, the default settings are used to mesh the model.
6. Run the simulation, the results can be seen from the ”Results” tab.

7.2.3. Validation

The validation is performed using the formula provided in Figure 7.6. This formula relates the applied pressure to the membrane deflection at the center of a thin circular membrane. The outcome of this analytical validation serves as a comparison to the computational FEM model.

$$\frac{Pr^4}{Et^4} = \frac{5.33}{1-v^2} \cdot \frac{y}{t} + \frac{2.6}{1-v^2} \cdot \left(\frac{y}{t}\right)^3$$

Figure 7.6: This equation describes the relationship between applied pressure P (MPa) and membrane deflection y (mm) at the center of a thin circular membrane. This membrane has a thickness t (mm), a radius r (mm), and is made of a material with a Young’s modulus E (MPa) and Poisson’s ratio v [12].

This formula can be written as the pressure P in terms of the membrane deflection y. The value of y is determined by the valve’s requirements and is therefore a known value. The pressure P will be compared to the by trial-and-error found pressures from the FEM simulations. This formula is used in Matlab to generate graphs, the code can be found from Appendix B.8.

7.2.4. Protocol MMAM microfluidic devices

The following protocol which can be used to 3D print multi-material microfluidic valves is based on the protocol which can be found in Subsection 6.2.4. Several adjustments are made to accommodate for 2 pause steps and a change in layer height during printing.

Step 1

Software and model preparation

1. Create the valve design in CAD software, in this case Solidworks is used.
2. Prepare the STL file in the slicer software, use the settings for Liqcreate Elastomer-X to slice the file with the exposure settings from Anycubic High Clear. This way only the exposure time for the soft intermediate part has to be changed in the following steps.
3. Check the amount of layers and the height in the slicer, compare this to the CAD model and identify which layers need alteration.
4. Import the file in UVTools and use the ”Timelapse” setting to create 2 pause steps. One pause-step is required between the interface from rigid to soft material and one pause-step is required between the interface from soft to rigid material.
5. Since the file is sliced with the exposure time for Anycubic High Clear, it is only required to change the exposure time for the intermediate part. Select the ”Phased exposure” option and select a layer range to set the ”Normal exposure time” to 16 seconds.
6. Be aware that a pause step at ”layer 5” pauses the printer after finishing layer 4. The ”Phased exposure” setting affects the layers by adding a duplicate layer with a certain amount of exposure time, when for example ”from: layer 100 to: layer 105” is selected, 12 (2*6 layers) frames are created in UVTools, this does **not** affect the total height.
7. The last setting which is required is ”Edit print parameters”, in which manual adjustments to the layer height can be made. Creating larger layer heights, result in a larger model (Z-height). This has to be compensated for in the CAD design. For example, if the file is sliced at 10 µm and the membrane is supposed to be one layer of 50 µm, this layer should be designed in CAD to be 10 µm. In the UVTools settings this single layer is altered to be 50 µm.

8. UVTools does not automatically calculate the Z height of the subsequent layers. For example, when a single layer is edited from 45.050 mm to 45.100 mm and the file is sliced at 10 µm, the next layer after a Z height of 45.100 mm will start at the ”following” layer height, which is 45.060 mm. All subsequent layers have to be edited manually to overcome this problem.
9. Check the file, layer per layer, using the navigation menu to check the correctness of all values. If all values are correct, save the file.
10. Export the file to a USB drive and insert it in the 3D printer. Select the file and start the print, during printing the vat containing material B can be prepared. Make sure to cover the vat.

Step 2

Pause and cleaning

1. Follow the protocol as described in Appendix A.2.

Step 3

Printing material B

1. Resume the printer

Step 4

Pause and cleaning

1. Follow the protocol as described in Appendix A.2.

Step 5

Printing material A

1. Resume the printer
2. Clean and post cure the part as described in Appendix A.1

Equipment

- MSLA 3D printer
- 2 resin vats
- Resin vat cover
- Nanografi ultrasonic processor / Homogenizer
- 3D printing Resin
- Aluminum foil
- Cleanroom paper
- Plastic bag
- Isopropanol (IPA)

Chemicals

- Anycubic High Clear

- Liqcreate Elastomer-X
- Isopropanol (IPA)

Dangers

- Dripping resin onto LCD screen.
- Dripping IPA which can drip into the printer.

Protective gear

- Protective glasses
- Gloves

7.3. Results and discussion

7.3.1. FEM simulation

The average Young's modulus of all Elastomer-X samples, which is the result of the described method in Subsection 7.2.2, was found to be 0.693 MPa. The pressures which are required to deflect the center of various membrane diameters for 80 µm, and their accompanying Von Mises stress are found using trial-and-error and are given in the list below. An example picture of these FEM simulations can be seen from Figure 7.7, all pictures of the FEM simulations containing both displacement and stress can be found in Appendix D.

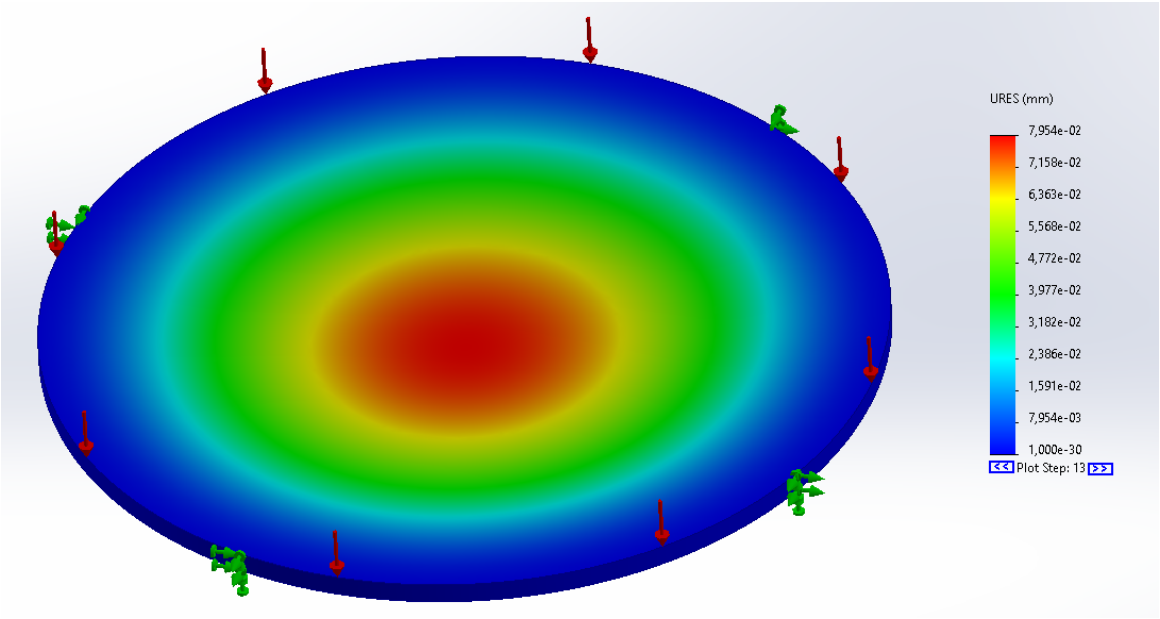

Figure 7.7: FEM simulation using Solidworks for a 2 mm diameter membrane with a thickness of 50 µm. The color bar displays the deviation of the membrane's center in mm.

- For a membrane with a diameter of 1 mm and a thickness of 50 µm, the actuation pressure required is 1660 Pa to close the valve. The stress value for this pressure is 7.523×10^4 Pa.
- For a membrane with a diameter of 1 mm and a thickness of 100 µm, the actuation pressure required is 5860 Pa to close the valve. The stress value for this pressure is 9.166×10^4 Pa.
- For a membrane with a diameter of 2 mm and a thickness of 50 µm, the actuation pressure required is 120.0 Pa to close the valve. The stress value for this pressure is 2.328×10^4 Pa.
- For a membrane with a diameter of 2 mm and a thickness of 100 µm, the actuation pressure required is 505.0 Pa to close the valve. The stress value for this pressure is 2.998×10^4 Pa.
- For a membrane with a diameter of 3 mm and a thickness of 50 µm, the actuation pressure required is 25.90 Pa to close the valve. The stress value for this pressure is 9.532×10^3 Pa.
- For a membrane with a diameter of 3 mm and a thickness of 100 µm, the actuation pressure required is 105 Pa to close the valve. The stress value for this pressure is 1.297×10^4 Pa.

The average UTS of Liqcreate Elastomer-X samples is 2.43 MPa, it is observed that all stress values are far below this value. Therefore, the prediction is that the membrane will not break during operation with these pressures.

7.3.2. Validation

Using the explained method, graphs have been created using Matlab which show the pressure in terms of deflection. The deflection is known from the design requirements and this results in several actuation pressures for 1, 2 and 3 mm diameter membranes.

Pressure values for a 50 µm thick membrane can be seen from Figure 7.8 and are listed below for a deflection of 80 µm:

- **1 mm diameter** - 1750.97 Pa (1660 Pa from FEM)

- **2 mm diameter** - 109.436 Pa (120.0 Pa from FEM)
- **3 mm diameter** - 21.6169 Pa (25.90 Pa from FEM)

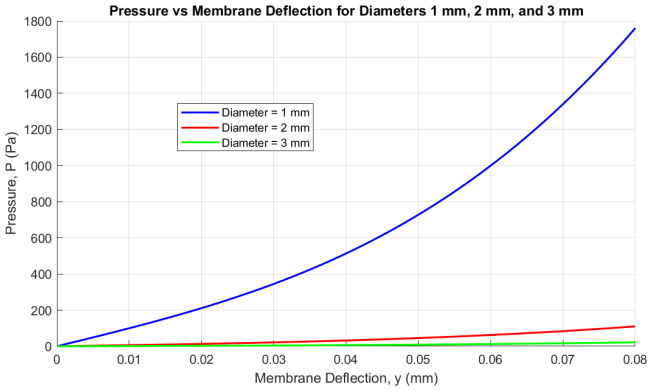

Figure 7.8: Graph showing the analytical approach to calculate the 50 µm thick membrane's deflection at the center.

Pressure values for a 100 µm thick membrane can be seen from Figure 7.9 and are listed below for a deflection of 80 µm:

- **1 mm diameter** - 8186.85 Pa (5860 Pa from FEM)
- **2 mm diameter** - 511.678 Pa (505 Pa from FEM)
- **3 mm diameter** - 101.072 Pa (105 Pa from FEM)

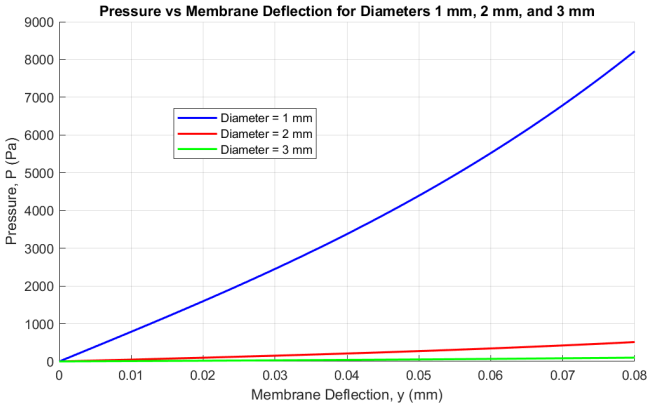

Figure 7.9: Graph showing the analytical approach to calculate the 100 µm thick membrane's deflection at the center.

It can be seen that these values are very close to the values found using the FEM analysis. The biggest discrepancy is found at a diameter of 1 mm with a thickness of 100 µm. This result may implicate that the used formula is only applicable to thin membranes in which the radius is a lot larger than the thickness (r»t). However, this result is in the same order of magnitude as the FEM simulated value. Since all other values found from FEM simulations are very close to the analytically found values, this analytical approach is a good validation of the FEM model. This means that the selected simulation model (non-linear) in Solidworks is sufficiently accurate to model thin flexible membranes. However, several remarks can be made about this method. First, this result would probably be more accurate with a full non-linear model of the Liqcreate Elastomer-X material. Second, a sensitivity analysis of the mesh should be made. Due to time constraints, no sensitivity analysis has been performed. Third, this simplified model does not account for the dead volume in channel, and because no wall contact was modeled, no conclusions can be drawn on the leakage of the valve. In conclusion, a microfluidic membrane can be simulated accurately using FEM simulations in combination with an analytical validation.

7.3.3. MMAM two material interfaces structure

The creation of a simplified valve-like structure consists of 3 sections and two material interfaces, it is fabricated without the membrane and channels. Fabrication of this structure proves the reliability and functionality of the

discussed newly developed protocol. This simple design can be expanded to functional microfluidic valves and other devices by simply adding channels and membranes in the design. The current design consists of a rectangular block of 25x25x2 mm, in which a 1 mm thick dyed (1 wt%) Liqcreate Elastomer-X ”membrane” was printed between both sections of Anycubic High Clear. Due to time limitations, the layer height was set to 0.05 mm or 50 µm for both materials. A pause step was initiated at layer 10 and at layer 30, the exposure time was set to 16 seconds for layer 10 to layer 30. The result of this method, utilizing the developed protocol, can be seen from Figure 7.10. The figure illustrates the interfaces between the three sections of a multi-material structure using Anycubic High Clear and dyed Liqcreate Elastomer-X. Notably, the first section (the left side, attached to the build plate) of Anycubic High Clear has a reduced height compared to the upper section (right side) of Anycubic High Clear. The reduced height of the bottom part can be explained by resin compression by the build platform, this occurs because the printer presses the build platform against the resin vat. For applications such as multi-material microfluidic devices, where precise layer thicknesses are critical, especially in components like flexible membranes or rigid channels, accurate layer control is essential for maintaining performance and functionality. However, the lost height can be added in the CAD design, therefore this loss in height can be mitigated by compensation in the design.

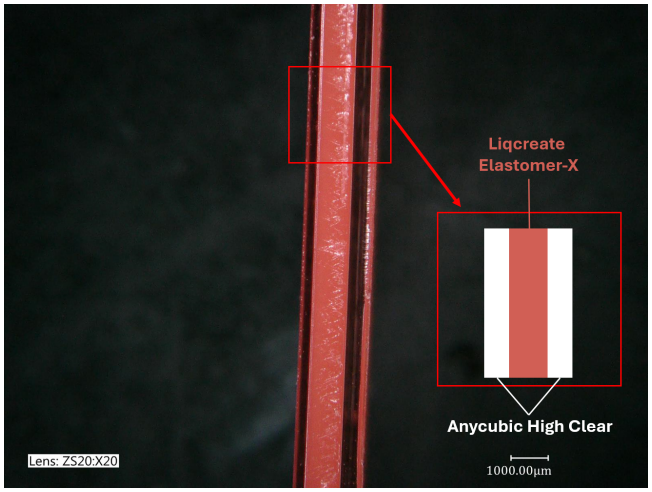

Figure 7.10: Material interfaces between sections in a multi-material dual-interface structure.

7.4. Conclusion multi-material microvalve

This chapter provided an examination of the design, simulation, and validation of a multi-material microfluidic valve using multi-material additive manufacturing (MMAM). The primary objective was to develop a protocol to fabricate multi-material microfluidic devices. This protocol considers aspects such as model preparation and software settings to the actual printing and cleaning processes. The protocol consists of 2 pause steps and numerous settings in the UVTools software to accommodate for the change in layer height and exposure time, while ensuring that the pause steps enable for cleaning in between layers.

The membrane’s performance was simulated in Solidworks using FEM, these simulations were validated against a relevant analytical method. The FEM results obtained in Solidworks have shown that membranes with 1, 2 and 3 mm diameters will not break due to pressures required to close a membrane. The membranes were simulated to deflect 80 µm and several pressures have been found to close the valve. These pressures have been validated using an analytical approach to calculate membrane deflection under a given pressure. It was found that the pressures are very similar, except for the 1 mm diameter membrane with a thickness of 100 µm, implicating that this analytical approach might only be applicable to very thin membranes in which the radius is a lot larger than the thickness. A mesh sensitivity analysis could improve the results as well, which was not performed due to time constraints.

The microfluidic valve design is based on the Quake valve, which consists of dual orthogonal channels separated by a thin membrane. By choosing channel dimensions based on prior characterization, and exploring a range of membrane sizes, the design aims to meet specific functional requirements while allowing for manufacturability within the constraints of MMAM. However, due to time constraints a fully functional microfluidic valve was not created during this research. Instead, the protocol was validated on a three-segment valve-like structure, which has proven the protocol’s reliability and usability.

8

Conclusion & Future work

8.1. Conclusion

This thesis has successfully demonstrated the potential of using multi-material additive manufacturing (MMAM) to create high-resolution, functional microfluidic devices, specifically focusing on microfluidic valves. However, the actual creation of a functional microfluidic valve was beyond the scope of this research. The research has outlined a novel protocol utilizing the print-pause-print technique, which has been shown to enable for the fabrication of multi-material microfluidic devices utilizing a single step fabrication process.

To create a multi-material microfluidic valve, it is required to have a flexible membrane and a rigid part containing the channels, therefore a rigid material and a flexible material were evaluated. The rigid material was used to create features, which can be distinguished as pins (extruded circles), bars (extruded rectangles), grooves (void rectangles) and holes (void circles), these features have been used to optimize the printing process. It was found that altering the exposure time can significantly affect the accuracy and resolution of 3D printed features. Exposure times of 3 to 4 seconds yielded optimal results for bars and grooves (rectangular sections), while pin sizes were most accurately reproduced at approximately 11 seconds. However, no optimal exposure time was found for the holes, which highlighted challenges in achieving accurate void circular features and calls for mitigation by using a scaling factor which is unique per feature shape.

The soft and flexible membrane material was printed with various dye concentrations to enable for visualization of the membrane during operation of the valve. It was observed that smaller dye concentrations of 1 and 2 wt% minimally impacted print quality, whereas a higher concentration of 3 wt% negatively affected build plate adhesion and durability. Therefore, 1 wt% was chosen as the minimal invasive dye percentage for subsequent testing. Ultrasonic cleaning in IPA of these soft samples caused swelling, which was shown to be reversed by heating the samples at 50°C for at least one hour. Subsequently, both undyed and dyed soft material, as well as the rigid material, were used to create dogbones for tensile testing. It was observed that the rigid material showed the highest mechanical properties at 10 seconds exposure time per layer and 30 minutes of UV post-curing, whereas the mechanical properties of the (dyed) soft and flexible material was largely unaffected up to a strain of 175%.

After the mechanical properties of both materials were known, the minimum feature size to create channels in the rigid material was evaluated by creating grooves as small as 10 µm, it was found that 80 µm could be printed reliably in the vertical direction. Variations were observed due to feature orientation, proximity of close to each other features, and printer resolution limits which are influenced by LCD pixel size and alignment.

As the mechanical properties of the two materials were already known, an expansion of the research to multi-material additive manufacturing was made by creating a novel protocol. For the fabrication of multi-material microfluidic devices, the bonding strength between both materials is of key importance, therefore multi-material dogbones were created and tensile tested. To fabricate multi-material dogbones, the UVTools software and a custom cleaning stand effectively facilitated the print-pause-print process, ensuring clean material interfaces. The tensile testing results showed that the ultimate tensile strength (UTS) of multi-material dogbones increased to 2.43 MPa, surpassing the 2.28 MPa UTS of single-material Liqcreate Elastomer-X dogbones. This improvement is attributed to the strong and possibly covalent interface bonding, which promotes an even stress distribution.

In order to ensure that microfluidic devices can withstand operational stresses, Finite Element Method (FEM) simulations were employed on several diameter membranes for the valve, which are created out of the flexible material of which the mechanical properties are already known. An exemplary valve was designed and it's membrane with various diameters was simulated in Solidworks to deflect 80 µm, these numerical simulations were validated against an analytical method from relevant literature. It was found that the pressures from FEM simulations and the analytical method are very similar, except for a 1 mm diameter membrane with a thickness

of 100 µm, implicating that this analytical approach is only applicable to very thin membranes or that the mesh should be improved by using a mesh sensitivity analysis. Finally, as a showcase of the newly developed protocol a multi-material structure was created with 2 material interfaces (rigid - soft - rigid).

In conclusion, to develop a novel 3D printing protocol which enables for the fabrication of high-resolution and multi-material microfluidic devices, several aspects have to be taken into account. The print process was optimized for the specific printer and resin, these parameters led to the minimum feature size of the rigid material, which the printer can accurately reproduce. To expand the research to multi-material devices, UVTools software and custom equipment were employed, leading to multi-material dogbones. This already answers the main research question, because this method can be expanded to an arbitrary number of multi-material interfaces. An exemplary valve was designed using Solidworks, and FEM simulations and analytical calculations of the isolated membrane were conducted. Lastly, a showcase was presented using both materials to create 2 material interfaces. With all information combined, this thesis establishes a strong foundation for the future development of complex, multi-material microfluidic devices using MMAM on affordable MSLA 3D printers. Furthermore, the developed protocol has the potential to be expanded to various fields where both multi-material and precise fabrication techniques are of key importance.

8.2. Future work

While this thesis has demonstrated the potential of multi-material additive manufacturing (MMAM) for fabricating multi-material microfluidic devices, several limitations were identified that might require further investigation. One notable area is the alignment error between layers. It was assumed that eliminating the need to remove the build plate would negate alignment inaccuracies. However, this assumption remains unverified and to fully address this, the linear stage's precision and the printer's overall alignment accuracy must be assessed. If alignment issues are confirmed, improvements such as a higher-precision linear stage or investing in a more advanced printer may resolve the problem.

The ultrasonic cleaning process also presents an opportunity for improvement. First, the Nanografi Ultrasonic Processor used in this research is designed for sample homogenization and is limited to localized cleaning close to and around the tip. Globally cleaning the build plate is a challenge using this device, normal ultrasonic cleaners like the Sonorex create ultrasonic sound waves across the whole area. Therefore, A custom designed ultrasonic cleaner could provide more consistent and thorough cleaning across the entire build plate, addressing these limitations. Second, cleaning procedures for Liqcreate samples also require optimization. The observed swelling and shiny spots during cleaning with IPA might be mitigated by using dedicated cleaning solvents instead of IPA, such as those provided by Liqcreate. This alternative cleaning approach could enhance the dimensional stability and surface quality of printed parts.

Besides, problems exist to capture the true shape of transparent 3D printed grooves. It was observed that the Keyence VHX-6000 doesn't capture the details of transparent objects, therefore more advanced 3D imaging techniques should be employed or a material with a lower transparency has to be selected. These methods would provide insights into channel depths and shapes, ensuring design accuracy and functionality.

Another significant limitation relates to the membrane's interaction with the valve walls. This interaction was left out of consideration in the simulations, potentially leading to deviations between FEM simulated and real-world performance. To create a more realistic simulation, future simulations should simulate the entire valve, with its integrated membrane, to achieve a more accurate representation of its behavior under operating conditions. Also, a mesh sensitivity analysis, which can prove critical for the validation of FEM simulations in certain scenarios, was not performed in this study due to time constraints. This sensitivity analysis makes sure that the simulation results are independent of the mesh size, which provides more confidence in the accuracy and reliability of the model's behavior. Therefore, future work should include a systematic mesh sensitivity analysis to confirm that the chosen mesh resolution is sufficient for accurately capturing the membrane's behavior and to identify any discrepancies that could arise from inadequate mesh refinement. Incorporating this step would enhance the credibility of the FEM results.

Further exploration of layer-by-layer MMAM processes could shed light on the mechanics of material bonding and stress distribution at interfaces, which remain under explored in this thesis. Additionally, elastomeric materials exhibit hysteresis losses, Liqcreate Elastomer-X as used in this study has not been analyzed for hysteresis. This leaves a gap in the understanding of its performance under cyclic loading. Incorporating these analyses could refine the design and functionality of future devices.

Addressing these challenges in future work will strengthen the reliability and applicability of MMAM to aid in the creation of high-resolution, multi-material microfluidic devices and other advanced structures.

A

Protocols

A.1. Cleaning a single material print

Step 1

Remove part from buildplate

1. Use the metal scraper to carefully detach the printed part from the build plate, avoid damage to the part and/or build plate.

Step 2

Initial rinse in Isopropyl Alcohol (IPA)

1. Place the part in a beaker filled with IPA.

Step 3

Ultrasonic cleaning

1. Transfer the beaker with the part into the ultrasonic cleaner. The ultrasonic cleaner can be filled with demineralized water or IPA.
2. Anycubic High Clear can be cleaned by 10 minutes of ultrasonic cleaning. For Liqcreate Elastomer-X, use 25 to 30 minutes.

Step 4

Dry the part

1. Remove the part from the beaker using tweezers.
2. Use compressed air or nitrogren to blow out excess solvent until the part is dry.

Step 5

Final inspection

1. Inspect the part for any uncured resin or defects.

Step 6

Dispose of waste properly

1. Dispose of the used IPA and resin residues according to the lab rules.

A.2. Pause and cleaning step for MMAM

Step 1

Before pause

1. Stay in proximity of the printer and be ready for step 2.

Step 2

During pause

1. When the printer pauses, press the pause button on the printer.
2. Cover the build plate using aluminum foil.
3. Remove the resin vat containing material A.
4. Place a protective layer (cleanroom tissue or aluminum foil) on top of the LCD screen.
5. Place the cleaning stand and remove the aluminum foil from the build plate.
6. Raise the IPA bath and fill with IPA until the build plate is fully submerged.
7. Turn the ultrasonic processor on and monitor the IPA temperature during ultrasonic cleaning.
8. Turn the ultrasonic processor off and lower the IPA bath, wait for the part to dry or blow dry using compressed air or nitrogen.
9. Remove the cleaning stand and protective layer from the LCD screen, and install the resin vat containing material B.
10. Resume printing using material B.

Step 3

After pause

1. Clean the object as described in Appendix A.1 OR
2. Stay in proximity of the printer for the next pause step.

A.3. Measuring the resolution block

Step 1

Taking pictures

1. Take a picture of several grooves using the Keyence microscope. Be sure to enable the scale bar function in the software. For example, a picture of a 150 µm and 200 µm sample is shown in Figure 5.2.

Step 2

Processing the pictures

1. Import the picture in the ImageJ software using the ”File” menu and choose ”open”, or press CTRL + O.
2. Go to the ”image” menu, choose ”type” and lastly choose ”8 bit” to simplify the picture for the software.
3. In ImageJ, zoom in on the scale bar and trace a straight line on top of this scale bar. Then go to the ”Analyze” menu and choose ”Set scale”. The scale is now set with respect to the scale bar.
4. Go to the ”Process” menu and choose the option ”Find edges”. This setting will automatically find all edges, such as boundaries of grooves in this case.
5. Go to the ”Process” menu again, choose the option ”Binary” and press ”Make binary”. This converts the image to a binary format, in which every pixel is either black (0) or white (1 or 255).
6. The result of the previous steps may result in an inverted picture, in which the background is black instead of white. When this happens, go to the ”Edit” menu and choose the option ”Invert”, this will automatically invert the image making the background white and the previously found edges black.

Step 3

Taking measurements

1. To fit an ellipse (with both length and width measurements), go to the ”analyze” menu and choose the option ”set measurements” and tick the ”ellipse” box. Now for every measurement an ellipse is fitted inside the boundaries of each groove.
2. To select the region to analyze, draw a rectangle using the ”Rectangle” feature around the grooves of interest.
3. To analyze the particles go to the ”Analyze” menu, choose the option ”Analyze particles”, tick the box ”Clear results” to delete previous measurements. Tick the box ”Display results” to display the results when the ellipses are fitted. Tick the box ”Add to manager” to see labels on the various samples, making it possible to distinguish the various grooves and directions. Tick the box ”Overlay” to create an overlay with the labels which are added to the manager. Choose ”Ellipses” to show the ellipses when the measurement is complete, this way it can be verified which ellipses are fitted correctly.

B

Matlab code

B.1. Create a linear fit to determine the Young's modulus

This Matlab code is used to create a linear fit which fits the first portion of the graph best. The value of the Young's modulus in the title is multiplied by 100 to reverse the percentage calculation, which would otherwise lead to a 100 times smaller Young's modulus.

```
% Load the .TRA file into MATLAB
data = readtable('tensile dog bone 3D print16 sept7.tra', 'FileType','text');

% Extract columns: Standard Force and Strain
strain = data{:, 'Strain1'}*100/30.58;    % The column is named 'Strain1'
force = data{:, 'StandardForce1'}/1e6;  % The column is named 'StandardForce1'

% Nominal area of the sample (6mm by 2mm)
nominal_area = 6 * 2;  % Area in mm^2
nominal_area_m2 = nominal_area * 1e-6;  % Convert to m^2

% Calculate stress (Stress = Force / Area)
stress = force / nominal_area_m2;

% Plot the original Stress vs. Strain curve
figure;
plot(strain, stress, 'r', 'LineWidth', 1.5);
hold on;

% Automated detection of linear region for Young's modulus calculation
best_r2 = 0;
best_slope = 0;
best_intercept = 0;

% Iterate through different regions of the curve to find the most linear region
for i = 1:length(strain)-10  % Start from 1 to avoid too small portions
    for j = i+10:length(strain)  % Ensure at least 10 points are used for
       fitting
        % Take the current slice of data
        strain_slice = strain(i:j);
        stress_slice = stress(i:j);

        % Perform linear fit
        coeffs = polyfit(strain_slice, stress_slice, 1); % Linear fit
        fit_line = polyval(coeffs, strain_slice);

        % Calculate R-squared to determine goodness of fit
        ss_res = sum((stress_slice - fit_line).^2);  % Residual sum of squares
        ss_tot = sum((stress_slice - mean(stress_slice)).^2);  % Total sum of
           squares
```

```
        r2 = 1 - (ss_res / ss_tot);  % Coefficient of determination (R-squared)

        % Check if this region has a better linear fit
        if r2 > best_r2
            best_r2 = r2;
            best_slope = coeffs(1);  % Save the slope (Young's modulus)
            best_intercept = coeffs(2);
            best_range = [i, j];  % Save the best fitting range
        end
    end
end

% Use the best fitting region to plot the linear fit
strain_linear = strain(best_range(1):best_range(2));
stress_linear = stress(best_range(1):best_range(2));
fit_line = best_intercept + best_slope * strain_linear;

% Plot the linear fit line on the graph
plot(strain_linear, fit_line, '--g', 'LineWidth', 1.5);

% Find the ultimate tensile strength (UTS) and its corresponding strain
[stress_max, idx_max_stress] = max(stress);
strain_at_max_stress = strain(idx_max_stress);

% Plot the UTS point
plot(strain_at_max_stress, stress_max, 'ko', 'MarkerSize', 8, 'MarkerFaceColor',
    'k');
text(strain_at_max_stress, stress_max, ['UTS: (', num2str(strain_at_max_stress,
   '%.2f'), ', ', num2str(stress_max, '%.2e'), ' Pa)'], 'VerticalAlignment', '
   top');

% Find the tensile stress at break
% Tensile stress at break is the last point before a significant drop in stress
% We'll define a "significant drop" as a decrease of more than 10% from UTS
drop_threshold = 0.1 * stress_max;  % 10% drop from UTS
for k = idx_max_stress:length(stress)-1
    if (stress(k) - stress(k+1)) > drop_threshold
        break_idx = k;  % The last point before the significant drop
        break;
    end
end
strain_at_break = strain(break_idx);
stress_at_break = stress(break_idx);

% Plot the tensile stress at break
plot(strain_at_break, stress_at_break, 'bo', 'MarkerSize', 8, 'MarkerFaceColor',
    'b');
text(strain_at_break, stress_at_break, ['Break: (', num2str(strain_at_break, '
   %.2f'), ', ', num2str(stress_at_break, '%.2e'), ' Pa)'], 'VerticalAlignment',
    'bottom');

% Add labels and title
xlabel('Strain');
ylabel('Stress (Pa)');
title(['Stress vs. Strain with Young''s Modulus Fit (E = ', num2str(best_slope
   *100, '%.2e'), ' Pa)']);
legend('Stress vs. Strain', 'Linear Fit', 'Ultimate Tensile Strength (UTS)', '
   Tensile Stress at Break');
grid on;
```

```
% Display the value of Young's modulus, R-squared, UTS, and tensile stress at
    break
disp(['Young''s Modulus: ', num2str(best_slope*100), ' Pa']);
disp(['Best R^2: ', num2str(best_r2)]);
disp(['Ultimate Tensile Strength (UTS): ', num2str(stress_max), ' Pa']);
disp(['Tensile Stress at Break: ', num2str(stress_at_break), ' Pa']);
```

B.2. Create a linear fit eliminating first datapoints

This Matlab code is used to skip the first few data-points in case the first data-points are not valid for the linear fit. The value of the Young's modulus in the title is multiplied by 100 to reverse the percentage calculation, which would otherwise lead to a 100 times smaller Young's modulus.

```
% Load the .TRA file into MATLAB
% Replace 'yourfile.tra' with the name of your file
data = readtable('tensile dog bone 3D print16 sept11.tra', 'FileType','text');

% Extract columns: Standard Force and Strain
strain = data{:, 'Strain1'}*100/30.58;    % The column is named 'Strain1'
force = data{:, 'StandardForce1'}/1e6;  % The column is named 'StandardForce1'

% Nominal area of the sample (6mm by 2mm)
nominal_area = 6 * 2;  % Area in mm^2
nominal_area_m2 = nominal_area * 1e-6;  % Convert to m^2

% Calculate stress (Stress = Force / Area)
stress = force / nominal_area_m2;

% Plot the original Stress vs. Strain curve
figure;
plot(strain, stress, 'r', 'LineWidth', 1.5);
hold on;

% Automated detection of linear region for Young's modulus calculation
best_r2 = 0;
best_slope = 0;
best_intercept = 0;

% Ignore the first 10 data points for the linear approximation
start_idx = 5;  % Start the linear fit search from the 11th data point

% Iterate through different regions of the curve to find the most linear region
for i = start_idx:length(strain)-10  % Start from the 11th data point to avoid
    too small portions
    for j = i+10:length(strain)  % Ensure at least 10 points are used for
       fitting
        % Take the current slice of data
        strain_slice = strain(i:j);
        stress_slice = stress(i:j);

        % Perform linear fit
        coeffs = polyfit(strain_slice, stress_slice, 1); % Linear fit
        fit_line = polyval(coeffs, strain_slice);

        % Calculate R-squared to determine goodness of fit
        ss_res = sum((stress_slice - fit_line).^2);  % Residual sum of squares
        ss_tot = sum((stress_slice - mean(stress_slice)).^2);  % Total sum of
           squares
        r2 = 1 - (ss_res / ss_tot);  % Coefficient of determination (R-squared)

        % Check if this region has a better linear fit
        if r2 > best_r2
            best_r2 = r2;
            best_slope = coeffs(1);  % Save the slope (Young's modulus)
            best_intercept = coeffs(2);
            best_range = [i, j];  % Save the best fitting range
        end
    end
end
```

```
% Use the best fitting region to plot the linear fit
strain_linear = strain(best_range(1):best_range(2));
stress_linear = stress(best_range(1):best_range(2));
fit_line = best_intercept + best_slope * strain_linear;

% Plot the linear fit line on the graph
plot(strain_linear, fit_line, '--g', 'LineWidth', 1.5);

% Find the ultimate tensile strength (UTS) and its corresponding strain
[stress_max, idx_max_stress] = max(stress);
strain_at_max_stress = strain(idx_max_stress);

% Plot the UTS point
plot(strain_at_max_stress, stress_max, 'ko', 'MarkerSize', 8, 'MarkerFaceColor',
    'k');
text(strain_at_max_stress, stress_max, ['(', num2str(strain_at_max_stress, '%.2f
    '), ', ', num2str(stress_max, '%.2e'), ' MPa)'], 'VerticalAlignment', 'bottom
    ', 'HorizontalAlignment', 'right');

% Find the tensile stress at break
% Tensile stress at break is the last point before a significant drop in stress
% We'll define a "significant drop" as a decrease of more than 10% from UTS
drop_threshold = 0.1 * stress_max;  % 10% drop from UTS
for k = idx_max_stress:length(stress)-1
    if (stress(k) - stress(k+1)) > drop_threshold
        break_idx = k;  % The last point before the significant drop
        break;
    end
end
strain_at_break = strain(break_idx);
stress_at_break = stress(break_idx);

% Plot the tensile stress at break
plot(strain_at_break, stress_at_break, 'bo', 'MarkerSize', 8, 'MarkerFaceColor',
    'b');
text(strain_at_break, stress_at_break, ['(', num2str(strain_at_break, '%.2f'), '
    , ', num2str(stress_at_break, '%.2e'), ' MPa)'], 'VerticalAlignment', 'top',
    'HorizontalAlignment', 'right');

% Add labels and title
xlabel('Strain (%)');
ylabel('Stress (MPa)');
title(['Stress vs. Strain with Young''s Modulus Fit (E = ', num2str(best_slope
    *100, '%.2e'), ' MPa)']);
legend('Stress vs. Strain', 'Linear Fit', 'Ultimate Tensile Strength (UTS)', '
    Tensile Stress at Break');
grid on;

% Display the value of Young's modulus, R-squared, UTS, and tensile stress at
    break
disp(['Young''s Modulus: ', num2str(best_slope*1e8), ' MPa']);
disp(['Best R^2: ', num2str(best_r2)]);
disp(['Ultimate Tensile Strength (UTS): ', num2str(stress_max), ' MPa']);
disp(['Tensile Stress at Break: ', num2str(stress_at_break), ' MPa']);
```

B.3. Graphs for Anycubic High Clear

This Matlab code is used to create graphs of the data obtained from the graphs, which are generated by the previous 2 matlab codes.

```
% Data for each sample and each test
youngs = [
    1088527894, 1038555852, 1116494934;  % Anyc HC - 5S, 5 min
    1107914033, 1062545818, 1152166722;  % Anyc HC - 10S, 5 min
    1124046019, 1152188605, 1197788062;  % Anyc HC - 5S, 30 min
    1187091567, 1228169560, 1175796189   % Anyc HC - 10S, 30 min
];

uts = [
    42778508.50, 40876950.58, 42494590.76;  % Anyc HC - 5S, 5 min
    42702418.01, 44631164.55, 43837870.28;  % Anyc HC - 10S, 5 min
    45998113.00, 46198852.54, 45490193.68;  % Anyc HC - 5S, 30 min
    49816818.24, 51765747.07, 50461390.18   % Anyc HC - 10S, 30 min
];

stress_at_break = [
    40316630.05, 38777336.12, 40730852.76;  % Anyc HC - 5S, 5 min
    40341623.94, 41734252.93, 40957186.38;  % Anyc HC - 10S, 5 min
    42953033.45, 42862192.79, 42051704.41;  % Anyc HC - 5S, 30 min
    47450754.80, 51057922.36, 47624033.61   % Anyc HC - 10S, 30 min
];

% Number of tests
n_tests = 3;

% Compute averages for each sample
avg_youngs = mean(youngs, 2)/1e6;
avg_uts = mean(uts, 2)/1e6;
avg_stress_at_break = mean(stress_at_break, 2)/1e6;

% Compute standard deviations for each sample
std_youngs = std(youngs, 0, 2);
std_uts = std(uts, 0, 2);
std_stress_at_break = std(stress_at_break, 0, 2);

% Compute standard error of the mean (SEM) for each sample
sem_youngs = std_youngs / (sqrt(n_tests)*1e6);
sem_uts = std_uts / (sqrt(n_tests)*1e6);
sem_stress_at_break = std_stress_at_break / (sqrt(n_tests)*1e6);

% Labels for x-axis (samples)
%x_labels = {'Anyc. HC - 5s exposure time, 5 min post curing', 'Anyc. HC - 10s
    exposure time, 5 min post curing', 'Anyc. HC - 5s exposure time, 30 min post
    curing', 'Anyc. HC - 10s exposure time, 30 min post curing'};
x_labels = {'A', 'B', 'C', 'D'};

% Plot Young's Modulus (Averaged) with error bars
figure;
bar(avg_youngs, 'grouped');
hold on;
errorbar(1:length(avg_youngs), avg_youngs, sem_youngs, 'k', 'linestyle', 'none')
    ;
title('Average Young''s Modulus', 'FontSize', 14);
xlabel('Samples', 'FontSize', 14);
ylabel('Average Young''s Modulus (MPa)', 'FontSize', 14);
set(gca, 'FontSize', 14); % This affects the tick labels on both axes
set(gca, 'xticklabel', x_labels);
```

```
grid on;
hold off;

% Plot Ultimate Tensile Stress (UTS) (Averaged) with error bars
figure;
bar(avg_uts, 'grouped');
hold on;
errorbar(1:length(avg_uts), avg_uts, sem_uts, 'k', 'linestyle', 'none');
title('Average Ultimate Tensile Stress (UTS)', 'FontSize', 14);
xlabel('Samples', 'FontSize', 14);
ylabel('Average UTS (MPa)', 'FontSize', 14);
set(gca, 'FontSize', 14); % This affects the tick labels on both axes
set(gca, 'xticklabel', x_labels);
grid on;
hold off;

% Plot Stress at Break (Averaged) with error bars
figure;
bar(avg_stress_at_break, 'grouped');
hold on;
errorbar(1:length(avg_stress_at_break), avg_stress_at_break, sem_stress_at_break
    , 'k', 'linestyle', 'none');
title('Average Stress at Break', 'FontSize', 14);
xlabel('Samples', 'FontSize', 14);
ylabel('Average Stress at Break (MPa)', 'FontSize', 14);
set(gca, 'FontSize', 14); % This affects the tick labels on both axes
set(gca, 'xticklabel', x_labels);
grid on;
hold off;
```

B.4. Writing data to Excel

This Matlab code is used to write the .TRA data from tensile testing into an excel file which makes it easier to copy the data.

```
% Load the .TRA file into MATLAB
data = readtable('tensile dog bone 3D print16 sept30.tra', 'FileType','text');

% Extract columns: Standard Force and Strain
strain = data{:, 'Strain1'};   % The column is named 'Strain1'
force = data{:, 'StandardForce1'};  % The column is named 'Standardforce1'

% Nominal area of the sample (6mm by 2mm)
nominal_area = 6 * 2;  % Area in mm^2
nominal_area_m2 = nominal_area * 1e-6;  % Convert to m^2

% Calculate stress (Stress = Force / Area)
stress = force / nominal_area_m2;

% Define the original length of the sample (30.6mm)
initial_length_mm = 30.58;  % mm

% Convert strain to percentage (strain in percentage = (strain / initial_length)
    * 100)
strain_percentage = (strain / initial_length_mm) * 100;

% Initialize arrays to store the extracted data for Excel
strain_percentages = [];
stress_values = [];

% Loop through 10% intervals and store values
for strain_mark = 10:10:350  % Strain percentage from 10% to 350%
    % Find the index of the strain value closest to the current strain_mark
    [~, idx] = min(abs(strain_percentage - strain_mark));

    % Store strain and stress values for Excel export
    strain_percentages = [strain_percentages; strain_mark];  % Store strain mark
        (e.g., 10%, 20%, etc.)
    stress_values = [stress_values; stress(idx)];  % Store corresponding stress
       values
end

% Create a table with strain percentages and stress values
results_table = table(strain_percentages, stress_values, 'VariableNames', {'
   Strain_Percentage', 'Stress_Pa'});

% Write the table to an Excel file
writetable(results_table, 'Test30.xlsx');

% Display the generated Excel file content
disp('Stress-strain data has been written to Test30.xlsx');
```

B.5. Creating graphs for Elastomer-X with percentages

This Matlab code is used to create a single graph of an elastomer from its tensile data as stored in the .TRA file, the output shows 1 elastomer with its corresponding values for 10-350%.

```
% Load the .TRA file into MATLAB
data = readtable('tensile dog bone 3D print16 sept14.tra', 'FileType','text');

% Extract columns: Standard Force and Strain
strain = data{:, 'Strain1'};    % The column is named 'Strain1'
force = data{:, 'StandardForce1'};  % The column is named 'Standardforce1'

% Nominal area of the sample (6mm by 2mm)
nominal_area = 6 * 2;  % Area in mm^2
nominal_area_m2 = nominal_area * 1e-6;  % Convert to m^2

% Calculate stress (Stress = Force / Area)
stress = force / nominal_area_m2;

% Define the original length of the sample (30.6mm)
initial_length_mm = 30.58;  % mm

% Convert strain to percentage (strain in percentage = (strain / initial_length)
    * 100)
strain_percentage = (strain / initial_length_mm) * 100;

% Plot the original Stress vs. Strain (percentage) curve
figure;
plot(strain_percentage, stress, 'r', 'LineWidth', 1.5);
hold on;

% Add dots at every 10% strain interval and display corresponding stress values
for strain_mark = 10:10:350  % Strain percentage from 10% to 350%
    % Find the index of the strain value closest to the current strain_mark
    [~, idx] = min(abs(strain_percentage - strain_mark));

    % Plot a dot at each 10% strain interval
    plot(strain_percentage(idx), stress(idx), 'bo', 'MarkerSize', 6, '
       MarkerFaceColor', 'b');

    % Annotate each dot with its strain percentage and corresponding stress
       value
    text(strain_percentage(idx), stress(idx), ...
        [' ', num2str(strain_mark), '% (', num2str(stress(idx), '%.2e'), ' Pa)'
           ], ...
        'VerticalAlignment', 'bottom');
end

% Add labels and title
xlabel('Strain (%)');
ylabel('Stress (Pa)');
title('Stress vs. Strain with Stress Values at Every 10% Strain Interval');
grid on;

% Display the maximum stress value
[max_stress, max_idx] = max(stress);
disp(['Maximum Stress: ', num2str(max_stress), ' Pa at ', num2str(
   strain_percentage(max_idx)), '% strain']);
```

B.6. Highest MPa from each file

This Matlab code takes the highest stress across all files and gives the average value.

```
% Define file names
% file_names = {
%     'tensile dog bone 3D print16 sept13.tra',
%     'tensile dog bone 3D print16 sept14.tra',
%     'tensile dog bone 3D print16 sept15.tra',
%     'tensile dog bone 3D print16 sept16.tra',
%     'tensile dog bone 3D print16 sept17.tra',
%     'tensile dog bone 3D print16 sept18.tra',
%     'tensile dog bone 3D print16 sept19.tra',
%     'tensile dog bone 3D print16 sept20.tra',
%     'tensile dog bone 3D print16 sept21.tra',
%     'tensile dog bone 3D print16 sept22.tra',
%     'tensile dog bone 3D print16 sept23.tra',
%     'tensile dog bone 3D print16 sept24.tra',
%     'tensile dog bone 3D print16 sept25.tra',
%     'tensile dog bone 3D print16 sept26.tra',
%     'tensile dog bone 3D print16 sept27.tra',
%     'tensile dog bone 3D print16 sept28.tra',
%     'tensile dog bone 3D print16 sept29.tra',
%     'tensile dog bone 3D print16 sept30.tra',
% };

file_names = {
    'tensile dog bone Denzel 1.TRA',
    'tensile dog bone Denzel 2.TRA',
    'tensile dog bone Denzel 3.TRA',
    'tensile dog bone Denzel 4.TRA',
    'tensile dog bone Denzel 5.TRA',
    'tensile dog bone Denzel 6.TRA',
    };

% Nominal area of the sample (6mm by 2mm)
nominal_area = 6 * 2;  % Area in mm^2
nominal_area_m2 = nominal_area * 1e-6;  % Convert to m^2

% Define the original length of the sample
initial_length_mm = 30.58;  % in mm

% Initialize an array to store the highest stress from each file
highest_stresses = zeros(1, length(file_names));

% Loop through each file
for i = 1:length(file_names)
    % Load the current file
    data = readtable(file_names{i}, 'FileType', 'text');

    % Extract strain and force data
    strain = data{:, 'Strain1'};   % The column is named 'Strain1'
    force = data{:, 'StandardForce1'};  % The column is named 'StandardForce1'

    % Calculate stress (Stress = Force / Area)
    stress = force / nominal_area_m2;

    % Convert strain to percentage
    strain_percentage = (strain / initial_length_mm) * 100;

    % Find the maximum stress in the current file
    highest_stresses(i) = max(stress);
```

```
end

% Calculate the average of the highest stresses
average_highest_stress = mean(highest_stresses);

% Display the highest stresses from each file and the average
disp('Highest stress values from each file (Pa):');
disp(highest_stresses);

disp(['The average of the highest stresses across all files is: ', num2str(
    average_highest_stress), ' Pa']);
```

B.7. Young's modulus estimate for Elastomer-X

This Matlab code displays the estimated Young's modulus for Elastomer-X samples. In this file 10% of datapoints are taken into account, when "round (0.1 * num_points)" is changed to "round (1 * num_points)" the file will display the linear fit across the entire graph, instead of focusing on the first 10% of datapoints.

```
% Load the .TRA file into MATLAB
data = readtable('tensile dog bone 3D print16 sept30.tra', 'FileType', 'text');

% Extract columns: Standard Force and Strain
strain = data{:, 'Strain1'}*100/30.58;   % The column is named 'Strain1'
force = data{:, 'StandardForce1'}/1e6;  % The column is named 'StandardForce1'

% Nominal area of the sample (6mm by 2mm)
nominal_area = 6 * 2;  % Area in mm^2
nominal_area_m2 = nominal_area * 1e-6;  % Convert to m^2

% Calculate stress (Stress = Force / Area)
stress = force / nominal_area_m2;

% Focus on the first 10% of the data points
num_points = length(strain);
first_10_percent_idx = round(0.1 * num_points);
strain_subset = strain(1:first_10_percent_idx);
stress_subset = stress(1:first_10_percent_idx);

% Perform linear fit on the first 10% of the data
coeffs = polyfit(strain_subset, stress_subset, 1);  % Linear fit
youngs_modulus = coeffs(1);  % Young's modulus is the slope

% Generate extended strain values for linear fit visualization
strain_min = min(strain_subset);
strain_max = max(strain_subset);
strain_extended = linspace(strain_min - 0.01, strain_max + 0.02, 100);  %
    Slightly extend the range
fit_line_extended = polyval(coeffs, strain_extended);

% Plot the Stress vs. Strain curve
figure;
plot(strain, stress, 'r', 'LineWidth', 1.5);
hold on;

% Plot the extended linear fit line
plot(strain_extended, fit_line_extended, '--g', 'LineWidth', 1.5);

% Add labels and title
xlabel('Strain (%)');
ylabel('Stress (MPa)');
title(['Stress vs. Strain with Young''s Modulus Fit (E = ', num2str(
    youngs_modulus, '%.2e'), ' MPa)']);
legend('Stress vs. Strain', 'Linear Fit (10%)');
grid on;

% Display the value of Young's modulus
disp(['Young''s Modulus (First 10% of data): ', num2str(youngs_modulus*100), '
    MPa']);
```

B.8. Validation of pressure on membrane

This Matlab code uses the analytical formula to create graphs of Pressure (P) vs Deflection (y) on a thin circular membrane.

```
% Constants
E = 0.693e6; % Young's modulus in Pa
v = 0.495;  % Poisson's ratio (example value, adjust as needed)
t = 0.05; % Thickness in mm
r_values = [1, 2, 3] / 2; % Radii in mm for diameters 1 mm, 2 mm, and 3 mm

% Membrane deflection range (y) in mm
y = linspace(0, 0.1, 100); % Deflection range from 0 to 0.100 mm

% Pre-allocate matrix to store results
P = zeros(length(r_values), length(y));

% Calculate P for each radius and deflection
for i = 1:length(r_values)
    r = r_values(i); % Current radius in mm
    P(i, :) = (E * t^4 / r^4) .* ...
              ( (5.33 / (1 - v^2)) .* (y / t) + ...
                (2.6 / (1 - v^2)) .* (y / t).^3 );
end

% Plot P vs y for different radii
figure;
hold on;
colors = ['b', 'r', 'g']; % Color options for plots

for i = 1:length(r_values)
    plot(y, P(i, :), colors(i), 'LineWidth', 1.5, ...
        'DisplayName', ['Diameter = ', num2str(r_values(i) * 2), ' mm']); %
           Convert radius back to diameter for display
end

% Add labels, legend, and title
xlabel('Membrane Deflection, y (mm)');
ylabel('Pressure, P (Pa)');
title('Pressure vs Membrane Deflection for Diameters 1 mm, 2 mm, and 3 mm');
legend('show');
xlim([0, 0.08]); % Set X-axis range to 0 to 0.100 mm
%ylim([0, 60]); % Set Y-axis range to 0 to 400 psi
grid on;
```

B.9. Accuracy of the fit R^2

This Matlab code calculates the coefficient of determination across the linear fit, the displayed value is used to calculate an average manually.

```
% Load the .TRA file into MATLAB
data = readtable('tensile dog bone 3D print16 sept15.tra', 'FileType', 'text');

% Extract columns: Standard Force and Strain
strain = data{:, 'Strain1'}*100/30.58;   % The column is named 'Strain1'
force = data{:, 'StandardForce1'}/1e6;  % The column is named 'StandardForce1'

% Nominal area of the sample (6mm by 2mm)
nominal_area = 6 * 2;  % Area in mm^2
nominal_area_m2 = nominal_area * 1e-6;  % Convert to m^2

% Calculate stress (Stress = Force / Area)
stress = force / nominal_area_m2;

% Focus on the first 100% of the data points
num_points = length(strain);
first_10_percent_idx = round(1 * num_points);  % Adjust for first 10% of points
strain_subset = strain(1:first_10_percent_idx);
stress_subset = stress(1:first_10_percent_idx);

% Perform linear fit on the first 10% of the data
coeffs = polyfit(strain_subset, stress_subset, 1);  % Linear fit
youngs_modulus = coeffs(1);  % Young's modulus is the slope

% Generate extended strain values for linear fit visualization
strain_min = min(strain_subset);
strain_max = max(strain_subset);
strain_extended = linspace(strain_min - 0.01, strain_max + 0.02, 100);  %
    Slightly extend the range
fit_line_extended = polyval(coeffs, strain_extended);

% Plot the Stress vs. Strain curve
figure;
plot(strain, stress, 'r', 'LineWidth', 1.5);
hold on;

% Plot the extended linear fit line
plot(strain_extended, fit_line_extended, '--g', 'LineWidth', 1.5);

% Add labels and title
xlabel('Strain (mm)');
ylabel('Stress (MPa)');
title(['Stress vs. Strain with Young''s Modulus Fit (E = ', num2str(
    youngs_modulus, '%.2e'), ' Pa)']);
legend('Stress vs. Strain', 'Linear Fit (100%)');
grid on;

% Display the value of Young's modulus
disp(['Young''s Modulus (First 100% of data): ', num2str(youngs_modulus), ' Pa'
    ]);

% Assess the accuracy of the fit
assess_linear_fit(strain_subset, stress_subset, coeffs);

% Function to assess the accuracy of the linear fit
function assess_linear_fit(strain, stress, coeffs)
    % Predicted stress values from the linear fit
```

```
    stress_fit = polyval(coeffs, strain);

    % Calculate residuals
    residuals = stress - stress_fit;

    % Calculate R^2
    SS_res = sum(residuals.^2);  % Residual sum of squares
    SS_tot = sum((stress - mean(stress)).^2);  % Total sum of squares
    R2 = 1 - (SS_res / SS_tot);

    % Calculate RMSE
    RMSE = sqrt(mean(residuals.^2));

    % Display results
    disp(['R^2: ', num2str(R2)]);
    disp(['RMSE: ', num2str(RMSE), ' MPa']);

    % Plot residuals
    figure;
    plot(strain, residuals, 'o');
    xlabel('Strain (mm)');
    ylabel('Residuals (MPa)');
    title('Residuals of the Linear Fit');
    grid on;
end
```

C

Sample size pictures

C.1. Cleaning of Elastomer-X

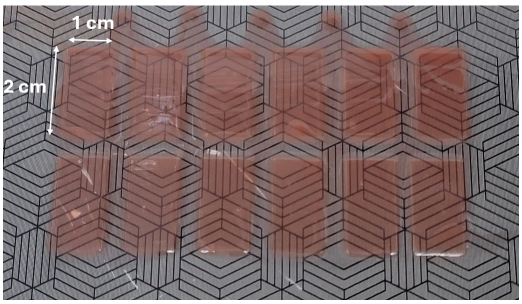

Figure C.1: Strips of 1 cm by 2 cm have been 3D printed in Liqcreate Elastomer-X with 1 wt% of red dye

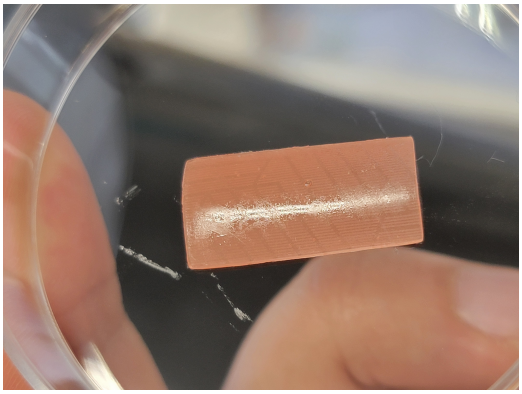

Figure C.2: 5 minutes of ultrasonic cleaning

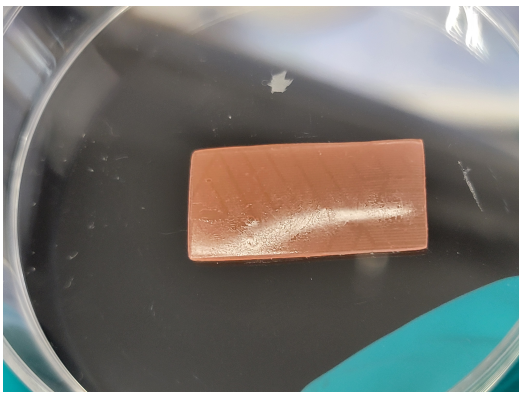

Figure C.3: 10 minutes of ultrasonic cleaning

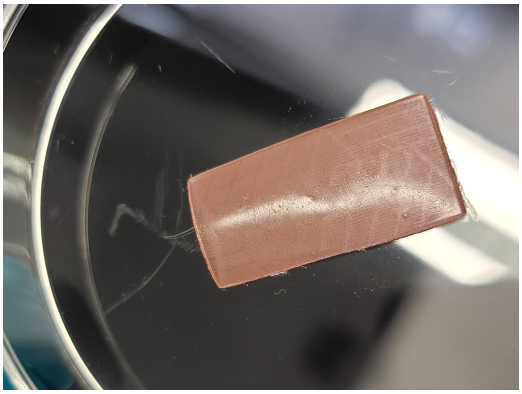

Figure C.4: 15 minutes of ultrasonic cleaning

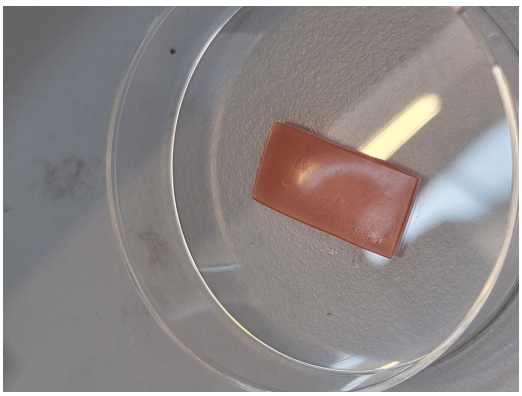

Figure C.5: 20 minutes of ultrasonic cleaning

Figure C.6: 25 minutes of ultrasonic cleaning

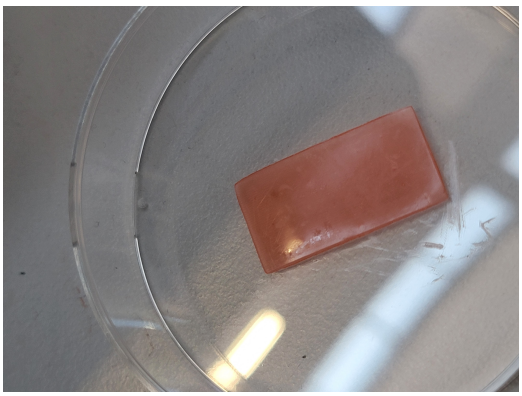

Figure C.7: 30 minutes of ultrasonic cleaning

C.2. Shrinkage of Elastomer-X

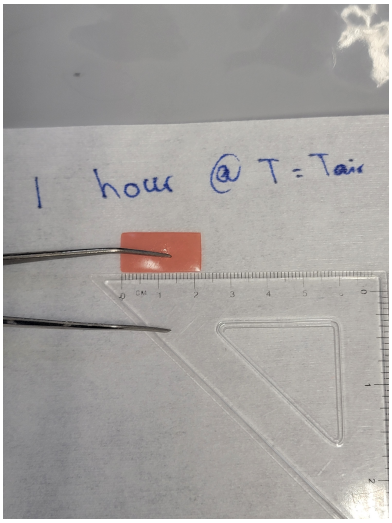

Figure C.8: 1 hour at ambient temperature.

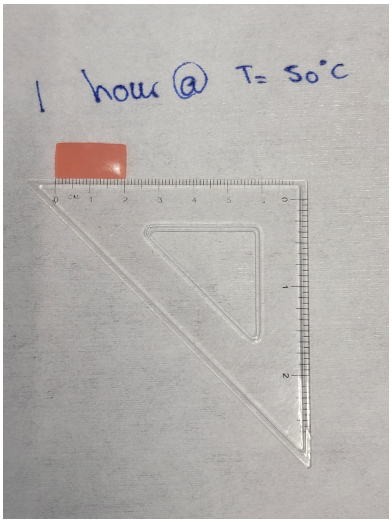

Figure C.9: 1 hour at 50 degrees Celsius.

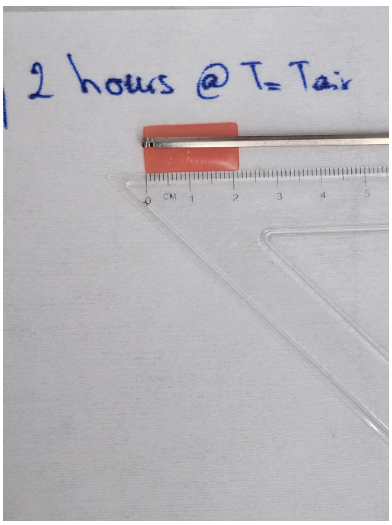

Figure C.10: 2 hours at ambient temperature.

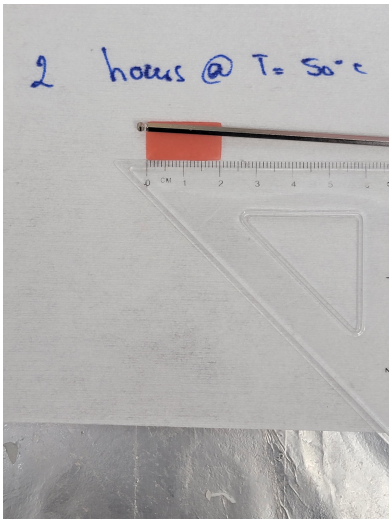

Figure C.11: 2 hours at 50 degrees Celsius.

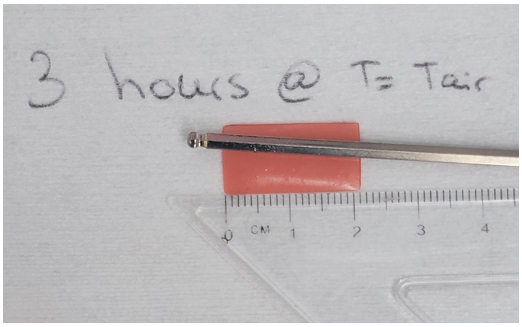

Figure C.12: 3 hours at ambient temperature.

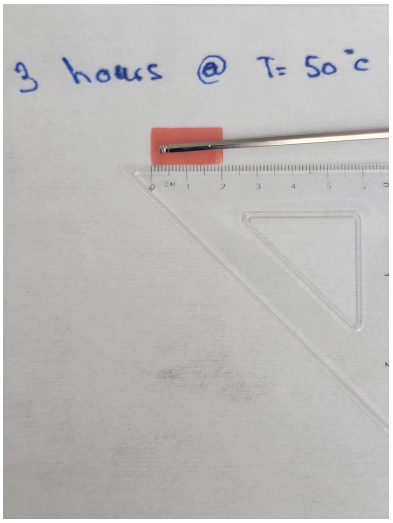

Figure C.13: 3 hours at 50 degrees Celsius.

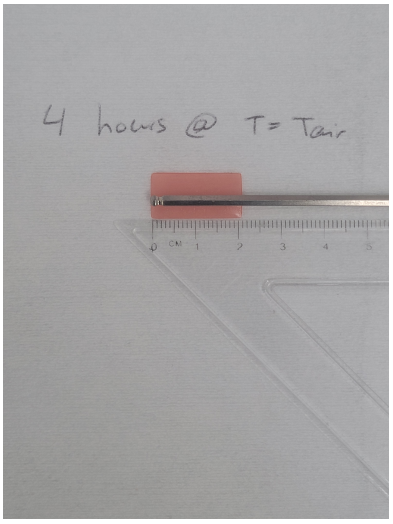

Figure C.14: 4 hours at ambient temperature.

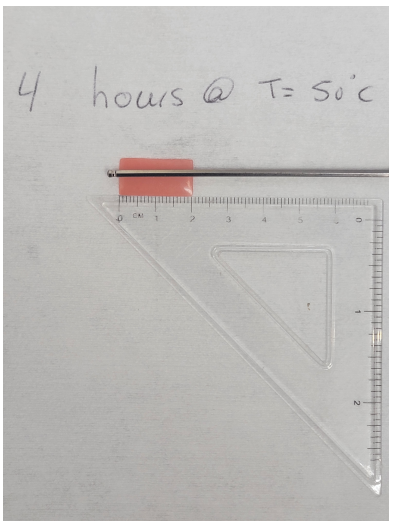

Figure C.15: 4 hours at 50 degrees Celsius.

D

FEM simulation

D.0.1. Solidworks settings

Property	Value	Units
Elastic Modulus	0.693	N/mm^2
Poisson's Ratio	0.495	N/A
Shear Modulus		N/mm^2
Mass Density	1180	kg/m^3
Tensile Strength	2.4	N/mm^2
Compressive Strength		N/mm^2
Yield Strength		N/mm^2
Thermal Expansion Coefficient		/K
Thermal Conductivity		W/(m K)

Figure D.1: Properties of the custom Liqcreate Elastomer-X material in Solidworks.

D.0.2. FEM pictures

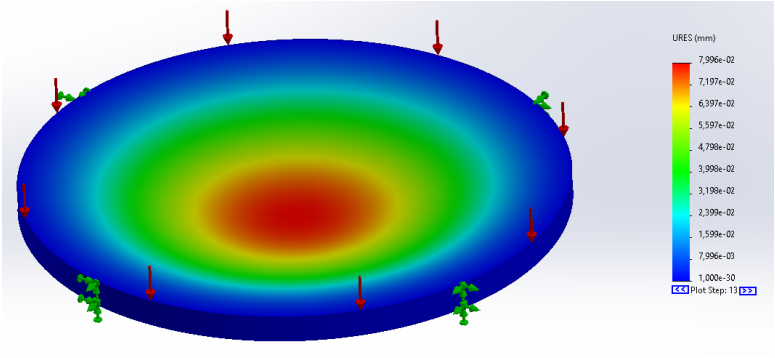

Figure D.2: Displacement for a 1 mm diameter membrane with a 50 micron thickness.

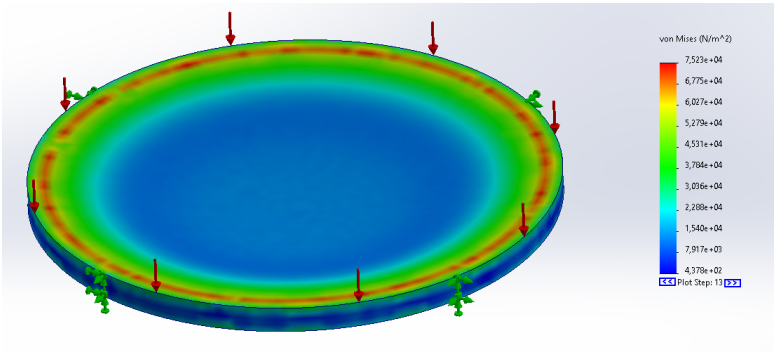

Figure D.3: Stress for a 1 mm diameter membrane with a 50 micron thickness.

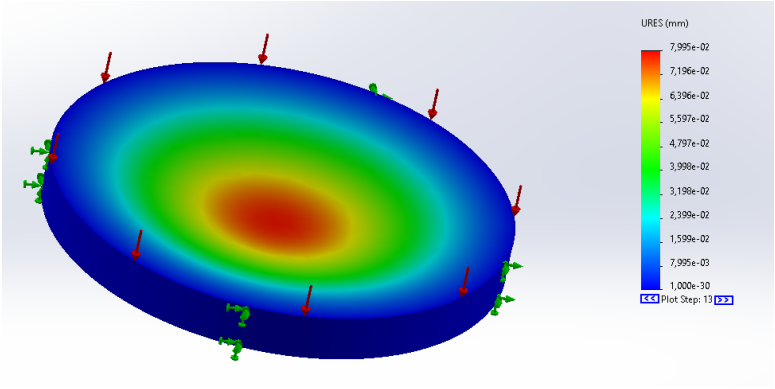

Figure D.4: Displacement for a 1 mm diameter membrane with a 100 micron thickness.

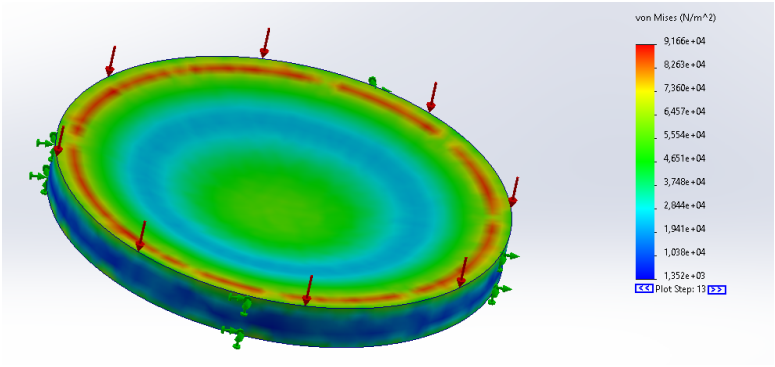

Figure D.5: Stress for a for a 1 mm diameter membrane with a 100 micron thickness.

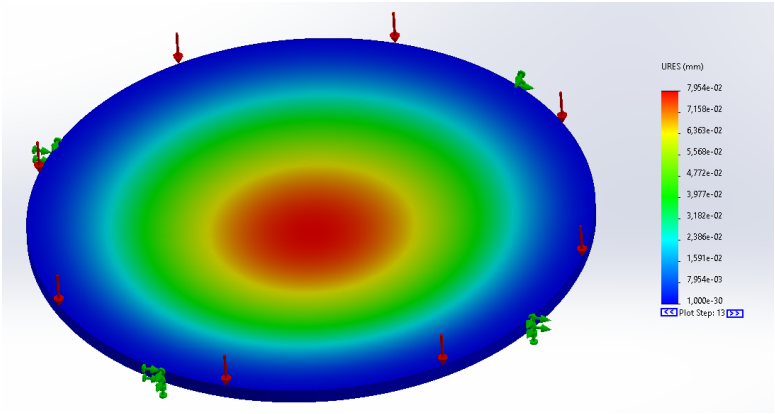

Figure D.6: Displacement for a 2 mm diameter membrane with a 50 micron thickness.

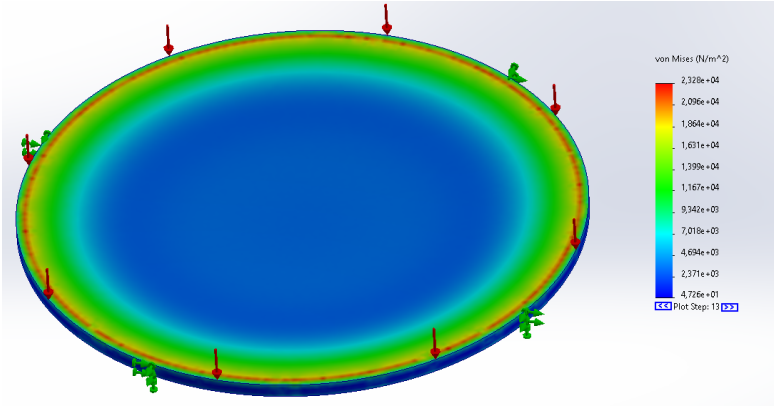

Figure D.7: Stress for a for a 2 mm diameter membrane with a 50 micron thickness.

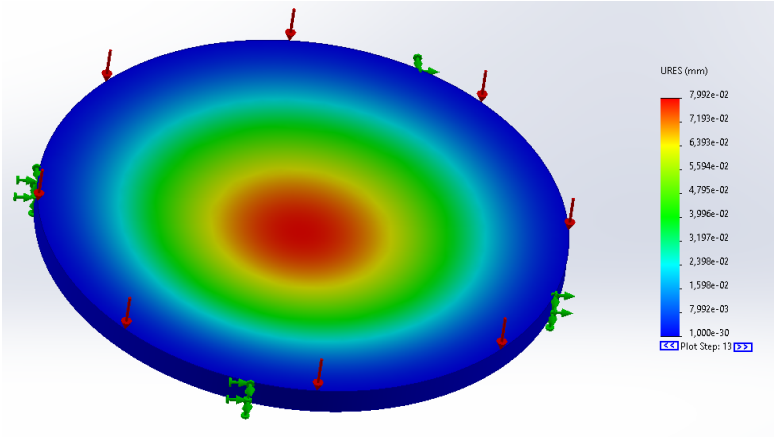

Figure D.8: Displacement for a 2 mm diameter membrane with a 100 micron thickness.

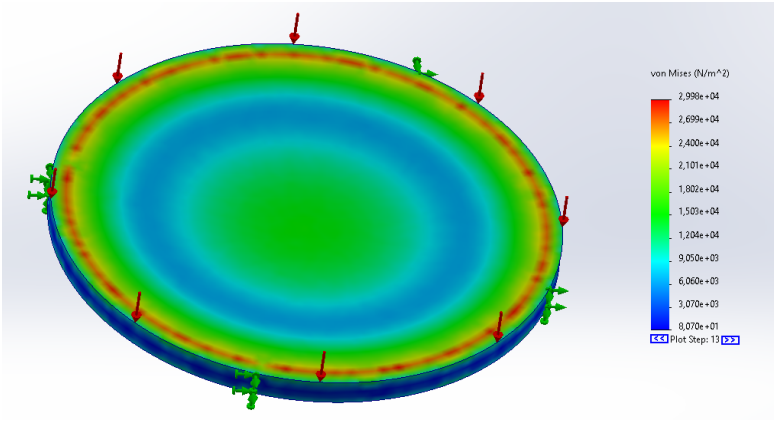

Figure D.9: Stress for a for a 2 mm diameter membrane with a 100 micron thickness.

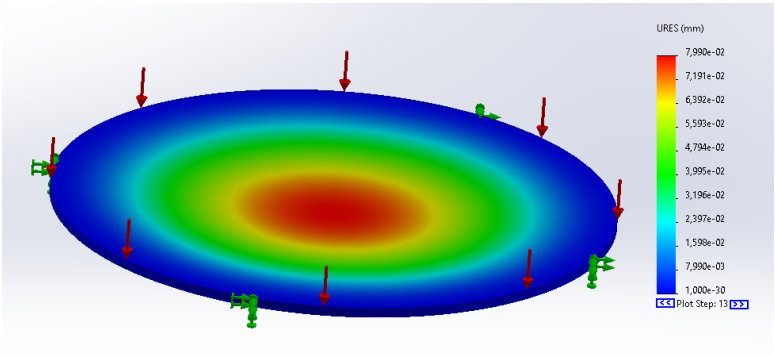

Figure D.10: Displacement for a 3 mm diameter membrane with a 50 micron thickness.

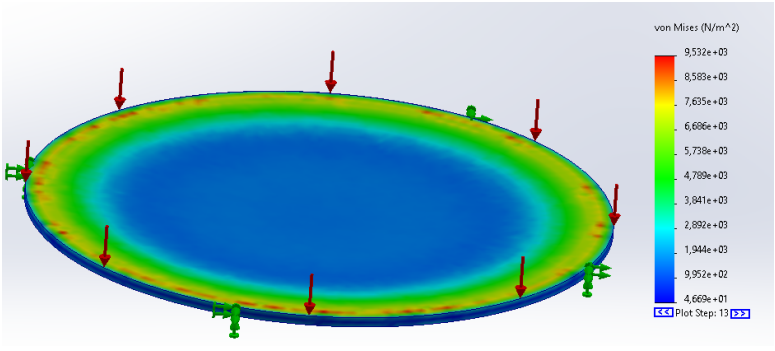

Figure D.11: Stress for a for a 3 mm diameter membrane with a 50 micron thickness.

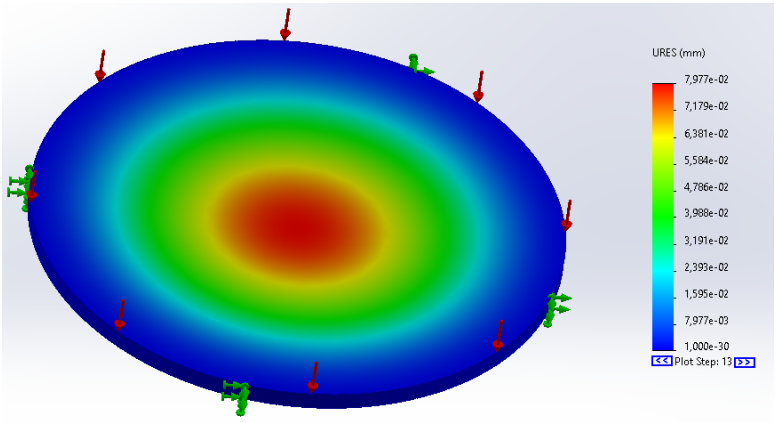

Figure D.12: Displacement for a 3 mm diameter membrane with a 100 micron thickness.

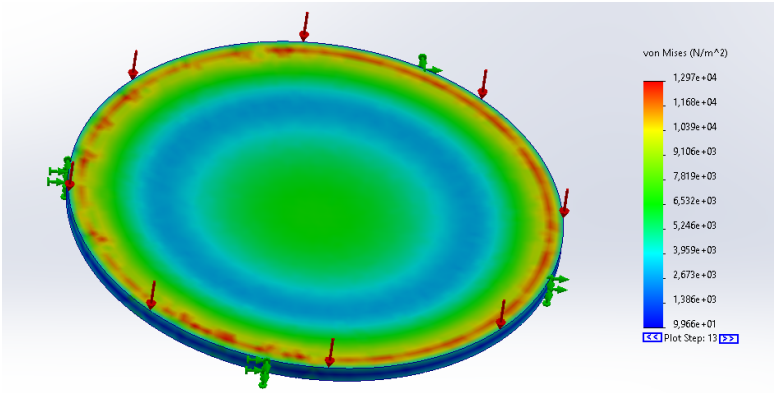

Figure D.13: Stress for a for a 3 mm diameter membrane with a 100 micron thickness.

E

Tensile testing graphs

E.1. Anycubic High Clear dogbones

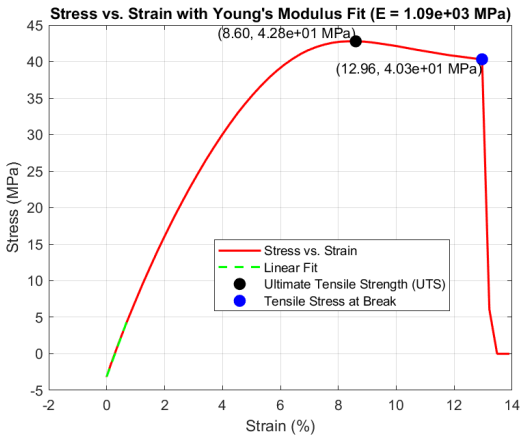

Figure E.1: Test1.

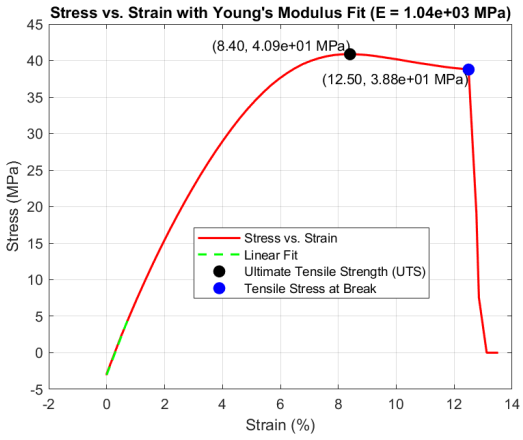

Figure E.2: Test2.

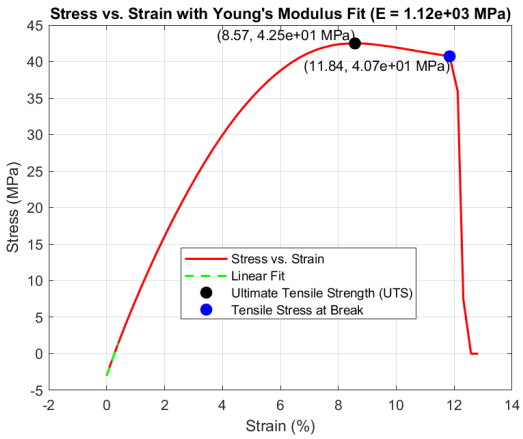

Figure E.3: Test3.

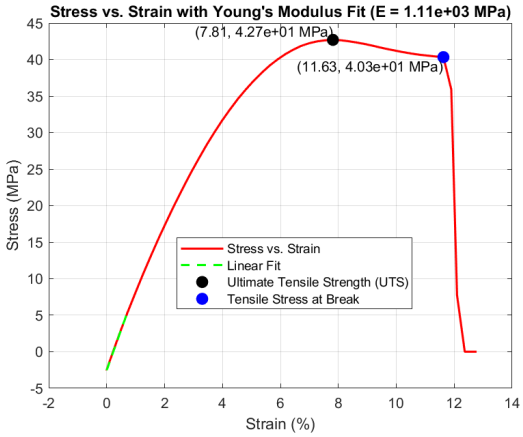

Figure E.4: Test4.

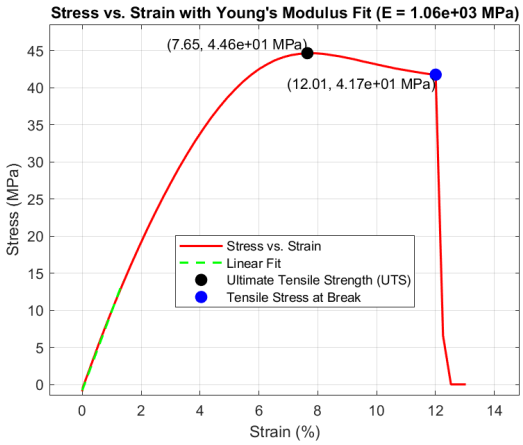

Figure E.5: Test5.

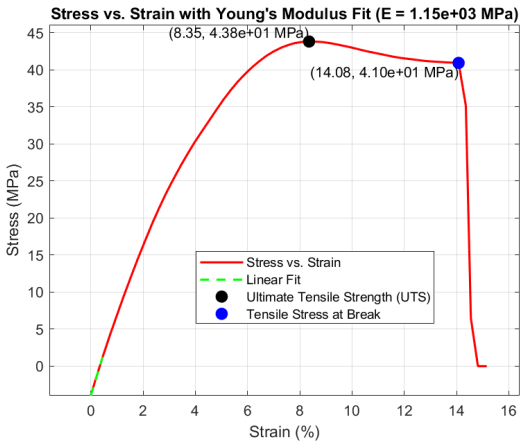

Figure E.6: Test6.

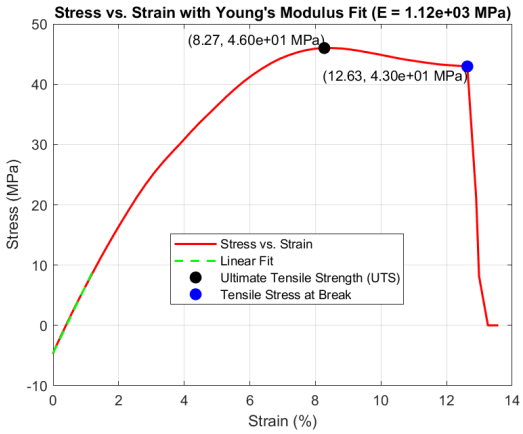

Figure E.7: Test7.

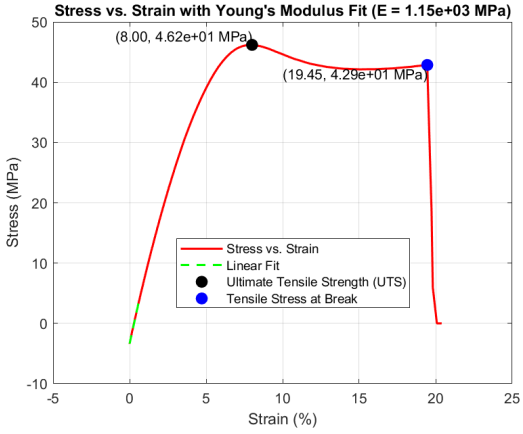

Figure E.8: Test8.

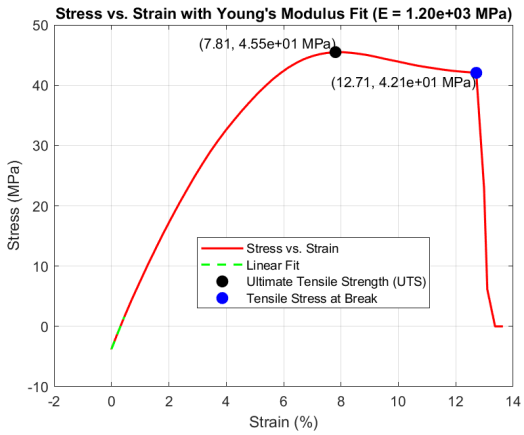

Figure E.9: Test9.

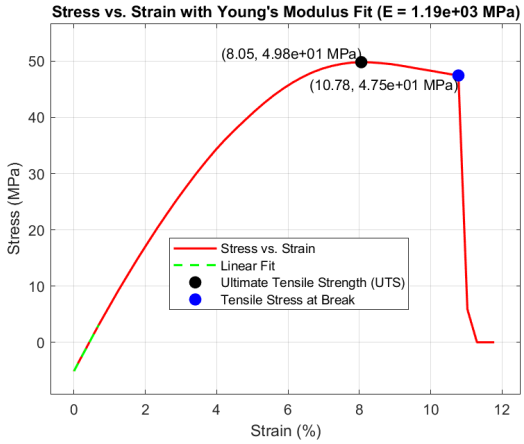

Figure E.10: Test10.

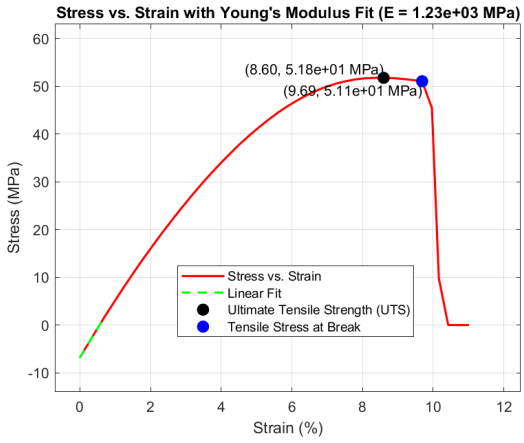

Figure E.11: Test11.

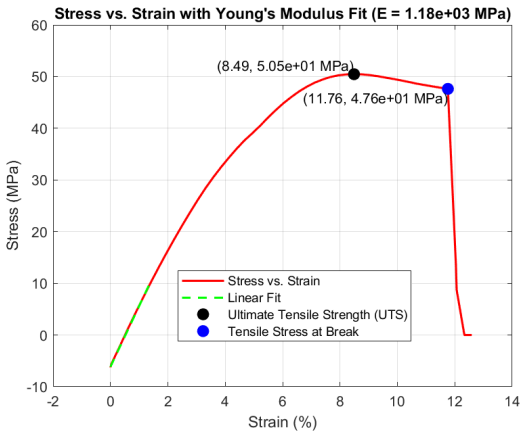

Figure E.12: Test12.

E.2. Liqcreate Elastomer-X dogbones

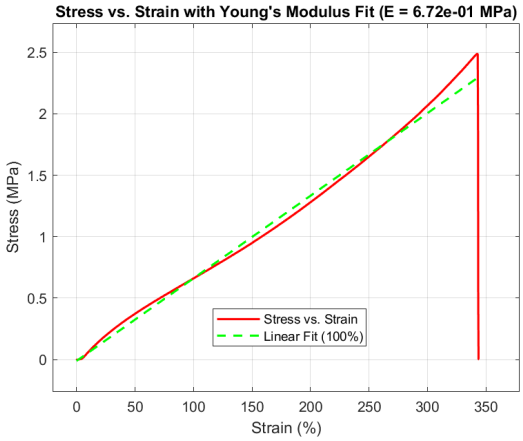

Figure E.13: Test13.

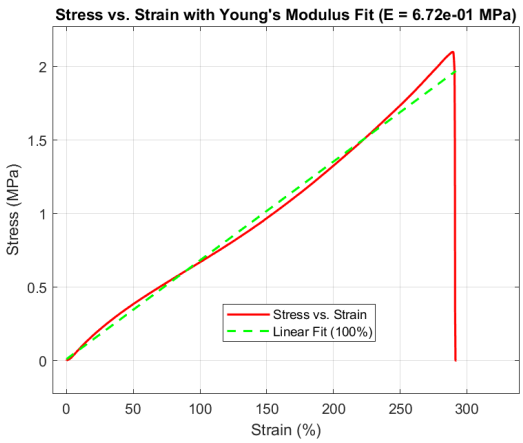

Figure E.14: Test14.

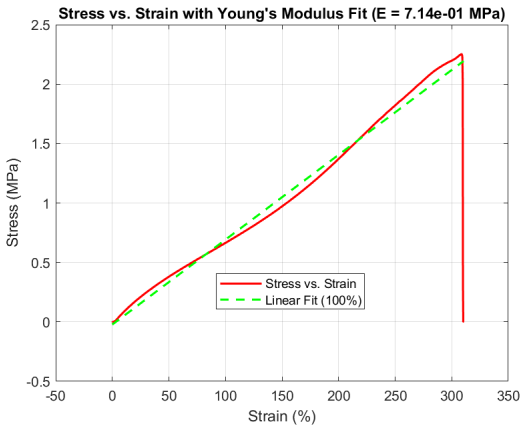

Figure E.15: Test15.

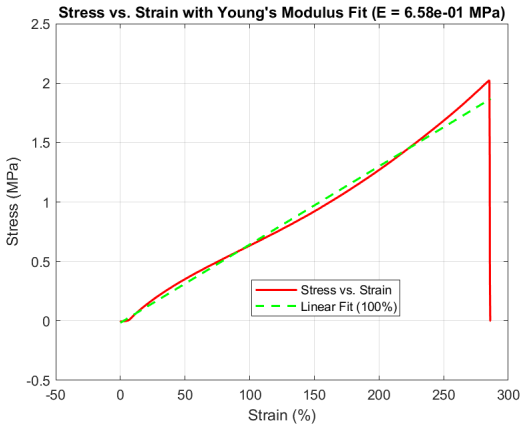

Figure E.16: Test16.

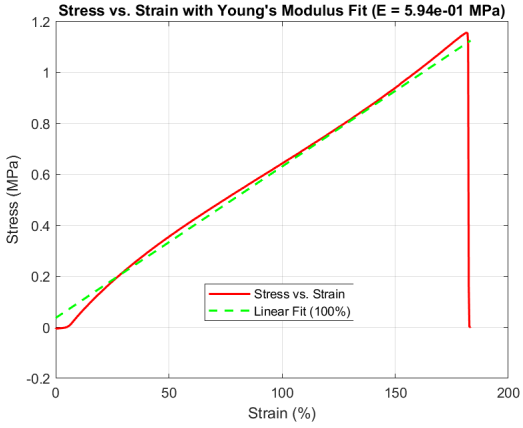

Figure E.17: Test17.

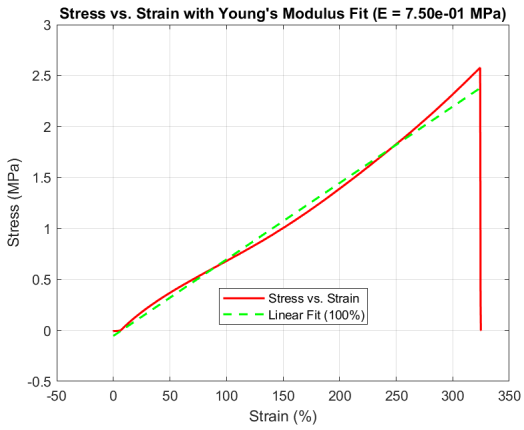

Figure E.18: Test18.

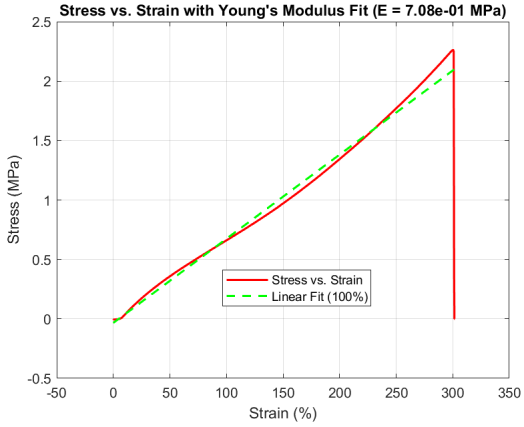

Figure E.19: Test19.

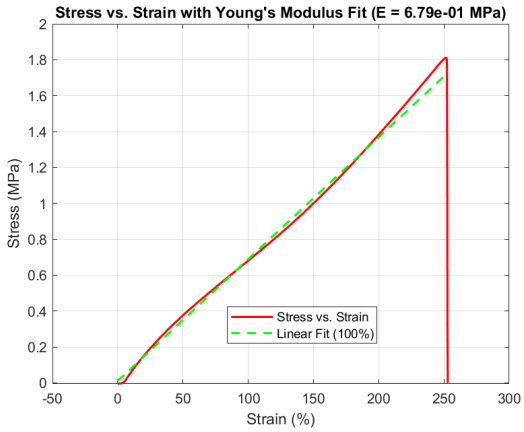

Figure E.20: Test20.

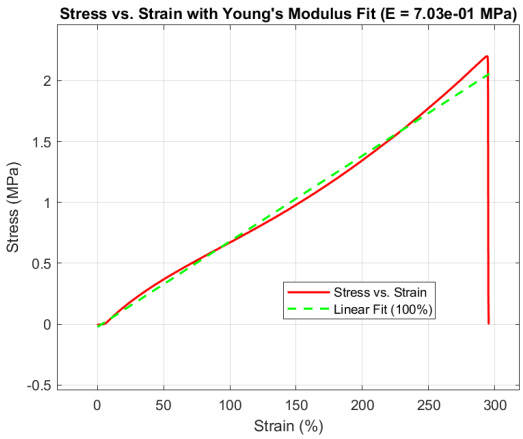

Figure E.21: Test21.

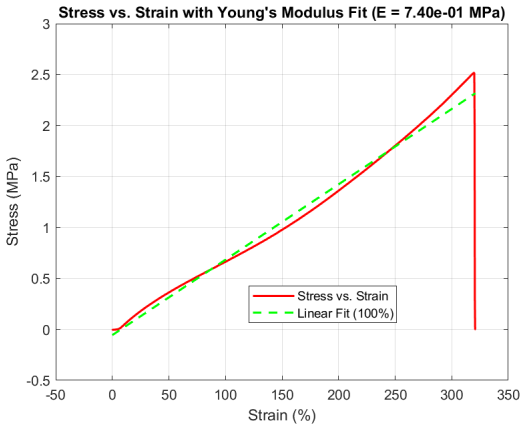

Figure E.22: Test22.

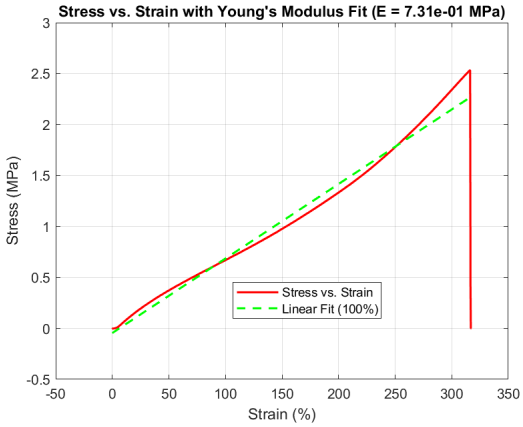

Figure E.23: Test23.

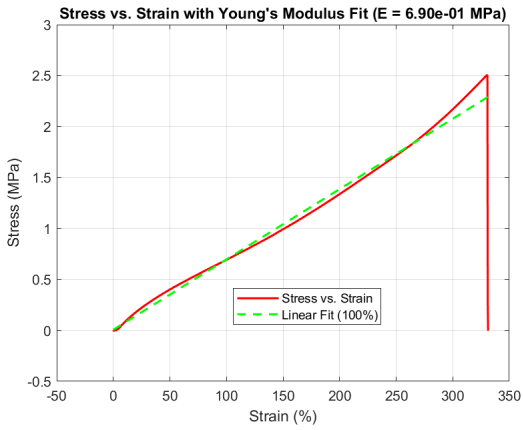

Figure E.24: Test24.

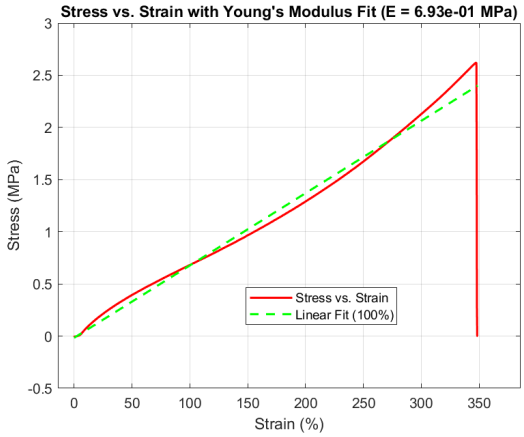

Figure E.25: Test25.

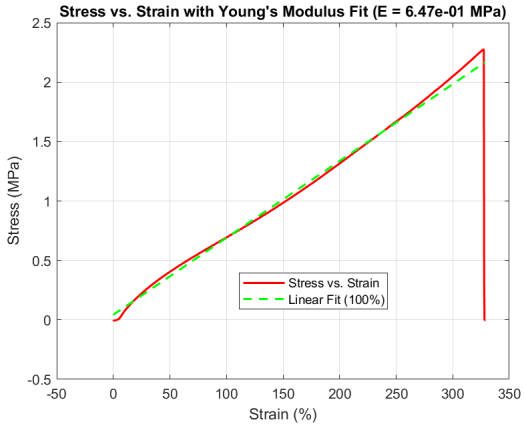

Figure E.26: Test26.

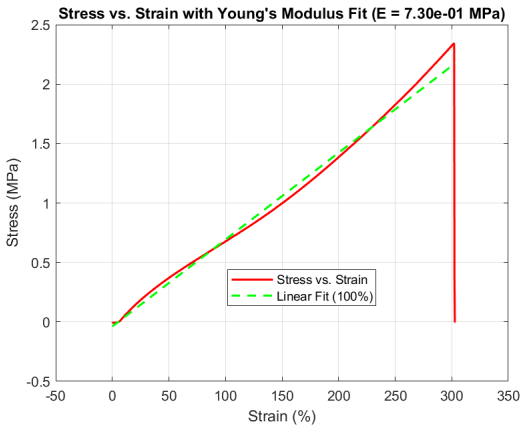

Figure E.27: Test27.

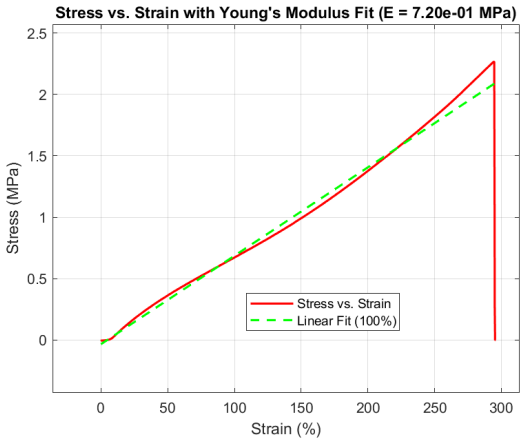

Figure E.28: Test28.

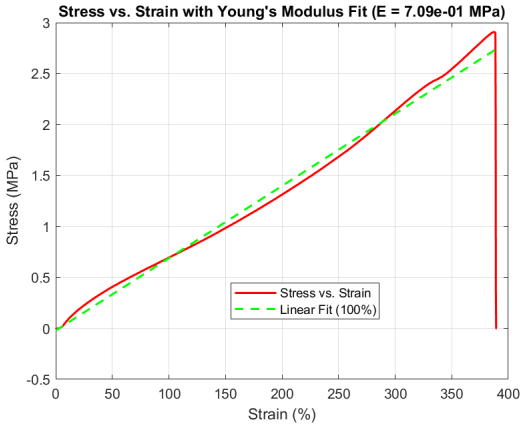

Figure E.29: Test29.

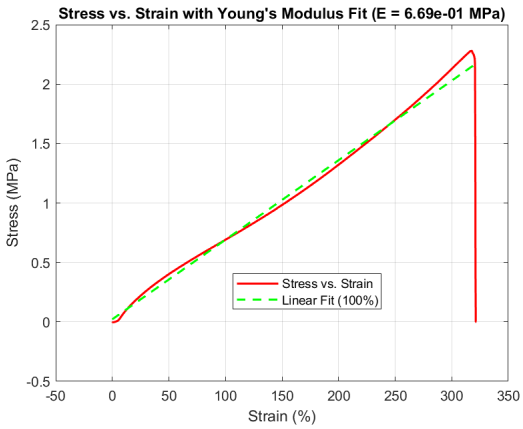

Figure E.30: Test30.

Bibliography

[1] D. J. Beebe, G. A. Mensing, and G. M. Walker, "Physics and applications of microfluidics in biology," *Annual Review of Biomedical Engineering*, vol. 4, pp. 261–286, 2002, ISSN: 15239829. DOI: 10.1146/ANNUREV.BIOENG.4.112601.125916.

[2] O. Abdulhameed, A. Al-Ahmari, W. Ameen, and S. H. Mian, "Additive manufacturing: Challenges, trends, and applications," *Advances in Mechanical Engineering*, vol. 11, 2 2019, ISSN: 16878140. DOI: 10.1177/1687814018822880.

[3] S. M. Scott and Z. Ali, *Fabrication methods for microfluidic devices: An overview*, 2021. DOI: 10.3390/mi12030319.

[4] J. Collingwood, K. D. Silva, and K. Arif, "High-speed 3d printing for microfluidics: Opportunities and challenges," *Materials Today: Proceedings*, Jun. 2023, ISSN: 2214-7853. DOI: 10.1016/J.MATPR.2023.05.683.

[5] G. Gharib, İ. Bütün, Z. Muganlı, *et al.*, "Biomedical applications of microfluidic devices: A review," *Biosensors*, vol. 12, p. 1023, 11 Nov. 2022, ISSN: 20796374. DOI: 10.3390/BIOS12111023/S1. [Online]. Available: https://www.mdpi.com/2079-6374/12/11/1023/htm%20https://www.mdpi.com/2079-6374/12/11/1023.

[6] J. Y. Qian, C. W. Hou, X. J. Li, and Z. J. Jin, *Actuation mechanism of microvalves: A review*, 2020. DOI: 10.3390/mi11020172.

[7] I. Fazal and M. C. Elwenspoek, "Design and analysis of a high pressure piezoelectric actuated microvalve," *Journal of Micromechanics and Microengineering*, vol. 17, 11 2007, ISSN: 09601317. DOI: 10.1088/0960-1317/17/11/026.

[8] X. Liu and S. Li, "An electromagnetic microvalve for pneumatic control of microfluidic systems," *Journal of Laboratory Automation*, vol. 19, 5 2014, ISSN: 22110690. DOI: 10.1177/2211068214531760.

[9] T. Liu, J. Wu, C. Xia, and Z. Qian, "A microvalve driven by a ferrofluid-based actuator," vol. 433-440, 2012. DOI: 10.4028/www.scientific.net/AMR.433-440.3767.

[10] K. Al-Aribe and G. K. Knopf, "Photoresponsive hydrogel microvalve activated by bacteriorhodopsin proton pumps," vol. 7646, 2010. DOI: 10.1117/12.848769.

[11] Q. Song, Y. Chen, P. Hou, *et al.*, "Fabrication of multi-material pneumatic actuators and microactuators using stereolithography," *Micromachines*, vol. 14, 2 2023, ISSN: 2072666X. DOI: 10.3390/mi14020244.

[12] Y. S. Lee, N. Bhattacharjee, and A. Folch, "3d-printed quake-style microvalves and micropumps," *Lab on a Chip*, vol. 18, 8 2018, ISSN: 14730189. DOI: 10.1039/c8lc00001h.

[13] M. Kaminaga, T. Ishida, and T. Omata, "Fabrication of pneumatic microvalve for tall microchannel using inclined lithography," *Micromachines*, vol. 7, 12 2016, ISSN: 2072666X. DOI: 10.3390/mi7120224.

[14] A. C. Tikka, S. F. Al-Sarawi, and D. Abbott, "Modelling a surface acoustic wave based remotely actuated microvalve," *Smart Materials and Structures*, vol. 18, 4 2009, ISSN: 09641726. DOI: 10.1088/0964-1726/18/4/045014.

[15] A. G. Niculescu, C. Chircov, A. C. Bîrcă, and A. M. Grumezescu, *Fabrication and applications of microfluidic devices: A review*, 2021. DOI: 10.3390/ijms22042011.

[16] I. Miranda, A. Souza, P. Sousa, *et al.*, *Properties and applications of pdms for biomedical engineering: A review*, 2022. DOI: 10.3390/jfb13010002.

[17] C. Ongaro, A. Betti, B. Zardin, *et al.*, "An alternative solution for microfluidic chip fabrication," *Journal of Physics: Conference Series*, vol. 2385, 1 2022, ISSN: 17426596. DOI: 10.1088/1742-6596/2385/1/012029. [Online]. Available: https://www.researchgate.net/publication/366525916_An_Alternative_Solution_for_Microfluidic_Chip_Fabrication.

[18] A. I. Shallan, P. Smejkal, M. Corban, R. M. Guijt, and M. C. Breadmore, "Cost-effective three-dimensional printing of visibly transparent microchips within minutes," *Analytical Chemistry*, vol. 86, 6 2014, ISSN: 15206882. DOI: 10.1021/ac4041857.

[19] B. K. Gale, A. R. Jafek, C. J. Lambert, *et al.*, *A review of current methods in microfluidic device fabrication and future commercialization prospects*, 2018. DOI: 10.3390/inventions3030060.

[20] *Microfluidics and its applications - an overview - renoir itn*. [Online]. Available: https://renoir-itn.eu/microfluidics-and-its-applications-an-overview/.

[21] Y. Zhang, "Three-dimensional-printing for microfluidics or the other way around?" *International Journal of Bioprinting*, vol. 5, 2 2019, ISSN: 24248002. DOI: 10.18063/ijb.v5i2.192.

[22] Y. Alapan, M. N. Hasan, R. Shen, and U. A. Gurkan, "Three-dimensional printing based hybrid manufacturing of microfluidic devices," *Journal of Nanotechnology in Engineering and Medicine*, vol. 6, 2 2015, ISSN: 19492952. DOI: 10.1115/1.4031231.

[23] K. G. Lee, K. J. Park, S. Seok, *et al.*, "3d printed modules for integrated microfluidic devices," *RSC Advances*, vol. 4, 62 2014, ISSN: 20462069. DOI: 10.1039/c4ra05072j.

[24] P. Prabhakar, R. K. Sen, N. Dwivedi, *et al.*, *3d-printed microfluidics and potential biomedical applications*, 2021. DOI: 10.3389/fnano.2021.609355.

[25] Q. Ji, J. M. Zhang, Y. Liu, *et al.*, "A modular microfluidic device via multimaterial 3d printing for emulsion generation," *Scientific Reports*, vol. 8, 1 2018, ISSN: 20452322. DOI: 10.1038/s41598-018-22756-1.

[26] K. C. Bhargava, B. Thompson, and N. Malmstadt, "Discrete elements for 3d microfluidics," *Proceedings of the National Academy of Sciences of the United States of America*, vol. 111, 42 2014, ISSN: 10916490. DOI: 10.1073/pnas.1414764111.

[27] A. E. Moumen, M. Tarfaoui, and K. Lafdi, "Modelling of the temperature and residual stress fields during 3d printing of polymer composites," *International Journal of Advanced Manufacturing Technology*, vol. 104, pp. 1661–1676, 5-8 Oct. 2019, ISSN: 14333015. DOI: 10.1007/S00170-019-03965-Y. [Online]. Available: https://www.researchgate.net/publication/333719097_Modelling_of_the_temperature_and_residual_stress_fields_during_3D_printing_of_polymer_composites.

[28] *3d printing with a 0.1 mm nozzle — cnc kitchen*. [Online]. Available: https://www.cnckitchen.com/blog/3d-printing-with-a-01-mm-nozzle.

[29] V. E. Alexopoulou, I. T. Christodoulou, and A. P. Markopoulos, "Effect of printing speed and layer height on geometrical accuracy of fdm-printed resolution holes of petg artifacts †," *Engineering Proceedings*, vol. 24, 1 2022, ISSN: 26734591. DOI: 10.3390/IECMA2022-12887.

[30] M. L. Dezaki, R. Sales, A. Zolfagharian, H. Y. Nezhad, and M. Bodaghi, "Soft pneumatic actuators with integrated resistive sensors enabled by multi-material 3d printing," *International Journal of Advanced Manufacturing Technology*, vol. 128, 9-10 2023, ISSN: 14333015. DOI: 10.1007/s00170-023-12181-8.

[31] A. R. Damanpack, A. Sousa, and M. Bodaghi, "Porous plas with controllable density by fdm 3d printing and chemical foaming agent," *Micromachines 2021, Vol. 12, Page 866*, vol. 12, p. 866, 8 Jul. 2021, ISSN: 2072-666X. DOI: 10.3390/MI12080866. [Online]. Available: https://www.mdpi.com/2072-666X/12/8/866/htm%20https://www.mdpi.com/2072-666X/12/8/866.

[32] J. An and K. F. Leong, "Multi-material and multi-dimensional 3d printing for biomedical materials and devices," *Biomedical Materials Devices*, 2022, ISSN: 2731-4812. DOI: 10.1007/s44174-022-00038-9.

[33] C. Zhou and T. Han, "Research on the influencing factors of fdm 3d printing accuracy," vol. 1838, 2021. DOI: 10.1088/1742-6596/1838/1/012027.

[34] F. Kotz, M. Mader, N. Dellen, *et al.*, "Fused deposition modeling of microfluidic chips in polymethylmethacrylate," *Micromachines*, vol. 11, 9 2020, ISSN: 2072666X. DOI: 10.3390/mi11090873.

[35] R. F. Quero, G. D. D. Silveira, J. A. F. D. Silva, and D. P. D. Jesus, "Understanding and improving fdm 3d printing to fabricate high-resolution and optically transparent microfluidic devices," *Lab on a Chip*, vol. 21, 19 2021, ISSN: 14730189. DOI: 10.1039/d1lc00518a.

[36] M. Mader, C. Rein, E. Konrat, *et al.*, "Fused deposition modeling of microfluidic chips in transparent polystyrene," *Micromachines*, vol. 12, 11 2021, ISSN: 2072666X. DOI: 10.3390/mi12111348.

[37] N. P. Macdonald, J. M. Cabot, P. Smejkal, R. M. Guijt, B. Paull, and M. C. Breadmore, "Comparing microfluidic performance of three-dimensional (3d) printing platforms," *Analytical Chemistry*, vol. 89, 7 2017, ISSN: 15206882. DOI: 10.1021/acs.analchem.7b00136.

[38] A. Waldbaur, H. Rapp, K. Länge, and B. E. Rapp, *Let there be chip - towards rapid prototyping of microfluidic devices: One-step manufacturing processes*, 2011. DOI: 10.1039/c1ay05253e.

[39] R. Kumaresan, M. Samykano, K. Kadirgama, D. Ramasamy, N. W. Keng, and A. K. Pandey, “3d printing technology for thermal application: A brief review,” *Journal of Advanced Research in Fluid Mechanics and Thermal Sciences*, vol. 83, pp. 84–97, 2 2021, ISSN: 22897879. DOI: 10.37934/ARFMTS.83.2.8497.

[40] M. Layani, X. Wang, and S. Magdassi, *Novel materials for 3d printing by photopolymerization*, 2018. DOI: 10.1002/adma.201706344.

[41] S. C. Ligon, R. Liska, J. Stampfl, M. Gurr, and R. Mülhaupt, *Polymers for 3d printing and customized additive manufacturing*, 2017. DOI: 10.1021/acs.chemrev.7b00074.

[42] C. W. Hull and C. Arcadia, “Apparatus for production of three-dimensional objects by stereolithography,” Aug. 1984. [Online]. Available: https://patents.google.com/patent/US4575330A/en.

[43] A. A. Bhanvadia, R. T. Farley, Y. Noh, and T. Nishida, “High-resolution stereolithography using a static liquid constrained interface,” *Communications Materials*, vol. 2, 1 2021, ISSN: 26624443. DOI: 10.1038/s43246-021-00145-y.

[44] G. Suresh, “Summarization of 3d-printing technology in processing development of medical implants,” *JOURNAL OF MECHANICS OF CONTINUA AND MATHEMATICAL SCIENCES*, vol. 14, 1 Feb. 2019, ISSN: 09738975. DOI: 10.26782/JMCMS.2019.02.00012.

[45] H. Quan, T. Zhang, H. Xu, S. Luo, J. Nie, and X. Zhu, “Photo-curing 3d printing technique and its challenges,” *Bioactive Materials*, vol. 5, pp. 110–115, 1 Mar. 2020, ISSN: 2452-199X. DOI: 10.1016/J.BIOACTMAT.2019.12.003.

[46] X. Wang, M. Jiang, Z. Zhou, J. Gou, and D. Hui, *3d printing of polymer matrix composites: A review and prospective*, 2017. DOI: 10.1016/j.compositesb.2016.11.034.

[47] *High-resolution 3d printers – the ultimate guide | all3dp pro*. [Online]. Available: https://all3dp.com/1/high-resolution-3d-printer-the-ultimate-guide/.

[48] *4 ways lfs 3d printing produces better parts | formlabs*. [Online]. Available: https://formlabs.com/eu/blog/benefits-of-lfs-3d-printing/.

[49] *Design for sla 3d printing: The ultimate guide*. [Online]. Available: https://www.printpool.co.uk/articles/design-for-sla-3d-printing-the-ultimate-guide.

[50] P. Robles-Martinez, X. Xu, S. J. Trenfield, *et al.*, “3d printing of a multi-layered polypill containing six drugs using a novel stereolithographic method,” *Pharmaceutics*, vol. 11, 6 2019, ISSN: 19994923. DOI: 10.3390/pharmaceutics11060274.

[51] *Adrian bowyer shares his take on multi-material resin 3d printing - 3d printing industry*. [Online]. Available: https://3dprintingindustry.com/news/adrian-bowyer-shares-his-take-on-multi-material-resin-3d-printing-203528/.

[52] *Dlp vs lcd 3d printer: The main differences | all3dp*. [Online]. Available: https://all3dp.com/2/lcd-vs-dlp-3d-printing-technologies-compared/.

[53] N. Divakaran, J. P. Das, A. K. P. V, S. Mohanty, A. Ramadoss, and S. K. Nayak, “Comprehensive review on various additive manufacturing techniques and its implementation in electronic devices,” *Journal of Manufacturing Systems*, vol. 62, pp. 477–502, Jan. 2022, ISSN: 02786125. DOI: 10.1016/J.JMSY.2022.01.002.

[54] C. Sun, N. Fang, D. M. Wu, and X. Zhang, “Projection micro-stereolithography using digital micro-mirror dynamic mask,” *Sensors and Actuators A*, vol. 121, pp. 113–120, 2005. DOI: 10.1016/j.sna.2004.12.011.

[55] R. M. Mainur, “Statistical analysis of the digital micromirror devices hinge sag phenomenon,” *Texas Tech University*, 190211614895 2002. [Online]. Available: https://ttu-ir.tdl.org/items/cc7246e9-17e8-4bfb-8e88-c0db32e2941f.

[56] R. Felzmann, S. Gruber, G. Mitteramskogler, *et al.*, “Lithography-based additive manufacturing of cellular ceramic structures,” vol. 14, 2012. DOI: 10.1002/adem.201200010.

[57] S. Y. Kang, S. Y. Chang, A. Costa, K. Kowsari, and A. W. Ma, “Additive manufacturing of embedded carbon nanocomposite structures with multi-material digital light processing (mmdlp),” *Journal of Materials Research*, vol. 36, pp. 3558–3567, 18 Sep. 2021, ISSN: 20445326. DOI: 10.1557/S43578-021-00224-3. [Online]. Available: https://www.researchgate.net/publication/352083416_Additive_manufacturing_of_embedded_carbon_nanocomposite_structures_with_multi-material_digital_light_processing_MMDLP.

[58] Z. Zhu, “Freeform optics for achieving collimated and uniform light distribution in lcd-type uv-curable 3d printing,” *IEEE Photonics Journal*, vol. 15, 4 Aug. 2023, ISSN: 19430655. DOI: 10.1109/JPHOT.2023.3294478. [Online]. Available: https://www.researchgate.net/publication/372325634_Freeform_Optics_for_Achieving_Collimated_and_Uniform_Light_Distribution_in_LCD-type_UV-Curable_3D_Printing.

[59] *Basic settings and maintenance of a resin 3d printer*. [Online]. Available: https://filament2print.com/gb/blog/148_settings-maintenance-resin-3d-printer.html.

[60] J. Xu, K. Jung, A. Atme, S. Shanmugam, and C. Boyer, “A robust and versatile photoinduced living polymerization of conjugated and unconjugated monomers and its oxygen tolerance,” *Journal of the American Chemical Society*, vol. 136, 14 2014, ISSN: 15205126. DOI: 10.1021/ja501745g.

[61] *Carbon3d unveils breakthrough clip 3d printing technology, 25-100x faster - 3dprint.com | the voice of 3d printing / additive manufacturing*. [Online]. Available: https://3dprint.com/51566/carbon3d-clip-3d-printing/.

[62] Y. Yampolskii, I. Pinnau, and B. D. Freeman, *Materials Science of Membranes for Gas and Vapor Separation*. 2006. DOI: 10.1002/047002903X.

[63] J. R. Tumbleston, D. Shirvanyants, N. Ermoshkin, *et al.*, “Continuous liquid interface production of 3d objects,” *Science*, vol. 347, 6228 2015, ISSN: 10959203. DOI: 10.1126/science.aaa2397.

[64] *All about continuous liquid interface production*. [Online]. Available: https://www.thomasnet.com/articles/custom-manufacturing-fabricating/continuous-liquid-interface-production-3d-printing/.

[65] B. J. Lee, K. Hsiao, G. Lipkowitz, T. Samuelsen, L. Tate, and J. M. DeSimone, “Characterization of a 30 µm pixel size clip-based 3d printer and its enhancement through dynamic printing optimization,” *Additive Manufacturing*, vol. 55, p. 102 800, Jul. 2022, ISSN: 2214-8604. DOI: 10.1016/J.ADDMA.2022.102800.

[66] *Mjp (multi-jet printing) | whiteclouds - whiteclouds*. [Online]. Available: https://www.whiteclouds.com/3dpedia/mjp/.

[67] *What is multijet printing (mjp)?* [Online]. Available: https://markforged.com/resources/learn/3d-printing-basics/3d-printing-processes/what-is-multijet-printing-mjp.

[68] *Polyjet high resolution 3d printing technology | full colour, multi-material*. [Online]. Available: https://proto3000.com/service/3d-printing-services/technologies/polyjet/.

[69] S. J. Keating, M. I. Gariboldi, W. G. Patrick, S. Sharma, D. S. Kong, and N. Oxman, “3d printed multi-material microfluidic valve,” *PLoS ONE*, vol. 11, 8 2016, ISSN: 19326203. DOI: 10.1371/journal.pone.0160624.

[70] F. Burmeister, S. Steenhusen, R. Houbertz, *et al.*, “Two-photon polymerization of inorganic-organic polymers for biomedical and microoptical applications,” *Optically Induced Nanostructures: Biomedical and Technical Applications*, pp. 239–265, May 2015. DOI: 10.1515/9783110354324-016/HTML. [Online]. Available: https://www.cesma.de/en/processing/two-photon-polymerization.html.

[71] S. Maruo and J. T. Fourkas, *Recent progress in multiphoton microfabrication*, 2008. DOI: 10.1002/lpor.200710039.

[72] J. Stampfl, R. Liska, A. Ovsianikov, J. Stampfl, R. Liska, and A. Ovsianikov, *Multiphoton Lithography: Techniques, Materials, and Applications*. 2016.

[73] A. Z. Zabidi, S. Li, R. M. Felfel, *et al.*, “Computational mechanical characterization of geometrically transformed schwarz p lattice tissue scaffolds fabricated via two photon polymerization (2pp),” *Additive Manufacturing*, vol. 25, pp. 399–411, Jan. 2019, ISSN: 22148604. DOI: 10.1016/J.ADDMA.2018.11.021.

[74] Z. F. Rad, P. D. Prewett, and G. J. Davies, *High-resolution two-photon polymerization: The most versatile technique for the fabrication of microneedle arrays*, 2021. DOI: 10.1038/s41378-021-00298-3.

[75] S. Maruo and K. Ikuta, “Submicron stereolithography for the production of freely movable mechanisms by using single-photon polymerization,” *Sensors and Actuators A: Physical*, vol. 100, pp. 70–76, 1 Aug. 2002, ISSN: 0924-4247. DOI: 10.1016/S0924-4247(02)00043-2.

[76] *Nanoscribe photonic professional gt2 review - professional resin 3d printer*. [Online]. Available: https://www.aniwaa.com/product/3d-printers/nanoscribe-photonic-professional-gt2/.

[77] M. Emons, K. Obata, T. Binhammer, *et al.*, “Two-photon polymerization technique with sub-50 nm resolution by sub-10 fs laser pulses references and links,” 2012. [Online]. Available: https://www.researchgate.net/publication/249339564_Two-photon_polymerization_technique_with_sub-50_nm_resolution_by_sub-10_fs_laser_pulses.

[78] Q. Hu, G. A. Rance, G. F. Trindade, *et al.*, “The influence of printing parameters on multi-material two-photon polymerisation based micro additive manufacturing,” *Additive Manufacturing*, vol. 51, p. 102 575, Mar. 2022, ISSN: 2214-8604. DOI: 10.1016/J.ADDMA.2021.102575.

[79] B. Khatri, M. Frey, A. Raouf-Fahmy, M. V. Scharla, and T. Hanemann, “Development of a multi-material stereolithography 3d printing device,” *Micromachines*, vol. 11, 5 2020, ISSN: 2072666X. DOI: 10.3390/mi11050532.

[80] R. Singh, R. Kumar, I. Farina, F. Colangelo, L. Feo, and F. Fraternali, “Multi-material additive manufacturing of sustainable innovative materials and structures,” *Polymers*, vol. 11, 1 2019, ISSN: 20734360. DOI: 10.3390/polym11010062.

[81] D. J. O’Sullivan, “Stabilized adhesive and curing compositions,” Jul. 1976. [Online]. Available: https://patents.google.com/patent/US4100141A/en.

[82] C. W. Hull and C. W. Lewis, “Methods and apparatus for production of three-dimensional objects by stereolithography,” Apr. 1988. [Online]. Available: https://patents.google.com/patent/US4999143A/en.

[83] S. K. Mirle, E. City, R. J. Kumpfmiller, and G. W. R, “Photosensitive compositions useful in three-dimensional part-building and having improved photospeed,” Nov. 1993. [Online]. Available: https://patents.google.com/patent/US5418112A/en.

[84] X. Zhang, X. N. Jiang, and C. Sun, “Micro-stereolithography of polymeric and ceramic microstructures,” *Sensors and Actuators, A: Physical*, vol. 77, 2 1999, ISSN: 09244247. DOI: 10.1016/S0924-4247(99)00189-2.

[85] W. A. Green, *Industrial photoinitiators: A technical guide*. [Online]. Available: https://books.google.nl/books?hl=en&lr=&id=b1jRBQAAQBAJ&oi=fnd&pg=PP1&ots=PERJj-lcQv&sig=hNwvgsbE-iKmwmCoy5A8lsmmZn4&redir_esc=y#v=onepage&q&f=false.

[86] A. Bagheri and J. Jin, “Photopolymerization in 3d printing,” *ACS Applied Polymer Materials*, vol. 1, pp. 593–611, 4 Apr. 2019, ISSN: 26376105. DOI: 10.1021/ACSAPM.8B00165. [Online]. Available: https://pubs.acs.org/sharingguidelines.

[87] C. W. Hull, S. Clarita, S. T. Spence, *et al.*, “Stereolithographic curl reduction,” Jun. 1998. [Online]. Available: https://patents.google.com/patent/US6048188A/en.

[88] R. R. Moraes, J. W. Garcia, M. D. Barros, *et al.*, “Control of polymerization shrinkage and stress in nanogel-modified monomer and composite materials,” *Dental Materials*, vol. 27, pp. 509–519, 6 Jun. 2011, ISSN: 0109-5641. DOI: 10.1016/J.DENTAL.2011.01.006.

[89] D. G. Leppard, M. Kohler, and L. Misev, “Photopolymerizable compositions containing an alkylbisacylphosphine oxide,” Apr. 1994. [Online]. Available: https://patents.justia.com/patent/5472992.

[90] S. C. Ligon-Auer, M. Schwentenwein, C. Gorsche, J. Stampfl, and R. Liska, “Toughening of photo-curable polymer networks: A review,” *Polymer Chemistry*, vol. 7, pp. 257–286, 2 Jan. 2016, ISSN: 17599962. DOI: 10.1039/C5PY01631B.

[91] S. C. Lapin, J. R. Snyder, E. V. Sitzmann, D. Plaines, D. K. Barnes, and G. D. Green, “Stereolithography using vinyl ether-epoxide polymers,” Feb. 1994. [Online]. Available: https://patents.google.com/patent/US5437964A/en.

[92] W. ; Akira and T. ; Takashi, “Photo-curable resin composition used for photo fabication of three-dimensional objects,” Dec. 1997. [Online]. Available: https://patents.google.com/patent/US5981616A/en.

[93] K. A. D. K. K. Ohkawa and S. A. D. K. K. Saito, “Resin composition for optical modeling,” Feb. 1989. [Online]. Available: https://patents.google.com/patent/EP0360869A4/en.

[94] P. Mosadegh, C. Polygerinos, S. Keplinger, *et al.*, “Pneumatic networks for soft robotics that actuate rapidly,” *Advanced Functional Materials*, vol. 24, pp. 2163–2170, 15 2014. DOI: 10.1002/adfm.201303288.

[95] D. K. Patel, A. H. Sakhaei, M. Layani, B. Zhang, Q. Ge, and S. Magdassi, “Highly stretchable and uv curable elastomers for digital light processing based 3d printing,” *Advanced Materials*, vol. 29, 15 2017, ISSN: 15214095. DOI: 10.1002/adma.201606000.

[96] M. Liu, J. Sun, Y. Sun, C. Bock, and Q. Chen, “Thickness-dependent mechanical properties of polydimethylsiloxane membranes,” *Journal of Micromechanics and Microengineering*, vol. 19, 3 2009, ISSN: 09601317. DOI: 10.1088/0960-1317/19/3/035028. [Online]. Available: https://www.researchgate.net/publication/231042781_Thickness-dependent_mechanical_properties_of_polydimethylsiloxane_membranes.

[97] F. C. Sales, R. M. Ariati, V. T. Noronha, and J. E. Ribeiro, “Mechanical characterization of pdms with different mixing ratios,” *Procedia Structural Integrity*, vol. 37, pp. 383–388, C Jan. 2022, ISSN: 2452-3216. DOI: 10.1016/J.PROSTR.2022.01.099.

[98] *Is there a silicone 3d-printing photopolymer resin?* | *liqcreate*. [Online]. Available: https://www.liqcreate.com/supportarticles/silicone-photopolymer-resin-3dprinting/.

[99] U. Gleißner and T. Hanemann, “Tailoring the optical and rheological properties of an epoxy acrylate based host-guest system,” *Optical Engineering*, vol. 53, 8 2014, ISSN: 0091-3286. DOI: 10.1117/1.oe.53.8.087106.

[100] U. Gleißner, T. Hanemann, C. Megnin, and F. Wieland, “The influence of photo initiators on refractive index and glass transition temperature of optically and rheologically adjusted acrylate based polymers,” *Polymers for Advanced Technologies*, vol. 27, 10 2016, ISSN: 10991581. DOI: 10.1002/pat.3793.

[101] T. Nakahara, J. Suzuki, Y. Hosokawa, F. Shimokawa, H. Kotera, and T. Suzuki, “Fabrication of magnetically driven microvalve arrays using a photosensitive composite,” *Magnetochemistry*, vol. 4, 1 2018, ISSN: 23127481. DOI: 10.3390/magnetochemistry4010007.

[102] N. Lazarus, S. S. Bedair, and G. L. Smith, “Creating 3d printed magnetic devices with ferrofluids and liquid metals,” *Additive Manufacturing*, vol. 26, 2019, ISSN: 22148604. DOI: 10.1016/j.addma.2018.12.012.

[103] T. J. Wallin, J. Pikul, and R. F. Shepherd, *3d printing of soft robotic systems*, 2018. DOI: 10.1038/s41578-018-0002-2.

[104] G. Weisgrab, A. Ovsianikov, and P. F. Costa, “Functional 3d printing for microfluidic chips,” *Advanced Materials Technologies*, vol. 4, no. 10, 2019. DOI: 10.1002/admt.201900275.

[105] C. S. Loh, H. Yukoi, and T. Arai, “New shape memory alloy actuator: Design and application in the prosthetic hand,” vol. 7 VOLS, 2005. DOI: 10.1109/iembs.2005.1616092.

[106] A. Inamdar, M. Magana, F. Medina, Y. Grajeda, and R. Wicker, “Development of an automated multiple material stereolithography machine,” 2006. [Online]. Available: https://www.researchgate.net/publication/235666915_Development_of_an_automated_multiple_material_stereolithography_machine.

[107] J. W. Choi, H. C. Kim, and R. Wicker, “Multi-material stereolithography,” *Journal of Materials Processing Technology*, vol. 211, pp. 318–328, 3 Mar. 2011, ISSN: 09240136. DOI: 10.1016/J.JMATPROTEC.2010.10.003. [Online]. Available: https://www.researchgate.net/publication/229346617_Multi-material_stereolithography.

[108] Y. T. Kim, A. Ahmadianyazdi, and A. Folch, “A ‘print–pause–print’ protocol for 3d printing microfluidics using multimaterial stereolithography,” *Nature Protocols*, vol. 18, 4 2023, ISSN: 17502799. DOI: 10.1038/s41596-022-00792-6.

[109] J. W. Choi, E. MacDonald, and R. Wicker, “Multi-material microstereolithography,” *International Journal of Advanced Manufacturing Technology*, vol. 49, 5-8 2010, ISSN: 02683768. DOI: 10.1007/s00170-009-2434-8.

[110] R. B. Wicker and E. W. MacDonald, “Multi-material, multi-technology stereolithography,” *Virtual and Physical Prototyping*, vol. 7, 3 2012, ISSN: 1745-2759. DOI: 10.1080/17452759.2012.721119.

[111] C. Zhou, Y. Chen, Z. Yang, and B. Khoshnevis, “Development of a multi-material mask-image-projection-based stereolithography for the fabrication of digital materials,” 2011. [Online]. Available: https://utw10945.utweb.utexas.edu/Manuscripts/2011/2011-06-Zhou.pdf.

[112] Y. T. Kim, K. Castro, N. Bhattacharjee, and A. Folch, “Digital manufacturing of selective porous barriers in microchannels using multi-material stereolithography,” *Micromachines*, vol. 9, 3 2018, ISSN: 2072666X. DOI: 10.3390/mi9030125.

[113] M. Vaezi, S. Chianrabutra, B. Mellor, and S. Yang, *Multiple material additive manufacturing - part 1: A review: This review paper covers a decade of research on multiple material additive manufacturing technologies which can produce complex geometry parts with different materials*, 2013. DOI: 10.1080/17452759.2013.778175.

[114] D. Han, C. Yang, N. X. Fang, and H. Lee, "Rapid multi-material 3d printing with projection micro-stereolithography using dynamic fluidic control," *Additive Manufacturing*, vol. 27, 2019, ISSN: 22148604. DOI: 10.1016/j.addma.2019.03.031.

[115] A. K. Miri, D. Nieto, L. Iglesias, *et al.*, "Microfluidics-enabled multimaterial maskless stereolithographic bioprinting," *Advanced Materials*, vol. 30, 27 2018, ISSN: 15214095. DOI: 10.1002/adma.201800242.

[116] K. Kowsari, S. Akbari, D. Wang, N. X. Fang, and Q. Ge, "High-efficiency high-resolution multimaterial fabrication for digital light processing-based three-dimensional printing," *3D Printing and Additive Manufacturing*, vol. 5, 3 2018, ISSN: 23297670. DOI: 10.1089/3dp.2018.0004.

[117] *Bcn3d: Viscous lithography manufacturing (vlm) 3d printing technology*. [Online]. Available: https://vlm.bcn3d.com/.

[118] *What is viscous lithography manufacturing or vlm 3d printing technology? | by manufactur3d | medium*. [Online]. Available: https://medium.com/@Manufactur3DMagazine/what-is-viscous-lithography-manufacturing-or-vlm-3d-printing-technology-7ab40a077db3.

[119] H. Wang, A. Enders, J. A. Preuss, J. Bahnemann, A. Heisterkamp, and M. L. Torres-Mapa, "3d printed microfluidic lab-on-a-chip device for fiber-based dual beam optical manipulation," *Scientific Reports*, vol. 11, 1 Dec. 2021, ISSN: 20452322. DOI: 10.1038/S41598-021-93205-9. [Online]. Available: https://www.researchgate.net/publication/353293564_3D_printed_microfluidic_lab-on-a-chip_device_for_fiber-based_dual_beam_optical_manipulation.

[120] *What does resolution mean in 3d printing? | formlabs*. [Online]. Available: https://formlabs.com/eu/blog/3d-printer-resolution-meaning/.

[121] *Bio-mems - wikipedia*. [Online]. Available: https://en.m.wikipedia.org/wiki/Bio-MEMS.

[122] *Photonsters validation matrix v2*. [Online]. Available: https://www.printables.com/model/229429-photonsters-validation-matrix-v2.

[123] *3djake resin colorant verkeersrood - 3djake nederland*. [Online]. Available: https://www.3djake.nl/3djake/resin-colorant-verkeersrood?sai=10882.

[124] *Coloring of elastomer-x, elastic 3d-printing resin | liqcreate*. [Online]. Available: https://www.liqcreate.com/supportarticles/coloring-3dprinting-resin-elastic-rubber/.

[125] *Explained: How to adjust coloring of your 3d print resin*. [Online]. Available: https://www.liqcreate.com/supportarticles/explained-tested-coloring-of-3d-printing-resin/.

[126] F. Aloui, L. Lecamp, P. Lebaudy, and F. Burel, "Refractive index evolution of various commercial acrylic resins during photopolymerization," *Express Polymer Letters*, vol. 12, pp. 966–971, 11 Nov. 2018, ISSN: 1788618X. DOI: 10.3144/EXPRESSPOLYMLETT.2018.83. [Online]. Available: https://www.researchgate.net/publication/327243682_Refractive_index_evolution_of_various_commercial_acrylic_resins_during_photopolymerization.

[127] *Modeling elastomers using fem: Do's and dont's | simscale blog*. [Online]. Available: https://www.simscale.com/blog/tips-modeling-elastomers-using-fem/.